Extensions of dynamical mean-field theory to non-local correlations and multi-band systems

Von der Fakultät Mathematik und Physik der Universität Stuttgart
zur Erlangung der Würde eines Doktors der Naturwissenschaften
(Dr. rer. nat.) genehmigte Abhandlung

Vorgelegt von

Xiaodong Cao

aus Jiangyou, China

Hauptberichter:	Dr. Philipp Hansmann
Mitberichter:	Prof. Dr. Maria Daghofer
	Prof. Dr. Hidenori Takagi
Tag der mündlichen Prüfung:	30. October 2019

Max-Planck-Institut für Festkörperforschung
Universität Stuttgart
Stuttgart 2019

Zusammenfassung

Stark korrelierte Materialien stellen eine einzigartige Klasse von Verbindungen dar, in denen interessante physikalische Phänomene gefunden werden können. Einige Beispiele sind: kolossaler Magnetowiderstand, Metall-Isolator-Übergang und Hochtemperatursupraleitung. Diese neuartigen Phänomene versprechen einerseits neue Technologien —oder haben diese bereits ermöglicht—, die die menschliche Gesellschaft erheblich verbessern könnten, und bieten andererseits eine hervorragende Plattform, um innovative Physik zu entdecken. Daher ist das Verstehen solcher Systeme oder insbesondere der Versuch, universelle Konzepte und Methoden zu entwickeln, die eine Verbindung zwischen der mikroskopischen Elektronenstruktur und den makroskopischen Eigenschaften herstellen können, eines der großen Ziele der Physik der kondensierten Materie und definiert auch den Bereich, zu dem diese Doktorarbeit beitragen soll.

Eine der charakteristischen Eigenschaften korrelierter Elektronensysteme ist, dass ihre Observablen gleichzeitig Merkmale der vollständig lokalisierten Grenze—wie atomare Multiplets—und der itineranten (renormierten) Fermi-Flüssigkeitsgrenze auf weisen können, was ihre theoretische Behandlung schwierig und störungstheoretische Ansätze inadäquat macht. Genau aus dem diesem Grund besitzen diese Systemen jedoch reichhaltige Phasendiagramme, die ihre Empfindlichkeit gegenüber externen Einflüssen zeigt. Daher ist die Entwicklung einer störungstheorie-freien Behandlung der Niedrigenergiemodelle—wie das Hubbard-Modell und seine Multiband-Varianten—, die für diese Kategorie von Systemen abgeleitet wurden, äußerst wünschenswert.

Die dynamische Molekularfeldtheorie (DMFT) ist eine der erfolgreichsten Methoden, die in den letzten Jahrzehnten entwickelt wurde, um diese subtilen Merkmale stark korrelierter Systeme zu beschreiben. Sie legt einen Schwerpunkt auf die Lokalität dieser Systeme und behandelt die lokalen Korrelationen störungstheoriefrei, durch Abbildung des ursprünglichen Systems auf ein effektives Störstellen-Modell, welches mit numerischen Methoden mit hoher Genauigkeit gelöst wird. Es wurde erfolgreich angewendet, um die Natur des Metall-Isolator-Übergangs und die Auswirkungen der Hund'schen Kopplung in Multi-Orbital-Systemen aufzudecken. Kürzlich wurden auch Erkenntnisse über das Zusammenspiel von Coulomb-Wechselwirkung und Spin-Bahn-Kopplung in Seltenerdmetalloxiden gewonnen. Trotz des Erfolges gibt es jedoch Mängel und Hindernisse bei der Anwendung von DMFT: Die lokalen Korrelationen werden zwar störungsfrei behandelt, die nicht lokalen Korrelationen, die für die zugrunde liegende neuartige Physik von großer Bedeutung sein

könnten, werden jedoch komplett vernachlässigt; Außerdem kann die Lösung des—zwar vereinfachten—Störstellen-Modells immer noch sehr schwierig sein, insbesondere wenn es mehrere stark verschränkte Freiheitsgrade enthält. Diese Arbeit stellt unsere Lösungsansätze, diese Mängel und Hindernisse von DMFT zu beseitigen, vor.

Wir beginnen mit der Darstellung des Hintergrunds der Standard-DMFT, die die klassische Molekularfeldtheorie um lokale, thermische und Quantenfluktuationen erweitert, gefolgt von der Motivation, sowohl nicht-lokale Korrelationen als auch Wechselwirkungen einzubeziehen. Durch Einführung von Bosonischen Feldern zur Entkopplung der Elektron-Elektron-Wechselwirkung wird eine einheitliche Herleitung der Selbstkonsistenzgleichungen für DMFT, Extended DMFT (EDMFT) und TRiply Irreducible Local EXpansion (TRILEX) dargestellt. Innerhalb dieses einheitlichen Rahmens werden die Approximationsebenen verschiedener Methoden (DMFT, EDMFT, TRILEX) offensichtlich. Als ein Beispiel für die Wichtigkeit und Notwendigkeit der Einbeziehung nicht-lokaler Korrelationen werden die Adatom-Oberflächensysteme, deren Niedrigenergiephysik durch ein erweitertes Einband-Hubbard-Modell mit einer $1/r$ - Lang- streckenwechselwirkung auf dem Dreieck-Gitter beschrieben wird, mit der TRILEX-Methode untersucht. Das Zusammenspiel von Spin- und Ladungsfluktuationen und deren Auswirkungen auf die Entstehung unkonventioneller Supraleitung in diesen experimentell gut kontrollierten Systemen werden durch die Analyse der Impulsaufgelö- sten Antwortfunktionen aufgedeckt. Interessanterweise spielt die intrinsische nicht-lokale Wechselwirkung in dieser Materialkategorie eine wesentliche Rolle für die Entstehung einer unkonventionellen supraleitenden Paarung, was sich in der direkten Abhängigkeit der supraleitenden Übergangstemperatur von der nicht-lokalen Wechselwirkungsstärke im widerspiegelt. Ein weiterer wichtiger Bestandteil der beobachteten supraleitenden Phase ist die Dreiecksgittersymmetrie dieser Materialien, die einen kumulativen Beitrag von Spin- und Ladungsfluktuationen zur supraleitenden Instabilität ermöglicht. Diese Ergebnisse lassen auf ein supraleitendes Paarungsszenario schließen, das sich vom häufig untersuchten Hubbard-Modell auf dem Quadratgitter unterscheidet und möglicherweise auch die experimentelle Forschung im loch-dotierten Bereich dieser Materialien anregt.

Der zweite Teil dieser Arbeit trägt zur Entwicklung tensorproduktzustandsbasierter Lösungsmethoden für das Anderson Impurity Modell auf der reellen Achse für allgemeine DMFT-Rechnungen bei. Wir beginnen mit der Motivation von Matrix-Produktzuständen (MPS) basierenden Ansätze, indem wir die Stärken und Mängel der vorhandenen Methoden untersuchen. Anschließend geben wir eine umfassende Einführung in die MPS-Theorie und die zugehörigen Algorithmen, die zur Implementierung des Störstellen-Lösers erforderlich sind. Im nächsten Schritt führen wir die Rotation in die natürliche Orbitalbasis für allgemeine Störstellen-Modelle ein und stellen ihren Vorteil gegenüber der allgemein verwendeten Ketten- und Sternbasen durch Analyse der Verschränkung des Störstellen-Grundzustands fest. Durch Rota-

tion auf die natürliche Orbitalbasis erzielen wir nicht nur eine viel kleinere maximale Bindungsdimension der MPS, sondern auch einen schnelleren Abbau der Bindungsdimension im ganzen System. Darüber konvergiert die Dichte als Funktion des Abstands von der Störstelle in der Bad-Stelle im Leitungsband (Valenzband) exponentiell zum leeren (vollen) Zustand. Basierend auf dieser Dichteverteilung schlagen wir eine Teilchenzahl-Projektionsmethode vor, die die Anzahl der erlaubten Elektronen (Löcher) im Leitungsband (Valenzband) begrenzt. Dies ermöglicht eine systematische Kontrolle des Gleichgewichts zwischen Genauigkeit und Rechenaufwand durch Anpassung der Projektionsparameter. Die Leistungsfähigkeit der vorgeschlagenen Methode wird durch Lösen des Einband-Hubbard-Modells auf dem Bethe-Gitter in verschiedenen Parameterregionen demonstriert. Um den Schwierigkeiten im Frequenzbereich entgegenzuwirken, erweitern wir diese Projektionsmethode auf den Zeitbereich. Indem wir den exponentiellen Abfall der Gewichte von Zuständen, hinsichtlich der erlaubten Teilchenzahl, im Leitungsband und Valenzband zeigen, können wir den Schluss ziehen, dass diese Projektionsmethode hocheffizient ist und exponentiell mit der Entwicklungsordnung, der Anzahl der zulässigen Teilchen in der projizierten Region, und Subsystemgröße konvergiert. Benchmarks und Tests dieser Zeitbereichs-Projektionsmethode werden auch für das Einband-Hubbard-Modell auf dem Bethe-Gitter durchgeführt, und es wird eine gute Übereinstimmung mit den vorhandenen Ergebnissen aus der Literatur beobachtet.

Trotz der Tatsache, dass die Rotation zur natürlichen Orbital Darstellung die Einteilchenbasis optimiert und eine kleine Grundzustandsverschränkung für Störstellenmodelle zur Folge hat, ist die Kettengeometrie der MPS nicht für Mehrbandmodelle geeignet. Dies lässt sich anhand des folgenden Beispiels veranschaulichen: Betrachtet man ein Mehrband-Störstellenmodell, das eine ähnliche Bandbreite und Wechselwirkungsstärke aufweist, so kann einerseits die Verschränkung zwischen der Störstelle und der aktiven Stelle, die zum selben Band gehört, aber auch die Verschränkung zwischen den Störstellen, wegen Interband-Wechselwirkungen, ziemlich groß sein. Daher gibt es keine Möglichkeit, die Kettengeometrie so zu ordnen, das die Verschränkung zwischen Störstelle-Aktive Stelle und Störstelle-Störstelle gleichzeitig optimiert. Darüber hinaus ist es unvermeidlich, weit-entfernte Sprünge einzuführen, wenn die Bad-Stellen eines Mehrband-Störstellenmodells auf einer Kettengeometrie angeordnet werden. Daher sind alternative Tensorproduktzustände wünschenswert, die in der Lage sind, die Verschränkungsstruktur eines allgemeinen Mehrband-Störstellenmodells auf optimierte Weise zu erfassen. Fork-Tensor-Produkt-Zustände (FTPS) stellen einen dieser Versuche dar. Sie trennen die Freiheitsgrade, die zu verschiedenen Bändern gehören, indem sie auf verschiedene Gabelungen—der Fork (Gabel)—gelegt werden. Indem wir weiter festhalten, dass die FTPS zu den allgemeineren Tree-Tensor-Produkt-Zuständen (TTPS) gehören, schlagen wir in dieser Arbeit eine TTPS-Darstellung der Vielkörperwellenfunktion eines allgemeinen, in die Basis der

natürlichen Orbital rotierten, Mehrband-Störstellenmodells vor. Der Vorteil dieser vorgeschlagenen TTPS ist, dass sie nicht nur die Freiheitsgrade, die zu verschiedenen Bändern gehören, sondern auch das Leitungs- und das Valenzband, die ausdrücklich zu demselben Band gehören, voneinander trennen. Zusammen mit allen Vorteilen der Rotation in die natürliche Orbitalbasis kann dieser Störstellen-Löser Probleme bewältigen, die mit anderen Methoden nicht möglich sind. Für Benchmark- und Demonstrationszwecke wird die prototypische Verbindung $SrVO_3$ mit dem vorgeschlagenen Störstellen-Löser im Rahmen von DMFT gelöst. Die erhaltene Green'sche Funktion zeigt eine schnelle Konvergenz mit der Bindungsdimension der TTPS, löst die atomaren Multiplets korrekt auf und zeigt auch eine gute Übereinstimmung mit den FTPS Referenzergebnissen.

Zusammenfassend haben wir die Wichtigkeit und Notwendigkeit der Einbeziehung nicht-lokaler Korrelationen in die Standard-DMFT Methode durch die TRILEX-Studie der loch-dotierten Adadom-Oberflächensysteme gezeigt. Darüber hinaus werden die wesentlichen Rollen der Ferninteraktion und Gittersymmetrie bei der Entstehung der supraleitenden Paarung durch die Analyse der Impuls-aufgelösten Antwortfunktionen aufgezeigt. Um nicht-lokale Korrelationen in die Cluster-Erweiterungen von DMFT einzubeziehen und auch Mehrbandsysteme zu handhaben, entwickeln wir einen effizienten Störstellen-Löser, der den Kern der DMFT-Berechnungen bildet. Durch die Rotation in die natürliche Orbitalbasis wird ein Projektionsmethode sowohl für den Frequenz- als auch für den Zeitbereich vorgeschlagen und getestet. Um den inhärenten Schwierigkeiten der MPS-Darstellung der Vielkörperwellenfunktion eines Mehrbandsystems entgegenzuwirken, haben wir einen baumtensorproduktzustand vorgeschlagen, um die Verschränkungsstrukturen von Mehrbandmodellen korrekt zu erfassen. Dieser Störstellen-Löser wurde durch Simulationen des prototypischen $SrVO_3$ getestet und zeigt ein großes Potenzial für weitere Anwendungen.

Contents

1

Introduction and Motivation

Strongly correlated materials present a unique class of compounds in which interesting phenomena can be found. Some of the examples are colossal magnetoresistance, metal-insulator transition and high-temperature superconductivity. These novel phenomena, on one hand, promise and have already triggered new techniques that could greatly improve human society, and on the other hand, provide a great platform to reveal novel physics. Hence, the understanding of such systems, or specifically, attempt of developing universal concepts and methods that can build a connection between the microscopic electron structure to the macroscopic properties, is one of the golden goals of condensed matter physics, and also defines the realm to where this thesis intends to contribute.

One of the characteristic features of correlated electron systems is that their observables may show-at the same time-features from the fully localized limit (like atomic multiplets) and itinerant or renormalized Fermi-liquid limit, which makes their theoretical treatment challenging and perturbative approaches inadequate. However, it is precisely for the same reason that these systems display rich phase diagrams highlighting their sensitivity to external perturbation. Hence, the development of non-perturbative treatment of low energy models derived for this category of systems (like the Hubbard model and its multi-band variants) is highly desirable.

Dynamical mean-field theory (DMFT) is one of the most successful methods which are developed during the past decades aimed to capture these subtle features of

strongly correlated systems. It puts an emphasis on the locality of these systems and treats the local correlation non-perturbatively through mapping of the original system to an effective impurity model which is then solved with numerical methods to high accuracy. It has been successfully applied to reveal the nature of metal-insulator transition, the effects of Hund's coupling in multi-orbital systems, and recently it also provides insights into the interplay between Coulomb interaction and spin-orbital coupling in rare earth metal oxides. However, despite its success, there are shortcomings and obstacles in the application of DMFT: first, although the local correlations are treated in a non-perturbative way, the non-local correlations, which could be quite important in the underlying novel physics, are totally ignored; second, compared to solving the original lattice problem, although it has already been simplified, solving the impurity model, especially when it contains several highly entangled degrees of freedom, can be still very difficult.

This thesis presents our attempts to improve upon these shortcomings and obstacles of DMFT. In the first part, we present the theoretical background of TRiply Irreducible Local EXpansion (TRILEX) extension to DMFT and its application to adatom systems as:

- chapter 2 first presents the basic background of the standard DMFT followed by the motivation to include both non-local correlations and interactions. Then, by introducing bosonic fields to decouple the electron-electron interaction, a unified derivation of the self-consistency equations for DMFT, extended DMFT (EDMFT) and TRILEX is presented. Within such a unified framework, the levels of approximation of different methods (DMFT, EDMFT, TRILEX) are discussed.

- in chapter 3, the TRILEX method is applied to the adatom surface systems. Starting from a motivation to study the interplay between spin- and charge-fluctuations and their effects on the emergence of unconventional superconductivity in well controlled systems, we perform a comprehensive study of the hole doped phase diagram of the adatom systems. In particular, the impact of long-range interaction and lattice symmetry on the superconductivity instability are studied in detail as a novel ingredient to unconventional superconductivity.
  Parts of the contents of this chapter have been published in

"Chiral $d-$wave superconductivity in a triangular surface lattice mediated by long-range interaction", **Xiaodong Cao**, Thomas Ayral, Zhicheng Zhong, Olivier Parcollet, Dirk Manske, and Philipp Hansmann, ***Phys. Rev. B 97, 155145, 20 April 2018***

The second part of this thesis contributes to the development of tensor product states based impurity solvers on the real-axis for general DMFT calculations as:

- in chapter 4, we start with the motivation of the matrix product states (MPS) based impurity solver for general DMFT calculations by reviewing the strengths and shortcomings of the existing methods, then we give a comprehensive introduction of the MPS and the related algorithms which are needed to implement the impurity solver.

- in chapter 5 and chapter 6, we introduce the rotation to natural-orbital basis for general impurity models and establish its advantage to chain and star basis by analyzing entanglement of the impurity ground state. Furthermore, based on the density distribution in the natural-orbital basis, we propose a particle-number projection method which constrains the allowed electrons (holes) in the conduction (valence) channel. This allows for a systematical control of balance between the accuracy and computational cost by tuning the projection parameters. Performances of the proposed method in both frequency- and time-domain are demonstrated by solving the single-band Hubbard model on the Bethe lattice in various parameter regions.
  Parts of the contents of this chapter have been presented in

  "Natural-Orbital Impurity Solver and Projection Approach for Green's Function", Yi Lu, **Xiaodong Cao**, Philipp Hansmann and Maurits W. Haverkort, ***Phys.Rev.B 100, 115134, 16 September 2019***.

- in chapter 7, by analyzing the entanglement structure of multi-band impurity models, we introduce the tree tensor product states (TTPS) as an extension of the MPS for the single-band impurity models in the natural-orbital basis. After elaborating on extending algorithms developed for the MPS to TTPS, we demonstrate its performance by solving the prototypical compound $SrVO_3$.
  Parts of the contents of this chapter are presented in

"Efficient real-aixs tree tensor product states impurity solver in the natural-orbital basis", **Xiaodong Cao**, Yi Lu, Philipp Hansmann and Maurits W. Haverkort, ***in preparation***.

In chapter 8, we present a conclusion of this thesis and an outlook for future research.

2

Dynamical mean-filed theory and its TRILEX extension

The Hamiltonian for a general solid, which consists of oppositely charged nuclei and electrons, in crystalline structure can be formulated as

$$H = H_e + H_i, \tag{2.1}$$

$$H_e = \sum_i \left[-\frac{\hbar^2}{2m} \nabla^2_{\mathbf{r}_i} + V(\mathbf{r}_i) \right] + \frac{1}{2} \sum_{i \neq j} V_{ee} \left(\mathbf{r}_i - \mathbf{r}_j \right), \tag{2.2}$$

$$H_i = \sum_i -\frac{\hbar^2}{2M} \nabla^2_{\mathbf{R}_i} + \frac{1}{2} \sum_{i \neq j} V_{ii} \left(\mathbf{R}_i - \mathbf{R}_j \right). \tag{2.3}$$

Here, m (M) represents the mass of an electron (ion), and $\mathbf{r}_i$ ($\mathbf{R}_i$) its coordinates. V_{ee} (V_{ii}) is the Coulomb interaction between electrons (ions), while $V(\mathbf{r}_i) = \sum_j V_{ei}(\mathbf{r}_i - \mathbf{R}_j)$ is the ionic potential experienced by each electron. Since the ion is usually much heavier than the electron, it is reasonable to consider the ions to be static and focus only on the electronic degrees of freedom. After choosing a specific Wannier basis for the lattice problem, such an electronic Hamiltonian can be also written in the

second-quantized form as

$$H_0 = \sum_{ij,\alpha\beta} t_{ij}^{\alpha\beta} c_{i\alpha}^{\dagger} c_{j\beta}, \tag{2.4}$$

$$H_{\mathbf{int}} = \frac{1}{2} \sum_{ijkl} \sum_{\alpha\beta\gamma\delta} U_{ijkl}^{\alpha\beta\gamma\delta} c_{i\alpha}^{\dagger} c_{j\beta}^{\dagger} c_{k\gamma} c_{l\delta}, \tag{2.5}$$

where the latin indices represent the spatial coordinates, and the greek indices represents the collection of orbital and spin degrees of freedom. The hopping ($t_{ij}^{\alpha\beta}$) and interaction ($U_{ijkl}^{\alpha\beta\gamma\delta}$) can be obtained from the integral between the localized Wannier wave functions on each lattice site.

In general, a full solution of the Eq. (2.4) is impractical. The difficulty is that, when the interaction term $H_{\mathbf{int}}$ is not negligible or comparable with the kinetic part H_0, the total Hilbert space grows exponentially with the number of degrees of freedom. This is the famous "exponential wall problem" of strongly correlated systems.

To circumvent this difficulty, various methods have been developed over the past decades. Among these, mean-filed theory is probably the simplest method one might come up with. The basic idea behind this method is to map the original untraceable lattice model to an effective single-site model. Typically, such mapping causes fluctuations to be frozen out and thus only a static mean-field is left out to represent the relevant energy scale of the original system. It can be useful to provide a qualitative understanding about the underlying physics. However, once the fluctuations become strong or several energy scales are closely coupled and compete with each other, we need to employ more sophisticated methods.

Similar to the traditional mean-filed theory, DMFT also maps the complicated lattice model into an effective impurity model. The pioneering work to this mapping was made by Metzner and Vollhardt [1], who pointed out that the lattice fermionic strongly correlated systems have a nontrivial limit in the large dimension limit: the self-energy and Green's function are purely local! Then, with such an insight, a further interpretation of functional equations in the large dimension limit as an interacting impurity coupled with a self-consistent determined non-interacting bath was made in Refs. [2, 3, 4]. The difference to the classical mean-theory is that in DMFT, although the spatial fluctuations are frozen, the effective impurity model inherits all the local quantum fluctuations and remains a quantum many-body problem which leads to energy-dependent self-energies.

Although, the local picture provided by DMFT has been successfully applied to various systems to reveal the underlying mechanisms of certain interesting phenomena (like the Mott transition), novel physics induced by non-local interactions and non-local correlations are beyond its scope. During the last decades, a lot of efforts have been made to include these effects in various extensions of the standard DMFT. Extended DMFT (EDMFT) was proposed [5] to include the screening effects of non-local interaction by a self-determined local retarded interaction, while the self-energy and polarization remain to be local. However, when non-local correlations start to play an important role, local approximations like DMFT and EDMFT are both insufficient to reveal the underlying physics. To overcome these shortcomings, further extensions have been proposed [6, 7] and they can be divided into two categories as:

- Cluster extensions in real or reciprocal space [8, 9, 10, 7]: Since DMFT can capture the correlations inside the impurity exactly, a natural extension is to extend the single-site impurity to a cluster in real or reciprocal space. Although, compared to the original lattice problem, the effective impurity model is easier to be handled and a lot of sophisticated methods, both analytical and numerical, have been developed (originating from the study of the Kondo effect [11] in impurity systems), solving it can still be very challenging and numerical expensive especially for systems with low symmetry. Hence, the cluster extensions are usually limited by the size of the cluster (smaller than 10×10 for high temperature calculations) that can be handled.

- Diagrammatic extensions which include Feynman diagrams that are not taken into account in the DMFT framework. Examples are, (E)DMFT+GW [12, 13, 14] which emphasizes on the charge fluctuations, and FLEX+DMFT [15] which emphasizes on the spin fluctuations. In order to avert the bias on the fluctuation channels, dual boson (DB) method [16, 17, 18, 19] and dynamical vertex approximation (DΓA) [20] promote the locality on the one-particle irreducible level to two-particle irreducible level. Hence, despite the fact that we only need to solve a single-site impurity model, further two-particle quantities which have three-frequency dependence are needed to close the self-consistent loops.

A balance between the capacity of interesting physics and computational costs is achieved by the TRILEX method proposed by Ayral and Parcollet [21, 22, 23, 24]. In this framework, fluctuations in charge- and spin-channel are treated on the same

footing and contribute to a momentum dependence on the fermonic self-energy and bosonic polarization functions, while the computational costs remain manageable as only the three-legged vertex as function of two frequencies needs to be computed.

This chapter is organized as follows: section 2.1 introduces the model which will be used throughout this chapter; section 2.2 discusses the self-consistency equations of DMFT and EDMFT; in section 2.3 we present the TRILEX self-consistency loop and its numerical implementations.

2.1 Modeling the long-range interaction

As indicated in Eq. (2.4), electrons in solids have two competing energies: a kinetic energy which favors the electrons to be delocalized, and a repulsive Coulomb interaction which favors the electrons to be localized. Such a competition between states being delocalized and localized provides the playground of fascinating phenomena in many-body systems. The minimal model that is able to capture this competing effect is the celebrated Hubbard model [25, 26, 27]. In its single-band form, the Hamiltonian reads

$$\mathcal{H} = -\sum_{ij,\sigma} t_{ij} c^\dagger_{i\sigma} c_{j\sigma} - \mu \sum_i n_i + U \sum_i n_{i\uparrow} n_{i\downarrow}, \tag{2.6}$$

where $c^\dagger_{i,\sigma}$ ($c_{i\sigma}$) creates (annihilates) an electron on site i with spin $\sigma \in \{\uparrow, \downarrow\}$. μ is the chemical potential. t_{ij} is the hopping amplitude between site i and j, U is the on-site Hubbard interaction. $n_i = n_{i\uparrow} + n_{i\downarrow}$ and $n_{i\sigma} = c^\dagger_{i\sigma} c_{i\sigma}$.

Despite its apparent simplicity, the Hubbard model has been a challenge since its introduction. Except for few specific cases, exact solutions, either analytical or numerical, of this model are absent. We can take two limits of this model to gain some insights:

- when $t/U \to \infty$, the Hamiltonian can be diagonalized through the Fourier transformation into momentum space. $\hat{H}(t/U \to \infty) \approx \sum_{\mathbf{k}\sigma} \epsilon(\mathbf{k}) c^\dagger_{\mathbf{k}\sigma} c_{\mathbf{k}\sigma}$. Its ground and excited states are just made up by single Slater determinant.

- when $t/U \to 0$, the Hamiltonian can be diagonalized in real space. At half-filling, its ground state is a degenerate state that has one electron per site. A

gain of energy U, representing the existence of a doubly occupied site caused by electron hopping, exhibits a charge gap between the ground state and the first excited state. Such a charge gap induced by electron interaction is called Mott gap and the underlying insulator is called Mott insulator.

The Coulomb interaction in the Hubbard model is assumed to be purely local because of the screening effects in solids. However, as we will see in the next chapter, in some systems, screening effects are not strong enough to screen the original Coulomb interaction into a short-range (or on-site) interaction, hence a long-range interaction with a $1/\mathbf{r}$ ($\mathbf{r}$ is the distance) tail can survive. To model this kind of systems, we can further add long-range density-density type interaction terms into the Hubbard model as,

$$H = -\sum_{ij,\sigma} t_{ij} c^{\dagger}_{i\sigma} c_{j\sigma} - \mu \sum_{i} n_i + \frac{1}{2} U_{ij} \sum_{ij} n_i n_j, \tag{2.7}$$

where U_{ij} is the interaction strength between site i and j

$$U_{ij} = U_0 \delta_{ij} + \frac{V}{|\mathbf{r}_i - \mathbf{r}_j|} \left(1 - \delta_{ij}\right), \tag{2.8}$$

where U_0 is the on-site Hubbard interaction strength, V is the nearest-neighbor interaction strength. Here, we have assumed the lattice constant to be 1.

The long-range interaction in momentum space can be formulated as:

$$U(\mathbf{q}) = U_0 + v(\mathbf{q}) = U_0 + V \sum_{i \neq 0} \frac{1}{|\mathbf{r}_i|} e^{i\mathbf{q}\cdot\mathbf{r}_i}. \tag{2.9}$$

The Madelung like lattice-sum in (2.9) prevents a direct numerical summation because of its slow spatial decay. To handle this difficulty, we follow the ideas of Ewald [28] and split the sum in terms of a short-range (first term) and a long-range (second term) contribution as

$$\nu(\mathbf{q})/V = \left(\sum_{\mathbf{r} \in \mathrm{BL} \setminus \{0\}} \frac{\mathrm{erfc}\left(|\mathbf{r}|/\eta\right)}{|\mathbf{r}|} e^{i\mathbf{q}\cdot\mathbf{r}} \right) + \left(\sum_{\mathbf{r} \in \mathrm{BL} \setminus \{0\}} \frac{\mathrm{erf}\left(|\mathbf{r}|/\eta\right)}{|\mathbf{r}|} e^{i\mathbf{q}\cdot\mathbf{r}} \right), \tag{2.10}$$

where η is a parameter controlling the summation range and satisfying $\sqrt{N} \ll \eta \lesssim N$,

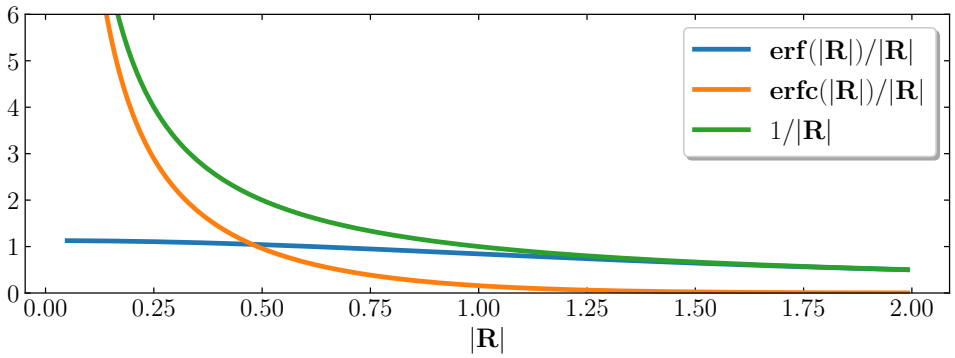

Figure 2.1: Decomposition of the long-range irregular function $1/|\mathbf{r}|$ into a short-range irregular one $\mathbf{erfc}(|\mathbf{r}|)/|\mathbf{r}|$ and a long-range regular one $\mathbf{erf}(|\mathbf{r}|)/|\mathbf{r}|$.

with N being the linear size of the lattice ($N = 64$ in our calculations). erf(x) is the error function and erfc(x) $= 1 -$ erf(x) its complementary. BL stands for sites in the Bravais lattice. In Fig. 2.1, we plot the behavior of the short- and long-ranged parts as a function of distance. The short-range, fast decaying $\mathrm{erfc}(|\mathbf{r}|)/|\mathbf{r}|$, although irregular when $|\mathbf{r}| \to 0$, can be evaluated accurately by numerical summation within η. For the long-range, but regular, $\mathrm{erf}(|\mathbf{r}|)/|\mathbf{r}|$ in two-dimension, an analytical summation can be performed as

$$\sum_{\mathbf{r}\in \mathrm{BL}\setminus\{0\}} \frac{\mathrm{erf}\left(|\mathbf{r}|/\eta\right)}{|\mathbf{r}|} e^{i\mathbf{q}\cdot\mathbf{r}} \approx \tag{2.11}$$
$$\int_0^\infty \rho d\rho \int_0^{2\pi} d\theta \frac{\mathbf{erc}(\rho/\eta)}{\rho} e^{i|\mathbf{q}|\rho\cos\theta} - \lim_{|\mathbf{r}|\to 0} \frac{\mathrm{erf}\left(|\mathbf{r}|/\eta\right)}{|\mathbf{r}|} e^{i\mathbf{q}\cdot\mathbf{r}} =$$
$$\frac{2\pi}{|\mathbf{q}|}\mathbf{erfc}\left(\frac{|\mathbf{q}|\eta}{2}\right) - \frac{2}{\eta\sqrt{\pi}}.$$

Thus, we have the final formula for long-range interaction in momentum space as

$$v(\mathbf{q}) = V\left(\sum_{\substack{\mathbf{r}\in \mathrm{BL}\setminus\{0\} \\ |\mathbf{r}|<N}} \frac{\mathrm{erfc}\left(|\mathbf{r}|/\eta\right)}{|\mathbf{r}|} e^{i\mathbf{q}\cdot\mathbf{r}} + \frac{2\pi}{|\mathbf{q}|}\mathrm{erfc}\left(\frac{|\mathbf{q}|\eta}{2}\right) - \frac{1}{\eta}\frac{2}{\sqrt{\pi}}\right). \tag{2.12}$$

The divergence as $|\mathbf{q}| \to 0$ can be handled by either a small shift of the whole Brillouin zone, or by putting a cutoff of $\mathbf{q}$. In the end, such a shift of the Brillouin zone or

cutting off should not influence the final results.

2.2 DMFT and EDMFT self-consistency equations

In this section, we present the DMFT and EDMFT self-consistency equations following the cavity approach [29, 30, 5] and put emphasis on the Luttinger-Ward functional which indicates the level of approximation of these two methods. But before that, we first consider the mean-field theory introduced by Weiss [31] that can provide an intuitive picture about the quantities we are going to introduce. A prototypical example of the mean-field solution is the Ising model whose Hamiltonian reads

$$H = -J \sum_{\langle ij \rangle} s_i s_j - h \sum_i s_i, \tag{2.13}$$

where J is the coupling strength between two neighboring classical spins $s_i = \pm 1$. h is an external magnetic field coupled locally with each spin. Here we assume $J > 0$ which favors a ferromagnetic ground state. The relevant degrees of freedom we choose to construct the mean-field solution is the averaged magnetic order $m = \langle s_i \rangle$. Then, after decoupling the interacting terms by neglecting spatial fluctuations, we end up with an effective Hamiltonian $H_{\text{eff}}[h_{\text{eff}}] = -h_{\text{eff}} s$. With $h_{\text{eff}} = Jzm + h$ being the Weiss field, the self-consistency condition is enforced by requiring $\langle s \rangle_{\text{eff}} = m$. Here, we notice that m is a lattice quantity while $\langle s \rangle_{\text{eff}}$ is an impurity quantity. Similarly, in (E)DMFT, we follow the same strategy by first isolating a site and then taking the infinite dimension limit $d \to \infty$. In this limit, the single-particle Green's function G and fully screened interaction W then serves as m in the Ising model.

The grand-canonical partition function $\mathcal{Z} = \operatorname{tr} e^{-\beta \mathcal{H}}$ can be written as

$$\mathcal{Z} = \int \mathcal{D}[\bar{c}_i, c_i] e^{-\mathcal{S}}, \tag{2.14}$$

$$\mathcal{S} = \int_0^\beta d\tau \left\{ \sum_{ij,\sigma} \bar{c}_{i\sigma}(\tau)[(\partial_\tau - \tilde{\mu})\delta_{ij} + t_{ij}] c_{j\sigma}(\tau) + \frac{1}{2} \sum_{ij} U_{ij} n_i(\tau) n_j(\tau) \right\},$$

with a shifted chemical potential $\tilde{\mu} = \mu + \frac{U}{2}$. $\beta = 1/T$ is the inverse temperature. $c_{i\sigma}$

($\overline{c}_{i\sigma}$) is the (conjugated) Grassmann antiperiodic field. To decouple the interacting term, we can introduce a bosonic field ϕ_i which couples with the electron density n_i locally by a Hubbard-Stratonovich transformation of the form

$$\exp\left\{\frac{1}{2}\int_0^\beta d\tau n_i(\tau)U_{ij}n_j(\tau)\right\} = \tag{2.15}$$
$$\int \mathcal{D}\left[\phi_i\right]\exp\left\{\int_0^\beta d\tau\left(\frac{1}{2}\phi_i(\tau)\left[-U^{-1}\right]_{ij}\phi_j(\tau)\pm\phi_i(\tau)n_i(\tau)\right)\right\}.$$

Now, the action $\mathcal{S}$ has an additional dependence on the bosonic field ϕ_i

$$\mathcal{S}[\overline{c}_i,c_i,\phi_i] = \int_0^\beta d\tau d\tau'\left\{-\sum_{ij,\sigma}\overline{c}_{i\sigma}(\tau)\left[\left(G_0\right)^{-1}(\tau-\tau')\right]_{ij}c_{j\sigma}(\tau')\right\} \tag{2.16}$$
$$+\int_0^\beta d\tau\left\{\frac{1}{2}\sum_{ij}\phi_i(\tau)\left[U^{-1}\right]_{ij}\phi_j(\tau)+i\alpha\sum_i\phi_i(\tau)n_i(\tau)\right\},$$

with the free lattice Green's function defined as $\left[\left(G_0\right)^{-1}\right]_{ij} = -[(\partial_\tau-\tilde{\mu})\delta_{ij}+t_{ij}]$. By introducing a real bosonic field ϕ_i which couples the electron density locally, the pure electron-electron interaction is replaced by an electron-boson interaction. The advantage of using an electron-boson interaction is that in such a form the screening effects can be monitored in an intuitive manner. α is the elctron-boson interaction strength, and the physical relevant case is $\alpha = 1$.

The generating functional for the electron propagator $G_{ij}(\tau,\tau') = -\langle\mathcal{T}c_i(\tau)\overline{c}_j(\tau')\rangle$, and boson propagator $W_{ij}(\tau,\tau') = \langle\mathcal{T}\phi_i(\tau)\phi_j(\tau')\rangle$ can be constructed by introducing the bilinear source fields B and F

$$\Omega\left[B,F\right] = -\ln\int\mathcal{D}\left[B,F\right]e^{-\mathcal{S}[\overline{c},c,\phi]+\mathcal{S}[B,F]}, \tag{2.17}$$

$$\mathcal{S}\left[B,F\right] = \int_0^\beta d\tau d\tau'\sum_{ij}\left(\overline{c}_{i\sigma}(\tau)F_{ij}(\tau,\tau')c_{j\sigma}(\tau')+\frac{1}{2}\phi_i(\tau)B_{ij}(\tau,\tau')\phi_j(\tau')\right). \tag{2.18}$$

The propagators can be obtain by $G_{ij}(\tau,\tau') = \delta\Omega/\delta F_{ij}(\tau,\tau')|_{F_{ij}\to 0}$ and $W_{ij}(\tau,\tau') = -2\,\delta\Omega/\delta B_{ij}(\tau,\tau')|_{B_{ij}\to 0}$. A transformation of functional dependence on the source

fields to the propagators can be achieved by a Legendre transformation as

$$\Gamma[W,G] = \Omega[B,F] - \mathrm{Tr}[FG] + \frac{1}{2}\mathrm{Tr}[BW]. \tag{2.19}$$

Then, the condition that requires the source filed to vanish in the evaluation of G and W is accomplished by simply requiring $\Gamma[W,G]$ to be stationary with respect to G and W, i.e., $F = -\frac{\delta\Gamma}{\delta G} = 0$ and $B = 2\frac{\delta\Gamma}{\delta W} = 0$. Γ is the famous Baym-Kadanoff functionals [32, 33]. We can further separate the non-interacting and interacting part in Γ by

$$\Gamma[W,G] = \Gamma_0 + \Psi[W,G]. \tag{2.20}$$

Here Γ_0 corresponds to the case of no electron-boson coupling and its formula is straightforwardly to compute. Ψ is the extension of electron Luttinger-Ward functional which has only a functional dependence on G to a functional dependence on both G and W. The self-energy for the electron and boson can be obtained by $\Sigma = \frac{\delta\Psi}{\delta G}$ and $\Pi = -2\frac{\delta\Psi}{\delta W}$.

Now, it is obvious that different approximation frameworks correspond to different approximations on $\Psi[W,G]$. The first non-trivial approximation can be obtained as

$\Sigma =$  ,
$\Pi =$  , (2.21)

which is the GW approximation. Comparing to the Fork diagram, the bare interaction U_{ij} is replaced by the fully screened interaction W_{ij}. Furthermore, we can directly see that the screening effects originate from the particle-hole process represented by the bubble diagram in Eq. (2.21).

Now, we are ready to adapt the standard cavity method to map our lattice model to an impurity model by separating our action (2.16) into three parts $\mathcal{S} = \mathcal{S}_0 + \mathcal{S}_{(0)} + \Delta\mathcal{S}$, corresponding to the action of site 0, the action of the remaining lattice with a

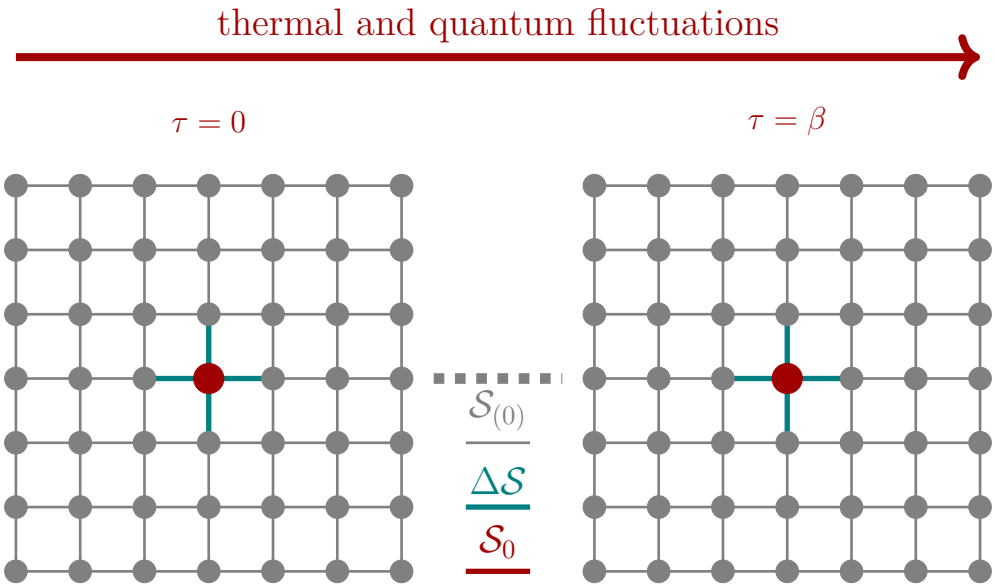

Figure 2.2: Illustration of the separation of the lattice action. $\mathcal{S}_0$ represents the thermal and quantum fluctuations on the impurity site; $\mathcal{S}_{(0)}$ represents the action of the rest of the lattice with a cavity at site 0; $\Delta\mathcal{S}$ represents the hybridization between the impurity site 0 and the rest of the lattice.

cavity at site 0, and the hybridization terms between them

$$\mathcal{S}_0[\bar{c}, c, \phi] = \int_0^\beta d\tau \left\{ \bar{c}_0(\tau)(\partial_\tau - \mu)c_0(\tau) + i\alpha\phi_0(\tau)n_0(\tau) + \frac{1}{2}\phi_0(\tau)U_{00}^{-1}\phi_0(\tau) \right\} \tag{2.22}$$

$$\mathcal{S}_{(0)}[\bar{c}, c, \phi] = \int_0^\beta d\tau \left\{ - \sum_{i\neq 0, j\neq 0} \bar{c}_i(\tau) \left[G_0^{-1}(\tau)\right]_{ij} c_j(\tau) \right\}, \tag{2.23}$$

$$+ \int_0^\beta d\tau \left\{ \frac{1}{2} \sum_{i\neq 0, j\neq 0} \phi_i(\tau) \left[U^{-1}\right]_{ij} \phi_j(\tau) + i\alpha \sum_{i\neq 0} \phi_i(\tau) n_i(\tau) \right\},$$

$$\Delta\mathcal{S}[\bar{c}, c, \phi] = \int_0^\beta d\tau \left\{ - \sum_{i\neq 0} t_{i0} \left[\bar{c}_0(\tau)c_i(\tau) + \bar{c}_i(\tau)c_0(\tau)\right] + \sum_{i\neq 0} \phi_i(\tau)U_{i0}^{-1}\phi_0(\tau) \right\}. \tag{2.24}$$

Such a separation is illustrated in Fig. 2.2.

Since we want to go to the infinite dimension limit, in which the hopping and interaction terms need to be rescaled correctly, we can rewrite the hybridization term

as

$$\Delta\mathcal{S}[\overline{c},c,\phi]=\int_0^\beta d\tau\left\{-\sum_{i\neq 0}[\overline{c}_i(\tau)\eta_i(\tau)+\overline{\eta}_i(\tau)c_i(\tau)]+\sum_{i\neq 0}j_i(\tau)\phi_i(\tau)\right\}, \tag{2.25}$$

by defining $\eta_i(\tau)=t_{i0}c_0(\tau)$ and $j_i(\tau)=U_{i0}^{-1}\phi_0(\tau)$. To obtain an effective action of the impurity site 0, we need to integrate out the remaining lattice degrees of freedom represented by

$$\Omega[\overline{\eta},\eta,j]=\ln\int\mathcal{D}_{i\neq 0}[\overline{c}_i,c_i,\phi_i]e^{-\mathcal{S}_{(0)}-\Delta\mathcal{S}}. \tag{2.26}$$

Note that $\int\mathcal{D}[\overline{c}_0,c_0,\phi_0]e^{\Omega}=\mathcal{Z}$. We can define the effective action of site 0 by,

$$e^{-\mathcal{S}_{\mathbf{eff}}}/\mathcal{Z}_{\mathbf{eff}}=\int\mathcal{D}_{i\neq 0}[c_i^*,c_i,\phi_i]e^{-\mathcal{S}_{(0)}-\mathcal{S}_0-\Delta\mathcal{S}}/\mathcal{Z}. \tag{2.27}$$

Noting that $\Omega[\eta^*,\eta,j]$ can be viewed as the generating functional of the connected Green's function of the cavity lattice as

$$G^{(0)}_{i_1,\cdots,i_n,j_n,\cdots,j_1}(\tau_1,\cdots,\tau_n,\tau_n',\cdots,\tau_1')=(-1)^n\frac{\delta^{2n}\Omega[\overline{\eta},\eta,j]}{\delta\overline{\eta}_{i_1}(\tau_1)\cdots\delta\overline{\eta}_{i_n}(\tau_n)\delta\eta_{j_n}(\tau_n')\cdots\delta\eta_{j_1}(\tau_1')}, \tag{2.28}$$

$$W^{(0)}_{i_1,\cdots,i_n,j_n,\cdots,j_1}(\tau_1,\cdots,\tau_n,\tau_n',\cdots,\tau_1')=\frac{\delta^{2n}\Omega[\overline{\eta},\eta,j]}{\delta j_{i_1}(\tau_1)\cdots\delta j_{i_n}(\tau_n)\delta j_{j_n}(\tau_n')\cdots\delta j_{j_1}(\tau_1')},$$

which means that we can express the generating functional Ω as an exponential expansion of connected Green's functions, i.e.,

$$\begin{aligned}\Omega[\overline{\eta},\eta,j]=&\sum_{n=1}^{\infty}\sum_{i_1,\cdots,i_n,j_1,\cdots,j_n}\int_0^\beta\overline{\eta}_{i_1}(\tau_1)\cdots\overline{\eta}_{i_n}(\tau_n)\eta_{j_n}(\tau_n')\cdots\eta_{j_1}(\tau_1')\\&(-1)^nG^{(0)}_{i_1,\cdots,i_n,j_n,\cdots,j_n,\cdots,j_1}(\tau_1,\cdots,\tau_n,\tau_n',\cdots,\tau_1')+\\&\sum_{n=1}^{\infty}\sum_{i_1,\cdots,i_n,j_1,\cdots,j_n}\int_0^\beta j_{i_1}(\tau_1)\cdots j_{i_n}(\tau_n)j_{j_n}(\tau_n')\cdots j_{j_1}(\tau_1')\\&W^{(0)}_{i_1,\cdots,i_n,j_n,\cdots,j_n,\cdots,j_1}(\tau_1,\cdots,\tau_n,\tau_n',\cdots,\tau_1').\end{aligned} \tag{2.29}$$

The key simplification to this expansion series comes from the finding of Metzner and

Vollhardt [1]. They pointed out that in infinite dimension, the hopping terms need to be scaled as $t/\sqrt{z}$, while the interaction terms need to be scaled as V/z with z being the coordinate number. So, in order to keep the kinetic and interacting terms remaining comparable, the connected Green's function also has to be rescaled by $t/\sqrt{z}$. Then in the expansion series, any term containing orders of connected Green's function higher then $n = 1$ vanish! In the end, we arrive at

$$\Omega[\overline{\eta}, \eta, j] = \int_0^\beta d\tau d\tau' \left\{ -\sum_{i,j\neq 0} t_{i0} t_{j0} \overline{c}_0(\tau) G_{ij}^{(0)}(\tau - \tau') c_0(\tau') \right\} \tag{2.30}$$
$$+ \int_0^\beta d\tau d\tau' \left\{ \sum_{i,j\neq 0} U_{i0} U_{j0} \phi_0(\tau) W_{ij}^{(0)}(\tau - \tau') \phi_0(\tau') \right\}.$$

The effective action of the impurity site can be already written as (dropping the index 0)

$$\mathcal{S}_{\mathbf{eff}}[\overline{c}, c, \phi] = -\int_0^\beta \overline{c}(\tau) \mathcal{G}^{-1}(\tau) c(\tau) + \int_0^\beta \phi(\tau) \mathcal{U}^{-1}(\tau) \phi(\tau) + i \int_0^\beta \phi(\tau) n(\tau), \tag{2.31}$$

with $\mathcal{G}$ and $\mathcal{U}$ being the Weiss propagators of the electron and boson defined as

$$\mathcal{G}^{-1}(\tau) = -\partial_\tau + \mu - \sum_{i,j\neq 0} t_{i0} t_{j0} G_{ij}^{(0)}(\tau), \tag{2.32}$$

$$\mathcal{U}^{-1}(\tau) = \nu_{00}^{-1} - \sum_{i,j\neq 0} U_{i0} U_{j0} W_{ij}^{(0)}(\tau). \tag{2.33}$$

and their Fourier transformed counterpart

$$\mathcal{G}^{-1}(i\omega) = i\omega + \mu - \sum_{i,j\neq 0} t_{i0} t_{j0} G_{ij}^{(0)}(i\omega), \tag{2.34}$$

$$\mathcal{U}^{-1}(i\nu) = \nu_{00}^{-1} - \sum_{i,j\neq 0} U_{i0} U_{j0} W_{ij}^{(0)}(i\nu). \tag{2.35}$$

By further using the relation between the lattice propagator and cavity propaga-

tor, we finally arrive at the self-consisent equations of (E)DMFT for electron

$$G_{\mathbf{lat}}(\mathbf{k}, i\omega) = \frac{1}{i\omega + \mu - \epsilon_{\mathbf{k}} - \Sigma(i\omega)}, \tag{2.36}$$

$$G_{\mathbf{loc}}(i\omega) = \sum_{\mathbf{k}} G_{\mathbf{lat}}(\mathbf{k}, i\omega), \tag{2.37}$$

$$\mathcal{G}(i\omega) = \frac{1}{G^{-1}_{\mathbf{loc}}(i\omega) + \Sigma(i\omega)}, \tag{2.38}$$

and for boson

$$W_{\mathbf{lat}}(\mathbf{q}, i\nu) = \frac{1}{U^{-1}(\mathbf{q}) - \Pi(i\nu)}, \tag{2.39}$$

$$W_{\mathbf{loc}}(i\nu) = \sum_{\mathbf{q}} W_{\mathbf{lat}}(\mathbf{q}, i\nu), \tag{2.40}$$

$$\mathcal{U}(i\nu) = \frac{1}{W^{-1}_{\mathbf{loc}}(i\nu) + \Pi(i\nu)}. \tag{2.41}$$

The self-consistency conditions of this set of equations are $\Sigma_{\mathbf{loc}}(i\omega) = \Sigma_{\mathbf{imp}}(i\omega)$ and $\Pi_{\mathbf{loc}}(i\nu) = \Pi_{\mathbf{imp}}(i\nu)$. Here quantities with subscript "**imp**" or "**loc**" stand for the impurity or local lattice quantities. For DMFT, we only need to compute the impurity self-energy, while for EDMFT, we need to further compute the impurity polarization with an retarded local interaction $\mathcal{U}(i\nu)$.

The term "dynamical" in DMFT now has a very intuitive illustration: the static hopping (t_{0i}) and interaction (U_{0i}) terms between the impurity site and cavity lattice sites are replaced by two time-dependent Weiss propagators $\mathcal{G}(\tau)$ and $\mathcal{U}(\tau)$ which mimic the effects of the cavity lattice on the impurity site.

Furthermore, we can see from the self-consistency equations for the bosonic field that the screening effects contain two categories of contributions: one category of contributions are generated by the particle-hole processes induced by the hybridization between the cavity lattice and the impurity site; another category of contributions originate from the particle-hole process inside the impurity. For the first kind of contributions, there are two possible sources: the first source is that the bare interaction has an explicit momentum dependence, i.e., the system has non-local interactions; the second source is the bare interaction has a dynamic character, for instance, the bare interaction obtained from a downfolding process, like cRPA [34], will maintain a dynamical nature. Hence, if there is no non-local interaction and the bare interaction

is static, the set of self-consistency equations returns to the normal DMFT ones which just require a self-consistency determination of the electron self-energy.

2.3 A local approximation to the three-legged vertex: TRILEX

As discussed in last section Sec. (2.2), local approximations like DMFT and EDMFT which approximate the Luttinger-Ward functional by its local contributions, are able to capture the local fluctuations but totally neglect the spatial fluctuations. These, however, are key to some of the most exciting phenomena (especially in low dimensions and low temperatures). For instance, the short-range spin fluctuations is proposed to be the source of high-T_c superconductivity in cuprates.

In this section, we present the TRILEX approximation which aims at including non-local fluctuations while keeping the computational cost manageable [21, 22, 24]. As already shown in Equation (2.16), an electron-electron interacting action can be rewritten as an electron-boson action by introducing a bosonic field coupled locally with the electron density. In the EDMFT construction, a real bosonic field is introduced, leading to a self-consistent determination of the charge fluctuations, while the spin fluctuations are ignored. Following this line, we can include the spin fluctuations by reintroducing another bosonic field which couples with the local spin operators $\{s_x, s_y, s_z\}$. To do this, we need to first decouple our interaction term and rewrite it as a combination of spin and charge contributions as

$$\frac{U}{2}nn = \frac{1}{2}\sum_I U^I n_I n_I, \tag{2.42}$$

here $I = \{0, x, y, z\}$ and $n_0 = n = n_\uparrow + n_\downarrow$, $n_x = s_x$, $n_y = s_y$ and $n_z = s_z$. If the underlying Hamiltonian has $SU(2)$ symmetry, we can choose $U^0 = U^{\mathbf{ch}}$, and $U^x = U^y = U^z = U^{\mathbf{sp}}$. The superscript "**ch**" and "**sp**" correspond to charge- and spin-channel, respectively. Requiring the decoupled interaction to be equal to the original one, we have $U = U^{\mathbf{ch}} - 3U^{\mathbf{sp}}$. Such a decoupling is called Heisenberg decoupling.

Now, we are ready to extend the electron-boson action in Eq. (2.16) to a more

general form,

$$\mathcal{S}_{\rm eb} = \overline{c}_{\overline{\mu}} \left[-G_0^{-1}\right]_{\overline{\mu}\nu} c_\nu + \frac{1}{2}\phi_\alpha \left[-W_0^{-1}\right]_{\alpha\beta} \phi_\beta + \lambda_{\overline{\mu}\nu\alpha}\overline{c}_{\overline{\mu}} c_\nu \phi_\alpha, \tag{2.43}$$

with Grassmann fields $\overline{c}_{\overline{\mu}}$ and c_ν which describe fermionic degrees of freedom. The μ (ν) index represents a collection of possible space R_μ (R_ν), time τ_μ (τ_ν), and spin σ_μ (σ_ν) indices. If the index is equipped with (without) a over line, it stands for an outgoing (incoming) direction. ϕ_α is the real bosonic fields, and the index α (β) represents a collection of space R_α (R_β), time τ_α (τ_β) and bosonic channel I_α (I_β) indices. G_0 and W_0 are the free electron and boson propagators. $\lambda_{\overline{\mu}\nu\alpha}$ stands for a general electron-boson coupling constant. All repeated indices are summed over.

Now, we can define the free energy of the system with external sources (h, B, F, λ) which are coupled with the fermionic, bosonic degrees of freedom,

$$\Omega\left[h, B, F, \lambda\right] = -\ln \int \mathcal{D}[\overline{c}, c, \phi] e^{-\mathcal{S}_{\rm eb} + h_\alpha \phi_\alpha - \frac{1}{2}\phi_\alpha B_{\alpha\beta}\phi_\beta - \overline{c}_{\overline{\mu}} F_{\overline{\mu}\nu} c_\nu}. \tag{2.44}$$

Note that, since λ in the $\mathcal{S}_{\rm eb}$ already plays the role of trilinear source field, we do not need to further introduce another one for the electron-bonson coupling operator $\overline{c}c\phi$. The definition of $\Omega\left[h, B, F, \lambda\right]$ can be used as the generator for correlation functions as

$$\varphi_\alpha = \langle \phi_\alpha \rangle = -\left.\frac{\partial \Omega}{\partial h_\alpha}\right|_{B,F,\lambda}, \tag{2.45}$$

$$W^{\mathbf{nc}}_{\alpha\beta} = -\langle \phi_\alpha \phi_\beta \rangle = -2\left.\frac{\partial \Omega}{\partial B_{\beta\alpha}}\right|_{h,F,\lambda}, \tag{2.46}$$

$$G_{\mu\overline{n}\overline{u}} = -\langle c_\mu \overline{c}_{\overline{\nu}} \rangle = -\left.\frac{\partial \Omega}{\partial F_{\overline{\nu}\mu}}\right|_{h,B,\lambda}. \tag{2.47}$$

The superscript "**nc**" in $W^{\mathbf{nc}}$ indicates that it contains non-connected terms. To change the variable from the external sources to correlation functions, we can perform a Legendre transformation with respect to the external sources as

$$\Gamma_2\left[\varphi, W, G, \lambda\right] = \Omega\left[h, B, F, \lambda\right] - \mathrm{tr}\, FG + \frac{1}{2}\,\mathrm{tr}\, BW^{\rm nc} + \mathrm{tr}\, h\varphi. \tag{2.48}$$

Here $\mathrm{tr}\, HJ = \sum_{\overline{\mu}\nu} H_{\overline{\mu}\nu} J_{\nu\overline{\mu}}$. Now, the sources can be generated by the derivatives of

Γ_2 through

$$h_\alpha = \left.\frac{\partial \Gamma_2}{\partial \varphi_\alpha}\right|_{W^{\mathrm{nc}},G,\lambda}, \tag{2.49}$$

$$B_{\alpha\beta} = 2\left.\frac{\partial \Gamma_2}{\partial W^{\mathrm{nc}}_{\beta\alpha}}\right|_{\varphi,G,\lambda}, \tag{2.50}$$

$$F_{\bar{\mu}\nu} = -\left.\frac{\partial \Gamma_2}{\partial G_{\nu\bar{\mu}}}\right|_{\varphi,W,\lambda}. \tag{2.51}$$

In the fermionic context, similar to the construction of the EMDFT approximation, Γ_2 is the Baym-Kadanoff functional [32, 33]. One can separate Γ_2 into

$$\Gamma_2\left[\varphi, W^{\mathrm{nc}}, G, \lambda\right] = \Gamma_2\left[\varphi, W^{\mathrm{nc}}, G, \lambda = 0\right] + \Psi\left[\varphi, W^{\mathrm{nc}}, G, \lambda\right], \tag{2.52}$$

with $\Gamma_2\left[\varphi, W^{\mathrm{nc}}, G, \lambda = 0\right]$ being the noninteracting contributions, which can be computed straightforwardly. Since Ψ contains all the interacting information, by inserting equation (2.52) into equations (2.49) and requiring $B = F = 0$, we obtain the Dyson equation for fermionic and bosonic fields as

$$\frac{\partial \Psi}{\partial G_{\nu\bar{\mu}}} = \Sigma_{\bar{\mu}\nu} = \left[G_0^{-1}\right]_{\bar{\mu}\nu} - \left[G^{-1}\right]_{\bar{\mu}\nu}, \tag{2.53}$$

$$-2\frac{\partial \Psi}{\partial W_{\beta\alpha}} = P_{\alpha\beta} = \left[W_0^{-1}\right]_{\alpha\beta} - \left[W^{-1}\right]_{\alpha\beta}. \tag{2.54}$$

Similar to its fermonic counterpart, i.e., the Luttinger-Ward functional, $\Psi\left[\varphi, W, G, \lambda\right]$ contains two-particle irreducible diagrams composed by fermionic (G) and bosonic (W) propagators, and the bare electron-boson interaction vertex λ. Different approximations to Ψ leads to various kinds of approximation for the fermionic and bosonic self-energies. For instance, the (E)DMFT approximation corresponds to

$$\Psi^{\mathrm{DMFT}} \approx \Psi\left[G_{\mathrm{loc}}\right], \Psi^{\mathrm{EDMFT}} \approx \Psi\left[W_{\mathrm{loc}}, G_{\mathrm{loc}}\right]. \tag{2.55}$$

Instead of approximating Ψ to be local on the single-particle level, TRILEX promotes the locality to the level of the three-legged diagrams. To achieve this, we

introduce another Legendre transformation

$$\Gamma_3\left[\varphi, W, G, \chi^{\mathrm{nc}}\right] = \Gamma_2\left[\varphi, W, G, \lambda\right] + \lambda_{\bar{\mu}\nu\alpha}\chi^{\mathrm{nc}}_{\mu\bar{\nu}\alpha}, \tag{2.56}$$

with the three-point correlation function $\chi^{\mathrm{nc}}_{\mu\bar{\nu}\alpha}$ (containing non-connected contributions) defined as

$$\chi^{\mathrm{nc}}_{\mu\bar{\nu}\alpha} = \langle c_\mu \bar{c}_{\bar{\nu}} \phi_\alpha \rangle = -\left.\frac{\partial\Omega}{\partial\lambda_{\mu\bar{\nu}\alpha}}\right|_{h,B,F}. \tag{2.57}$$

Its connected counterpart is defined as

$$\chi_{\mu\bar{\nu}\alpha} = \langle c_\mu \bar{c}_{\bar{\nu}} \left(\phi_\alpha - \varphi_\alpha\right)\rangle = \chi^{\mathrm{nc}}_{\mu\bar{\nu}\alpha} + G_{\mu\bar{\nu}}\varphi_\alpha. \tag{2.58}$$

The three-particle irreducible functional now can be defined as

$$\mathcal{K}\left[\varphi, W, G, \Lambda\right] = \Psi\left[\varphi, G, W, \lambda\right] + \lambda_{\bar{\nu}\mu\alpha}\chi^{\mathrm{nc}}_{\mu\bar{\nu}\alpha} - \frac{1}{2}\Lambda_{\bar{x}\mu\alpha}G_{w\bar{x}}G_{\mu\bar{v}}W_{\alpha\beta}\Lambda_{\bar{\nu}w\beta}, \tag{2.59}$$

with Λ being the amputated, connected correlation function

$$\Lambda_{\bar{\nu}\mu\alpha} = \left[G^{-1}\right]_{\bar{x}\mu}\left[G^{-1}\right]_{\bar{\nu}w}\left[W^{-1}\right]_{\alpha\beta}\chi_{w\bar{x}\beta}. \tag{2.60}$$

The Dyson-like equation on the three-particle irreducible level can be obtained as

$$\Lambda_{\bar{\nu}\mu\alpha} = \lambda_{\bar{\nu}\mu\alpha} + K_{\bar{\nu}\mu\alpha}, \tag{2.61}$$

$$K_{\bar{\nu}\mu\alpha} = -\left[G^{-1}\right]_{\bar{x}\mu}\left[G^{-1}\right]_{\bar{\nu}w}\left[W^{-1}\right]_{\alpha\beta}\frac{\partial\mathcal{K}}{\partial\Lambda_{\bar{x}w\beta}}. \tag{2.62}$$

The fermionic and bosonic self-energies are thus related with Λ by

$$\Sigma_{\bar{\mu}\nu} = -\lambda_{\bar{\mu}\omega\alpha}G_{\omega\bar{x}}W_{\alpha\beta}\Lambda_{\bar{x}\nu\beta} + \lambda_{\bar{\mu}\nu\alpha}\varphi_\alpha, \tag{2.63}$$

$$P_{\alpha\beta} = \lambda_{\bar{\mu}\omega\alpha}G_{\nu\bar{\mu}}G_{\omega\bar{x}}\Lambda_{\bar{x}\nu\beta}. \tag{2.64}$$

TRILEX approximates the three-particle irreducible functional as

$$\mathcal{K}\left[W, G, \chi\right] \approx \sum_{\mathbf{R}} \mathcal{K}\left[G_{\mathbf{RR}}, W_{\mathbf{RR}}, \chi_{\mathbf{RRR}}\right], \tag{2.65}$$

meaning that it only contains the local contributions! Similar to the local self-energies induced by the local approximation of Ψ in (E)DMFT on the two-particle irreducible level, here, the local approximation of $\mathcal{K}$ leads to a local Λ on the three-particle level

$$K\left(\mathbf{k},\mathbf{q};i\omega,i\nu\right)\approx K\left(i\omega,i\nu\right), \tag{2.66}$$

which is obtained, together with Eq. (2.61), from the the auxiliary impurity quantities

$$\chi^{\eta}_{\mathbf{RRR}}(i\omega,i\nu)=\chi^{\eta}_{\mathrm{imp}}(i\omega,i\nu), \tag{2.67}$$

$$G_{\mathbf{RR}}(i\omega)=G_{\mathrm{imp}}(i\omega), \tag{2.68}$$

$$W_{\mathbf{RR}}(i\nu)=W_{\mathrm{imp}}(i\nu). \tag{2.69}$$

The self-consistency is achieved by Eqs. (2.60)(2.61)(2.63)(2.67). From here we can see that, compared with (E)DMFT, TRILEX requires to compute the three-legged vertex from the impurity solver, which leads to an increase of the computational costs. However, compared with DΓA which requires to compute the two-particle irreducible vertex which depends on 3 frequencies, the three-legged vertex only has 2 frequency variables and thus is computational much more accessible.

3

The impact of long-range interaction on the emergence of unconventional superconductivity

Parts of the contents presented in this chapter have been published in "Chiral $d-$wave superconductivity in a triangular surface lattice mediated by long-range interaction", **Xiaodong Cao**, Thomas Ayral, Zhicheng Zhong, Olivier Parcollet, Dirk Manske, and Philipp Hansmann, ***Phys. Rev. B 97, 155145, 20 April 2018***

Since the discover of high-T_c superconductivity in cuprates [35], enormous efforts, both experimentally and theoretically, have been made in the search of new candidates for unconventional superconductivity. Although the original intention of research on the $Ba_xLa_{5-x}Cu_5O_{5(3-y)}$ compound was to seek after materials with large electron-phonon coupling, this system and the entire cuprate family have opened a new research field on materials beyond the BCS theory. These materials become superconducting at a critical temperature far above the "conventional" superconductors described by BCS theory. A timeline of the discovery of superconductors and their T_c is depicted in Fig 3.1.

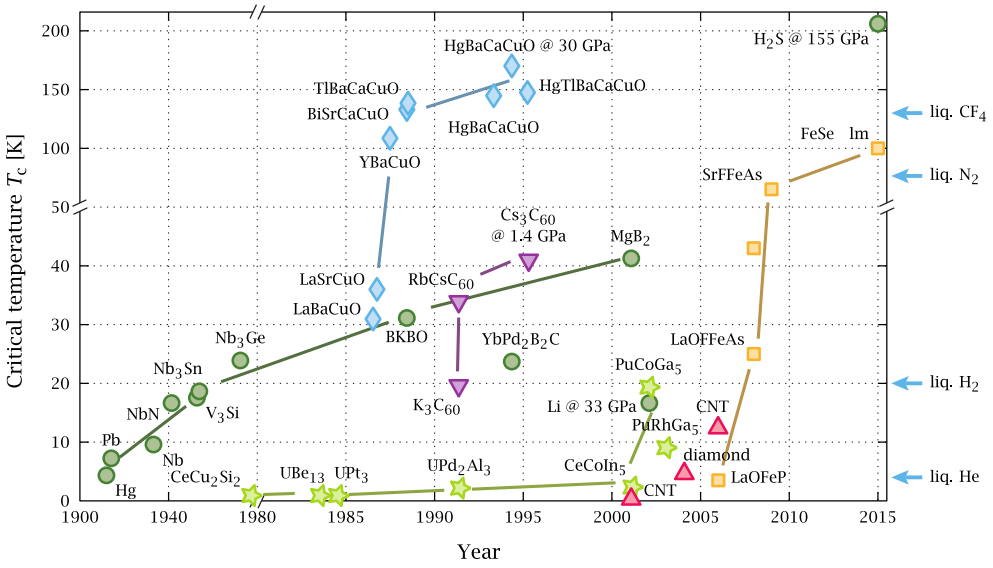

Figure 3.1: Timeline (from Wikipedia) of discover of superconductors. Green circles represent the BCS superconductors, blue diamonds represent the cuprates and yellow squares represent the iron-based superconductors.

Although, extensive efforts have been made to understand the paring mechanism in unconventional superconductors, a unified theory is still missing. One of the main encumbrances originates from the complexity of these materials. Usually, to have a concrete theoretical understanding of a system, we first derive a minimal low energy model which is able to capture the relevant physics while remaining as simple as possible. Although, the two-dimensional copper-oxygen plane plays a central role in cuprates, to have an effective low energy model which describes the correct competing energy scales is still very challenging. For instance, in $La_{2-x}Sr_xCuO_4$ (LSCO), the nominal valence configuration is Cu $3d^9$ and O $2p^6$. The degeneracy of the Cu d orbitals is lifted (into two $e_g(x^2-y^2$ and $3z^2-r^2)$ and three $t_{2g}(xy,\ yz,\ zx)$ levels) by the cubic environment. A tetragonal distortion further splits these d levels into four distinct levels (x^2-y^2, $3z^2-r^2$, xy and degenerate xz and yz levels in energy descending order) and the oxygen $2p$ orbitals into σ and π levels. By symmetry argument, only the in-plane $d_{x^2-y^2}$ and two σ levels will strongly hybridize with each other. Hence, the minimal model we can adapt is a three band model that includes these three hybridizing levels.

The hybridizing $d_{x^2-y^2}$ and (p_x, p_y) orbitals form three distinct levels including a

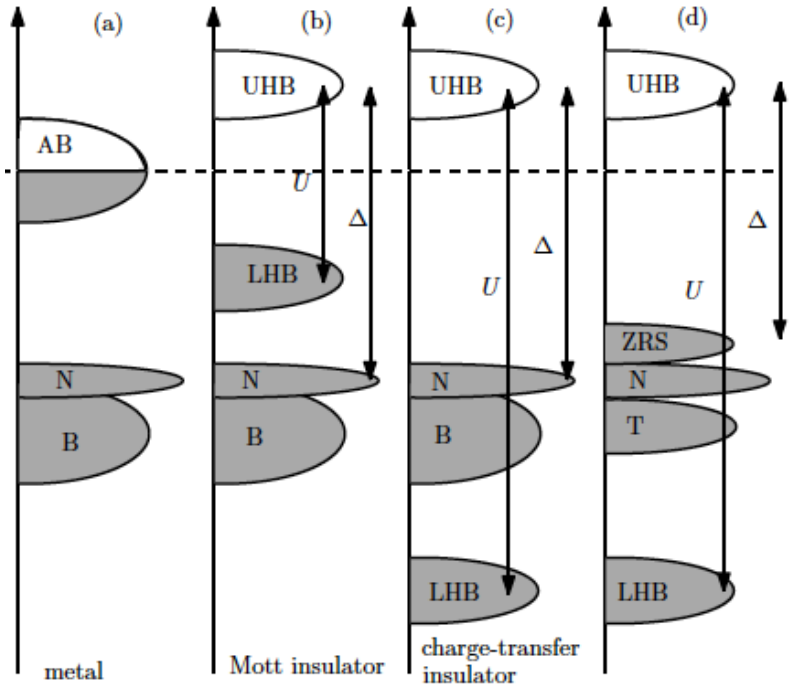

Figure 3.2: Stretch of various scenarios by comparing the Hubbard interaction U on $d_{x^2-y^2}$ orbital and charge-transfer energy $\Delta = \epsilon_d - \epsilon_p$. LHB stands for lower Hubbard band; UHB stands for upper Hubbard band; ZRS stands for Zhang-Rice Singlet band and T for Triplet band. (adapted from [36].)

pair of bonding (B) and anti-bonding (AB) bands, and a non-bonding (NB) band, see Fig. 3.2(a). The AB band is half-filled while the NB and AB bands are fully occupied. If the single-particle energy split $\Delta = \epsilon_d - \epsilon_p$, where $\epsilon_{d,p}$ is the on-site potential on d and p orbitals , is much larger than the on-site interaction U on the $d_{x^2-y^2}$ orbital, then we have a Mott-insulator, and an effective single-band model describing the AB band only is sufficient (the NB and B bands can be ignored safely), see Fig. 3.2(b). However, this is not the case in cuprates in which we have $U \gg \Delta$. In this case, we have a charge-transfer insulator [37] instead of a Mott-insulator, see Fig. 3.2(c). Furthermore, the holes in the AB band and electron on the B band will hybridize and form the famous Zhang-Rice singlet (ZRS) and triplet (ZRT) [38], see Fig. 3.2(d). Thus, the downfolding to a single-band model should be verified carefully in the context of cuprates! Hence, an alternative system, which can be described by a simper low energy model and also be experimentally well controlled,

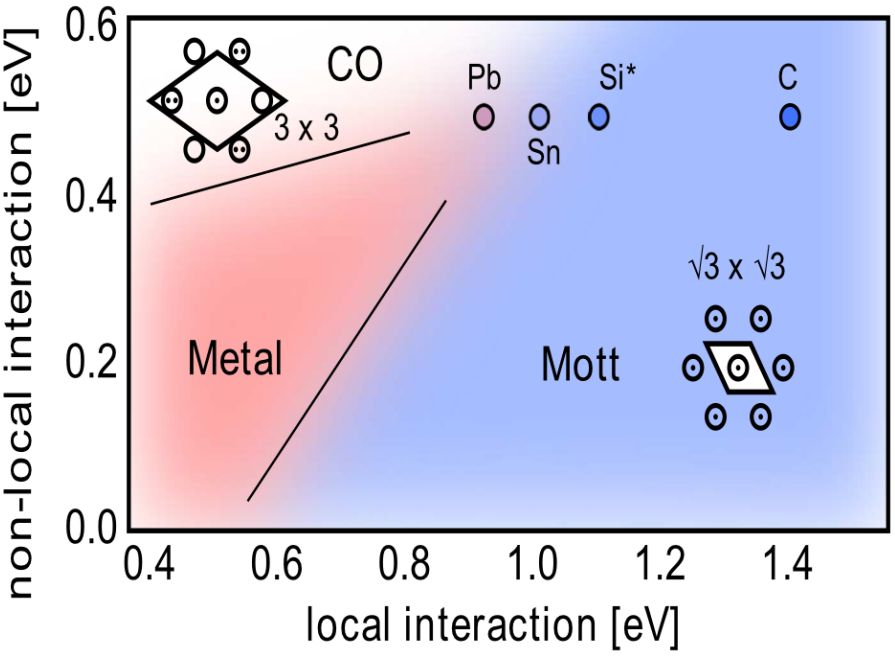

Figure 3.3: Phase diagram at half-filling as function of on-site interaction strength U and long-range interaction strength V. The inserts sketches show the unit cell and occupation patterns in the Mott and stripe (3×3 geometry) phases. Taken from [41].

is highly desirable for the understanding of cuprates.

In recent years, sophisticated synthesis technology allows for the construction of new materials like heterostructures or surface systems on an atomic length scale. Many-body studies on experimentally well controlled correlated adatom lattices X:Si(111) and X:Ge(111) with (X=Pb,Sn,C) revealed that these systems are good playground of interesting physics induced by correlation effects [39, 40, 41, 42, 43]. Furthermore, because of the simplicity of these systems, an effective single-band model can be derived, and it provides an unified phase diagram [41] for various variants at half-filling. As summarized in Fig. 3.3, due to sizable long-range interaction in the triangular lattice geometry, some of the materials were shown to be in close vicinity to a triple point between a Fermi liquid, a Mott insulator, and a charge-ordered insulator. Sn:Si(111) and Pb:Si(111) in particular turned out to be close to a charge-order Mott insulator phase transition with sizable charge fluctuations visible in core level spectroscopy [43] of Sn:Si(111). In complementary studies [42] the importance of spin fluctuations in

Sn:Si(111) was emphasized. Such materials are, hence, promising candidates to search for unconventional superconductivity.

In this chapter, we show that the triangular lattice model for the adatom materials has a dome shaped superconducting phase of chiral d-wave symmetry as a function of hole doping in realistic parameter regimes. The long-range interaction is key for enhanced critical temperatures and distinguishes the adatom Hamiltonian from triangular Hubbard models [44, 45, 46, 47, 48, 49, 50, 51]. By analyzing spin- and charge response functions we further show that the pairing mechanism crosses over from a cumulative spin/charge fluctuation character at small dopings to a charge dominated one at large doping.

3.1 Model and TRILEX implementation

The low energy Hamiltonian on the triangular lattice with long-range interaction reads:

$$H = \sum_{i,j,\sigma} t_{ij} \hat{c}^{\dagger}_{i\sigma} \hat{c}_{j\sigma} + \frac{1}{2} \sum_{i,j} U_{ij} \hat{n}_i \hat{n}_j - \mu \sum_i \hat{n}_i, \tag{3.1}$$

where $\hat{c}^{\dagger}_{i\sigma}$ ($\hat{c}_{i\sigma}$) are electron creation (annihilation) operators on site i with spin $\sigma = \uparrow, \downarrow$. $\hat{n}_i = \hat{n}_{i\uparrow} + \hat{n}_{i\downarrow}$ is the density operator on site i, and μ is the chemical potential. t_{ij} and U_{ij} are the hopping integrals and long-range Coulomb interaction strength between sites i and j. For translational invariant two-dimensional systems, the long-range Coulomb interaction, in momentum space, reads $U_{\mathbf{q}} = U_0 + V \sum_{i \neq 0} e^{i\mathbf{q}\cdot\mathbf{r}_i}/|\mathbf{r}_i|$ where $\mathbf{r}_i$ are real space coordinates, U_0 is the on-site interaction, and V is the strength of the long-range interaction respectively (See 2.1 for more details). More specifically, we adopt hopping parameters up to next-nearest-neighbors ($t = 0.042$eV and $t' = -0.02$eV) from [40, 41] derived from density functional theory (DFT) for the Pb:Si(111) adatom system (closest to the triple point, see Fig. 3.3) and vary the interaction parameters in realistic regimes for the adatom materials found by constrained random phase approximation [41].

As detailed in previous chapter, TRILEX approximates the three-legged fermion-boson interaction vertex using a local self-consistent quantum impurity model. For

systems retaining SU(2) symmetry, the self-consistent TRILEX equations [21, 22, 23, 24] for the fermionic single particle self-energy $\Sigma(\mathbf{k}, i\omega_n)$ and bosonic polarization in charge and spin channel $P^{\mathrm{c,s}}(\mathbf{q}, i\nu_n)$ can be rewritten as:

$$\begin{aligned}\Sigma_{\mathbf{k},i\omega_n} &= \Sigma^{\mathrm{imp}}_{i\omega_n} - \sum_{\eta,\mathbf{q},i\nu_n} m^{\eta} \widetilde{G}_{\mathbf{k}+\mathbf{q},i\omega_n+i\nu_n} \widetilde{W}^{\eta}_{\mathbf{q},i\nu_n} \Lambda^{\mathrm{imp},\eta}_{i\omega_n,i\nu_n}, \\ P^{\eta}_{\mathbf{q},i\nu_n} &= P^{\mathrm{imp},\eta}_{i\nu_n} + 2\sum_{\mathbf{k},i\omega_n} \widetilde{G}_{\mathbf{k}+\mathbf{q},i\omega_n+i\nu_n} \widetilde{G}_{\mathbf{k},i\omega_n} \Lambda^{\mathrm{imp},\eta}_{i\omega_n,i\nu_n},\end{aligned} \tag{3.2}$$

where the index $\eta = \{\mathrm{c}, \mathrm{s}\}$ corresponds to charge and spin channel respectively, and $\omega_n = (2n+1)\pi/\beta$ and $\nu_n = 2n\pi/\beta$ are fermionic and bosonic Matsubara frequencies. $G_{\mathbf{k},i\omega_n}$ is the dressed Green's function, and $W^{\mathrm{c,s}}_{\mathbf{q},i\nu_n}$ are the fully screened interactions in the charge and spin channel respectively. The local part of self-energy and polarization are replaced by their impurity counterparts $\Sigma^{\mathrm{imp}}_{i\omega_n}$ and $P^{\mathrm{imp},\eta}_{i\nu_n}$ respectively, and for any quantity X, $\widetilde{X}_{\mathbf{k},i\omega_n} = X_{\mathbf{k},i\omega_n} - X^{\mathrm{loc}}_{i\omega_n}$ with $X^{\mathrm{loc}}_{i\omega_n} = \frac{1}{N_k}\sum_{\mathbf{k}\in\mathbf{B.Z.}} X_{\mathbf{k},i\omega_n}$. We employ the Heisenberg decomposition of the interaction [22], for which we have $m_{\mathrm{c}} = 1$, $m_{\mathrm{s}} = 3$ and $W^{\eta}_{\mathbf{q},i\nu_n} = U^{\eta}_{\mathbf{q}}\left[1 - U^{\eta}_{\mathbf{q}} P^{\eta}_{\mathbf{q},i\nu_n}\right]^{-1}$. Bare interactions in charge and spin channel are, hence, given by $U^{\mathrm{c}}_{\mathbf{q}} = \frac{U_0}{2} + v_{\mathbf{q}}$ and $U^{\mathrm{s}} = -\frac{U_0}{6}$. This spin/charge ratio is a choice (dubbed "Fierz ambiguity" [22, 24]). The impurity problem was solved using the segment picture in the hybridization-expansion continuous time quantum Monte-Carlo algorithm [52, 53, 54, 55, 56] implemented with the TRIQS library [57].

In order to probe superconductivity instabilities, we solve the linearized gap equation with converged TRILEX results as an input [23]. For singlet $d-$wave pairing the corresponding eigenvalue equation for the gap reads

$$\lambda\Delta_{\mathbf{k},i\omega_n} = -\sum_{\mathbf{k}',i\omega'_n} |G_{\mathbf{k}',i\omega'_n}|^2 \Delta_{\mathbf{k}',i\omega'_n} V^{\mathrm{eff}}_{\mathbf{k}-\mathbf{k}',i\omega_n-i\omega'_n}, \tag{3.3}$$

where the singlet pairing interaction is given by

$$V^{\mathrm{eff}}_{\mathbf{q},i\nu_n} = m^{\mathrm{c}} W^{\mathrm{c}}_{\mathbf{q},i\nu_n} - m^{\mathrm{s}} W^{\mathrm{s}}_{\mathbf{q},i\nu_n}, \tag{3.4}$$

and is therefore a combination of effective interaction in *charge and spin* channel. The SC instability occurs when the largest eigenvalue $\lambda = 1$. The pairing symmetry is monitored by the $\mathbf{k}$ dependence of the gap function $\Delta_{\mathbf{k},i\omega_n}$.

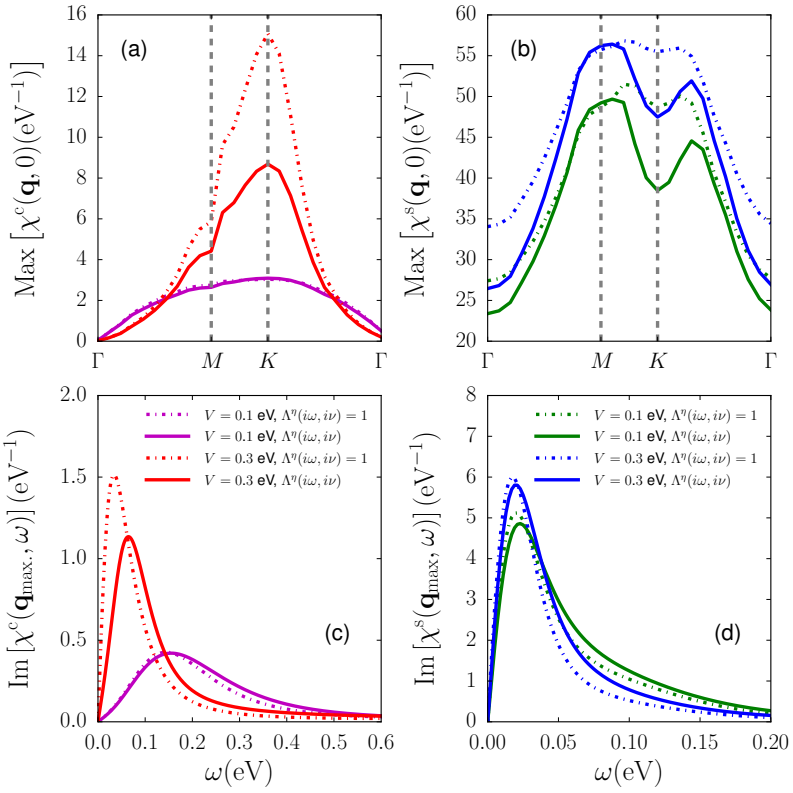

Figure 3.4: Charge- and spin response functions with (solid lines) and without (dashed lines) vertex corrections for $V = 0.1$eV and $V = 0.3$eV. Upper panels: Static charge- (a) and spin (b) response function along the high symmetry points. Lower panels: Spectrum of charge- (c) and spin (d) response function at $\mathbf{q} = \mathbf{q}_{\mathrm{max.}}$ with $\mathbf{q}_{\mathrm{max.}}$ being the peak position of the corresponding static response function. The shown results were obtained for $U_0 = 0.7$eV, $T = 116$K and $\delta = 0.2$.

3.2 Effects Vertex correction

In this section, we want to show the impact of vertex corrections to the charge- and spin-fluctuations. As depicted in Fig. 3.4, upon increasing the long-range interaction strength from $V = 0.1$eV to $V = 0.3$eV, the static charge- and spin response functions are enhanced (see Fig. 3.4 (a) and (b)). Simultaneously, their characteristic frequencies are shifted to lower energies as shown in Fig. 3.4 (c) and (d). In Fig. 3.4(a) we see that $\Lambda^{\mathrm{imp,c}}(i\omega_n, i\nu_n)$ partially suppresses the charge response function. This result agrees with findings in [58], i.e., the critical nearest-neighbor interaction strength V_{c} of metal to charge-ordered phase transition is shifted to larger values if the three-

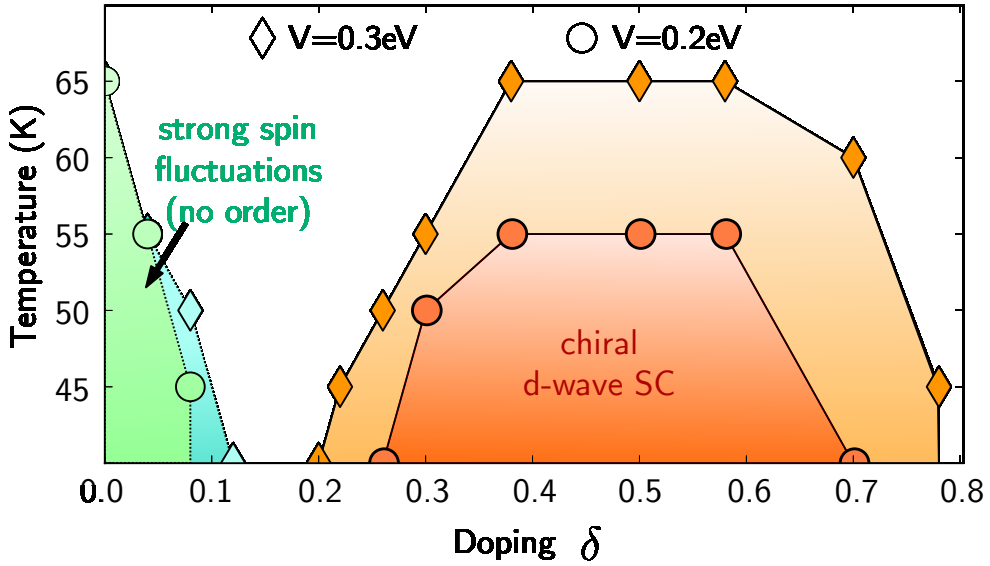

Figure 3.5: Phase diagram of the Hamiltonian (3.1) as function of temperature (for $T > 40$K) and doping for $U_0 = 0.7$eV, $V = 0.2$eV (circles) and $V = 0.3$eV (diamonds). Green/blue regions correspond to $1 \geqslant \mathrm{Max}[-\mathrm{P^s}(\mathbf{q}, \mathrm{i}\nu_\mathrm{n} = 0)\mathrm{U^s}] \geqslant 0.95$ for $\mathbf{q} \in \mathbf{B.Z.}$. Orange/red regions indicate chiral $d-$wave superconductivity.

legged vertex is taken into account. For the spin response function (Fig. 3.4(b)), $\Lambda^{\mathrm{imp,s}}(i\omega_n, i\nu_n)$ slightly suppresses its value and shifts its maximum closer to M. Finally, the λ values obtained from the solution of the gap equation for $V = 0.3$eV are actually *increased* from 0.49 to 0.52 as a consequence of the vertex corrections (for $V = 0.1$eV λ increases from 0.271 to 0.274). This means that inclusion of vertex corrections leads to even higher values of $\mathrm{T_c}$ which was found also in another recent TRILEX study for the 2D square lattice Hubbard model [23].

Based on the above observations, we can conclude that the vertex corrections will not change the qualitative behaviors of the results for superconductivity critical temperature. Hence, in the following, we will further approximate the TRILEX self-consistency equations (3.2) by choosing $\Lambda^{\mathrm{imp},\eta}_{i\omega_n, i\nu_n} = 1$.

3.3 Hole-doped phase diagram

In Fig. 3.5 we plot the temperature–doping (T–δ) phase diagram for $V = 0.2$eV and $V = 0.3$eV for a fixed value of $U_0 = 0.7$eV in the simplified TRILEX approximation.

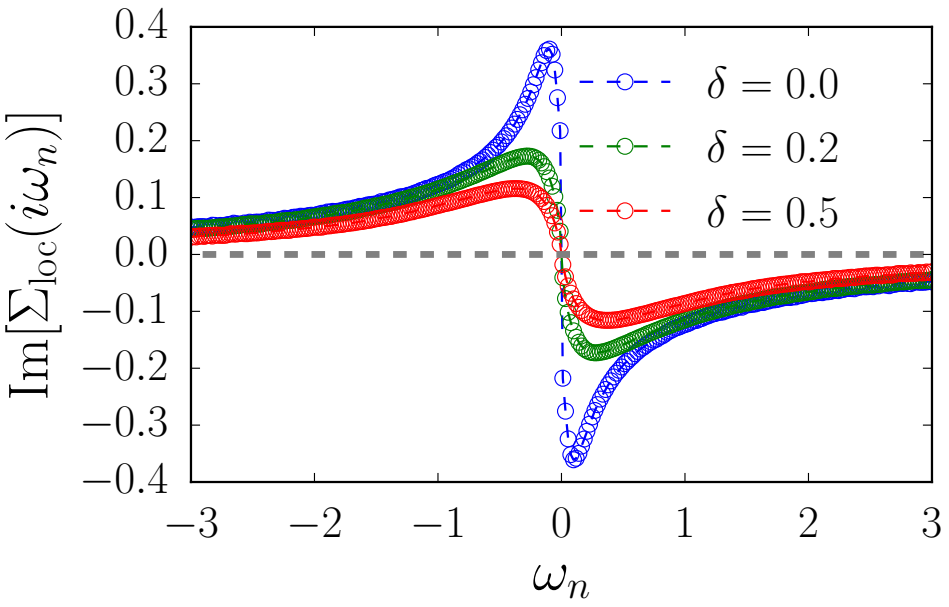

Figure 3.6: Plot of the imaginary part of the local fermionic self-energy on the Matsubara axis $\mathrm{Im}\left[\Sigma_{\mathrm{loc}}(\mathrm{i}\omega_{\mathrm{n}})\right]$ for several hole doping levels. We show data for fixed $(U_0, V) = (0.7, 0.3)$eV, and $T = 40$K.

At half-filling ($\delta = 0$) we obtain a correlated Fermi liquid with strong magnetic fluctuations. The Fermi liquid character can be seen from the imaginary part of the local fermionic self-energy on the Matsubara axis as plotted In Fig. 3.6 (data from various hole doping levels are also plotted). From the data shown we can estimate the mass enhancement of the correlated quasiparticles $m/m^* = \left[1 - \mathrm{Im}\left[\Sigma_{\mathrm{loc}}(\mathrm{i}\omega_0)\right]/\omega_0\right]^{-1} = 0.047, 0.21, 0.38$ corresponding to $\delta = 0.0, 0.2, 0.5$ respectively.

The static spin-spin correlation function $\chi^{\mathrm{s}}(\mathbf{q}, i\nu_n = 0)$ is very large at some $\mathbf{q}$ points but has not diverged yet, i.e. no phase transition has occurred. More precisely, we use $\mathrm{Max}[-\mathrm{P}^{\mathrm{s}}(\mathbf{q}, \mathrm{i}\nu_{\mathrm{n}} = 0)\mathrm{U}^{\mathrm{s}}]$ with $\mathbf{q} \in$ B.Z. which reaches 1 at a second order spin ordering phase transition to quantify the strength of the spin fluctuations and color code regions in the phase diagram for which $1 > \mathrm{Max}[-\mathrm{P}^{\mathrm{s}}(\mathbf{q}, \mathrm{i}\nu_{\mathrm{n}} = 0)\mathrm{U}^{\mathrm{s}}] \geqslant 0.95$ in green ($V = 0.2$eV) and blue ($V = 0.3$eV). From this plot we see that spin fluctuations are slightly enhanced by increasing V. For $\delta > 0.2$ we observe the emergence of a dome-shaped superconducting phase. A plot of the λ parameter in Eq. (3.3) as a function of temperature is shown in Fig. 3.7. The SC instability is indicated by $\lambda = 1$

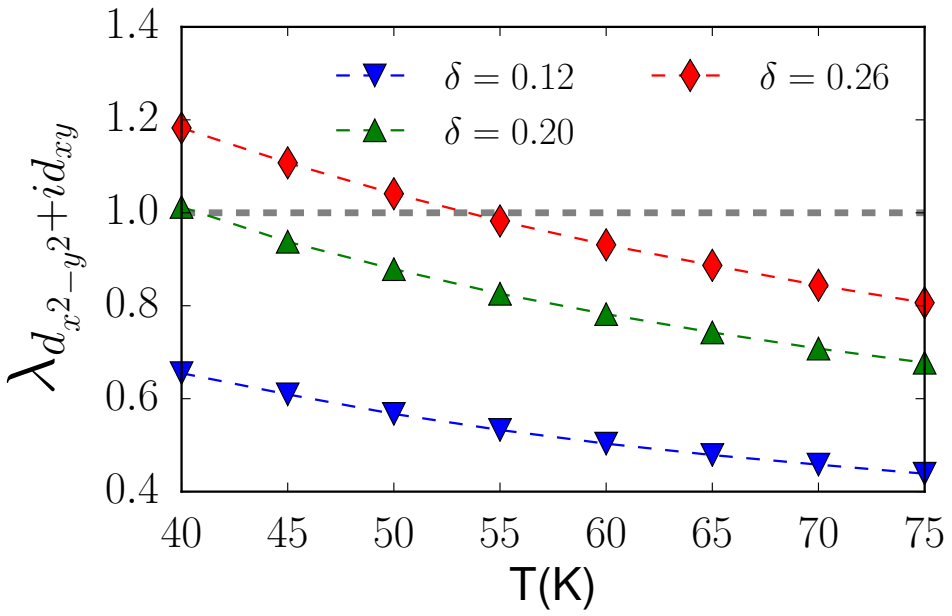

Figure 3.7: Plot of λ as a function of temperature T at different doping levels for fixed $U_0 = 0.7$eV and $V = 0.3$eV.

(for instance $\delta = 0.2$ at $T \approx 40$K and $\delta = 0.26$ at $T \approx 55$K). Please note that no extrapolation of $\lambda(T)$ is needed due to the absence of a magnetically ordered phase, different from the square lattice case [23].

The pairing symmetry of the SC phase is of d-wave character and includes doubly degenerate $d_{x^2-y^2}$- and d_{xy}-wave pairing channels. In Fig. 3.8 we plot the momentum dependence of the chiral $d-$wave gap function $\Delta_{d+id'}$ obtained from the solution of the gap equation (3.3) for the triangular lattice with long-range interaction. The chiral $d + id'$ superconducting state is a time-reversal symmetry breaking state with non-trivial topology as can be seen in Fig. 3.8(d) from the non-zero winding number($= 2$) along the Fermi surface. This indicates the existence of two edge states [59].

The degeneracy of these two pairing symmetries is protected by the C_{6v} point group of the triangular lattice, which then yields chiral $d-$wave symmetry below T_c to maximize condensation energy. The predicted chiral SC phase depends crucially on V: T_c increases from $V = 0.2$eV (red circles) to $V = 0.3$eV (orange diamonds) as shown in Fig. 3.5. Moreover, for $V = 0.0$eV and $V = 0.1$eV (not shown here) we do not find a SC phase for $T > 40$K.

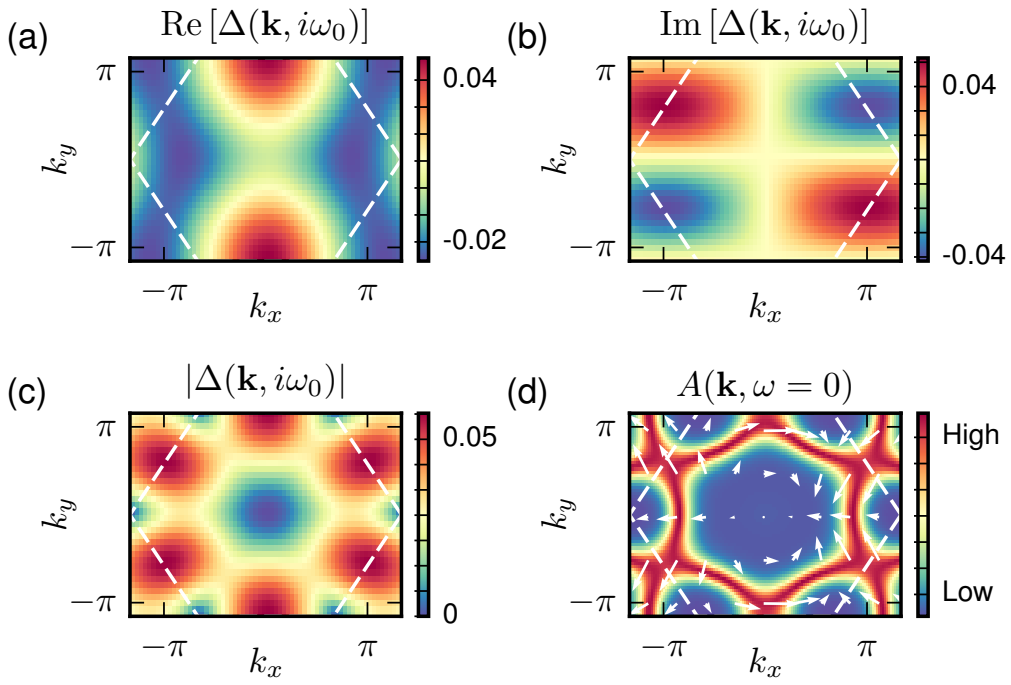

Figure 3.8: Momentum dependence of the gap function $\Delta_{d+id'}(\mathbf{k}, i\omega_n)$ at $\omega_0 = i\pi T$. (a) $\mathrm{Re}\,[\Delta_{d+id'}]$, (b) $\mathrm{Im}\,[\Delta_{d+id'}]$ and (c) $\|\Delta_{d+id'}\|$. (d) Plot of the complex gap function as vectors $(\mathrm{Re}\,[\Delta_{\mathrm{d+id'}}], \mathrm{Im}\,[\Delta_{\mathrm{d+id'}}])$ on top of the momentum dependent spectral function $A(\mathbf{k}, \omega = 0) = -G(\mathbf{k}, \tau = \beta/2)/\pi$. The gap function and spectral function were calculated for $T = 40$K, $\delta = 0.2$ and $(U_0, V) = (0.7, 0.3)$eV.

3.4 Impact of the long-range interaction

The impact of V on the SC instability is reflected in the effective singlet-pairing interaction $V^{\mathrm{eff}}_{\mathbf{q},i\nu_n}$ which depends on fluctuations in *both* charge and spin channels. We analyze the respective susceptibilities $\chi^{\mathrm{c/s}}(\mathbf{q}, i\nu_n)$ with the data shown in Fig. 3.9: In the upper panels we show the maximum values of the static ($i\nu_n = 0$) charge (left hand side) and spin (right hand side) susceptibilities as a function of hole doping. The corresponding position of the maximum in the first Brillouin zone is color coded (see inset).

The charge fluctuations increase with hole doping to a maximum value around $\delta = 0.5$ and, thereafter, decrease approaching the "empty" limit at $\delta = 1$. The spin fluctuations, instead, decrease monotonically as a function of δ. While $\chi^{\mathrm{c}}(\mathbf{q}, i\nu_n = 0)$

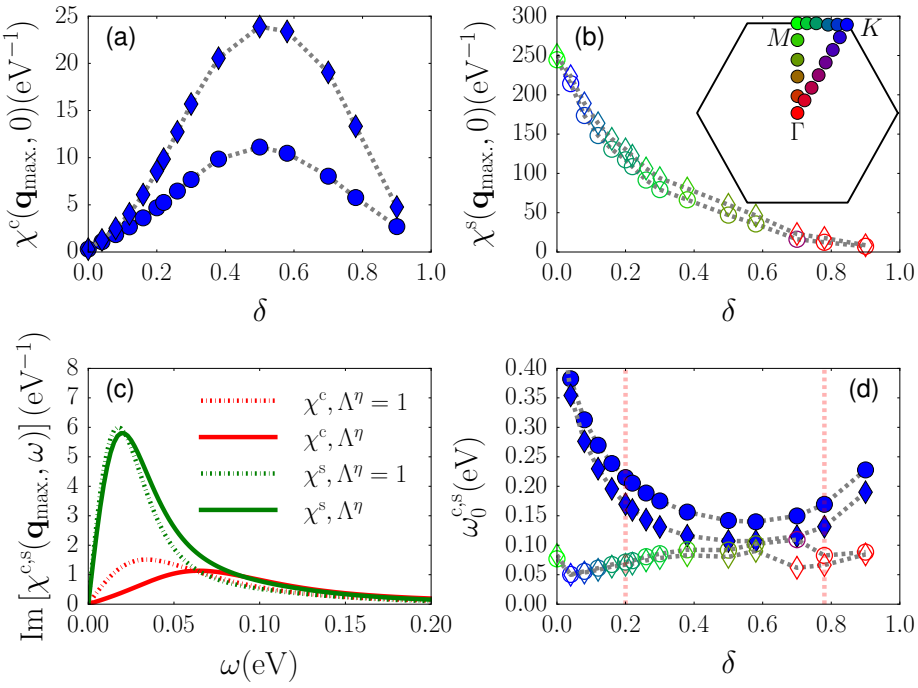

Figure 3.9: Maximum values of the static charge (a) and spin (b) response functions versus hole doping. Color coding indicates the position of the maximum in the first Brillouin zone as defined in the inset. Data is shown for fixed $U_0 = 0.7$eV and $T = 40$K and non-local interaction strength $V = 0.3$eV (diamonds) and $V = 0.2$eV (circles); (c) Charge- and spin response functions on the real frequency axis (obtained by analytical continuation with the maximum entropy method[60]) at their maximum in momentum space ($\mathbf{q}_{\max.}$) with (dashed) and without (solid) vertex corrections for $T = 116$K and $\delta = 0.2$; (d) Characteristic frequency of charge- (filled symbols) and spin (open symbols) fluctuations with the same convention and parameters as (a) and (b).

always peaks at K, the maximum of $\chi^{\mathrm{s}}(\mathbf{q}, i\nu_n = 0)$ moves from M to K when the system is slightly doped, and then follows $K \to M \to \Gamma$ when the system is further hole-doped. The peak position of the charge response function as a function of doping remains at the K point since its momentum dependence is mainly determined by the doping independent $v(\mathbf{q})$ which energetically favors a 3×3 charge configuration in real space [41]. The momentum dependence of the spin response function, however, is mostly determined by the topology of the Fermi surface. Indeed, the V dependence is much stronger for the charge response (compare diamond ($V = 0.3$eV) and circle ($V = 0.2$eV) symbols in Fig. 3.9). There are, however, small effects of V to the spin response function which can be understood by the V-dependent renormalization of

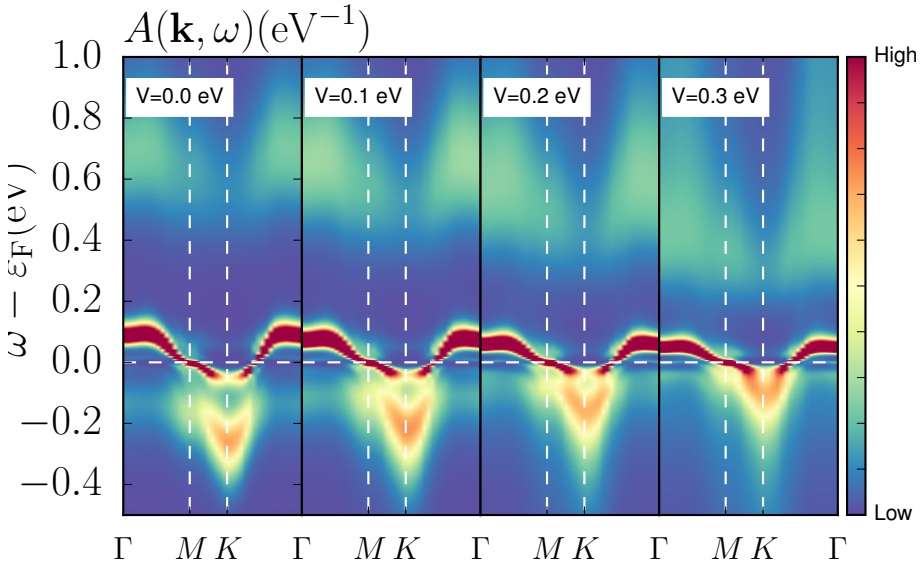

Figure 3.10: Single particle spectral function $A(\mathbf{k},\omega)$ along the high symmetry path Γ-M-K-Γ (see inset of Fig. 3.9) obtained at $\delta = 0.2$, $T = 40$K, $U_0 = 0.7$eV and four values of V.

the one-particle spectra as show in Fig. 3.10 [61]. At fixed $T = 40$K and $\delta = 0.2$, V is increased from 0.0eV to 0.3eV (subplots from left to right hand side). Upon increasing V, the bandwidth is effectively reduced and the spectral weight near to the Fermi energy is increased. Consequently, particle-hole excitations that contribute to the spin polarization $P^{\mathrm{s}}(\mathbf{q}, i\nu_n)$ and the spin susceptibility are enhanced.

We now extend these considerations to the frequency dependence of the bosonic fluctuations. In Fig. 3.9(c) we plot the dynamic response functions at the $\mathbf{q}$-points where they are maximal ($\mathbf{q}_{\mathrm{max.}}$) for doping $\delta = 0.2$. The data clearly shows a peaked structure of the dynamic response functions. Moreover, we show in this plot the impact of the vertex corrections (compare solid and dashed lines) which are only quantitative in the considered case as claimed in section 3.2. Fig. 3.9(d) shows the doping dependence of the characteristic frequency $\omega_0^{\mathrm{c,s}}(\mathbf{q}_{\mathrm{max.}})$ defined by

$$\omega_0^{\mathrm{c,s}}(\mathbf{q}_{\mathrm{max.}}) = \int_0^\infty \omega \mathrm{Im}\left[\chi^{\mathrm{c,s}}(\mathbf{q}_{\mathrm{max.}},\omega)\right] d\omega \Big/ \int_0^\infty \mathrm{Im}\left[\chi^{\mathrm{c,s}}(\mathbf{q}_{\mathrm{max.}},\omega)\right] d\omega \tag{3.5}$$

in both channels. Inside the superconducting region (indicated by the vertical red

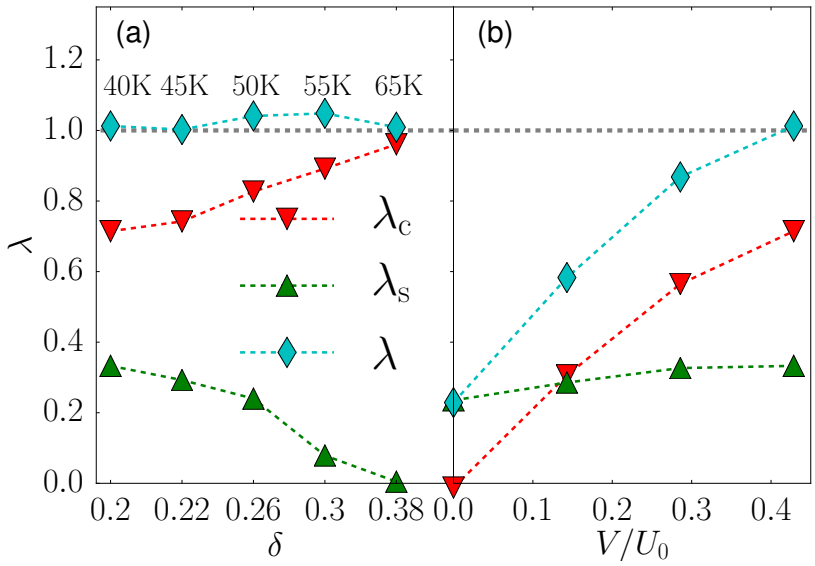

Figure 3.11: Eigenvalue λ of the gap equation Eq. (3.3) ($\lambda = 1$ signals SC transition) from full effective singlet pairing interaction $V^{\text{eff}}_{\mathbf{q},i\nu_n}$ (cyan) and charge/spin only channels (red /green). (a) Plot for $V = 0.3$eV along the SC phase boundary up to doping $\delta = 0.38$. (b) Plot as a function of V for fixed doping $\delta = 0.2$ and temperature $T = 40$K.

dashed lines) the characteristic frequency of the fluctuations are of the order of $100 - 200$meV. Moreover, $|\omega_0^{\text{c}}\text{-}\omega_0^{\text{s}}|$ is small and minimal for the region of maximum T_c. In agreement with our discussion above we see that an increase of V yields even smaller $|\omega_0^{\text{c}}\text{-}\omega_0^{\text{s}}|$ which suggests that charge and spin contributions to the SC pairing mechanism are cumulative.

3.5 Separating spin and charge channels in the pairing mechanism

In order to disentangle the interplay between charge and spin degrees of freedom in gap equation (3.3), we solve for λ including contributions from only spin- (λ_s) and only charge channel (λ_c), i.e., $V^{\text{eff}}_{\mathbf{q},i\nu_n} = -3W^{\text{s}}_{\mathbf{q},i\nu_n}$ and $V^{\text{eff}}_{\mathbf{q},i\nu_n} = W^{\text{c}}_{\mathbf{q},i\nu_n}$ respectively. First, we follow the phase boundary of the SC phase in the underdoped regime for fixed $V = 0.3$eV starting from $(\delta, T) = (0.2, 40\text{K})$ up to $(\delta, T) = (0.38, 65\text{K})$. In

Fig. 3.11(a) we plot λ, λ_s, and λ_c: Since we are following the phase transition line, $\lambda \approx 1$. λ_c and λ_s are both smaller than λ and $\lambda_c + \lambda_s \approx \lambda$ indicating a cumulative charge and spin contribution for the chiral d-wave pairing in the underdoped regime. The same conclusion can be drawn when the λ values are calculated at the critical doping $\delta_c = 0.2$ as a function of the non-local interaction V as depicted in Fig. 3.11(b).

Our data indicates that overall both spin- and charge fluctuations are important for the SC phase. As a function of doping, however, we observe that charge fluctuations become increasingly dominant and λ_s becomes negligible. This effect is reflected in the V dependence of the SC dome in Fig.3.5 which is stronger at larger dopings. We arrive at the same conclusions when we analyze the dependence of λ on the choice of the Fierz parameter that defines the charge-to-spin fluctuation ratio which will be presented below.

3.6 Dependence on the charge to spin ratio

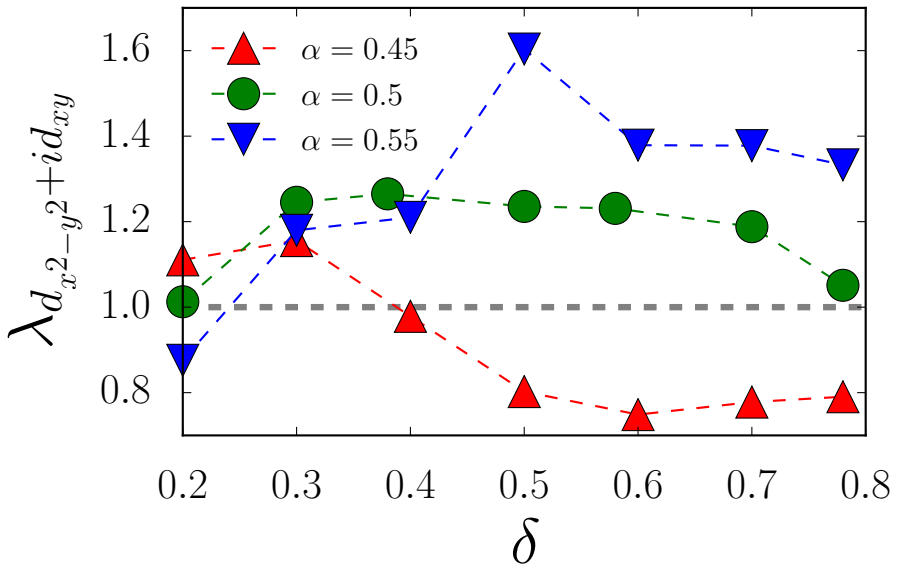

Figure 3.12: Chiral $d-$wave λ values corresponding to different values of the Fierz parameter α as a function of doping. The shown data was obtained at $T = 40$K, $U_0 = 0.7$eV, and $V = 0.3$eV.

As mentioned in Chapter 2.3, the ratio of the bare interaction in charge- and spin

channels may be parametrized by α, i.e.,

$$U^{\mathrm{c}}(\mathbf{q}) = (3\alpha - 1)U_0 + v(\mathbf{q}), U^{\mathrm{s}} = (\alpha - 2/3)U_0 \tag{3.6}$$

for Heisenberg decoupling [21]. The TRILEX results depend a priori on the choice of the Fierz parameter α. In the following, we show that our conclusions are robust with respect to the choice of α. While there is a sizable dependence of the λ values on α, this dependency leads only to a quantitative shift of the boundary of the SC phase but SC is never suppressed.

Since α controls the contributions from charge- and spin fluctuations to the SC pairing glue, we can exploit the dependence of the results on α as an indicator of their respective role in the emergence of SC. As shown in Fig. 3.12, for comparatively small doping ($\delta \sim 0.2$) λ is increased by decreasing α (i.e. emphasizing spin fluctuations). This indicates that at small doping spin fluctuations are the main contributor to the emergence of superconductivity. At large doping ($\delta \geq 0.5$), in contrast, λ is increased by increasing α (emphasizing the charge channel), which indicates once more that charge fluctuations are key for the emergence of superconductivity at large doping. Finally, for intermediate doping ($\delta \in (0.3, 0.42)$), the largest λ value is found for $\alpha = 0.5$, indicating that in this region charge- and spin fluctuations contribute "cumulatively" to the SC instability. While it is hard to further disentangle the cross influence of charge and spin fluctuations in the self-consistent solution, the insights from the α dependence support the picture of a cooperative (or additive) spin-charge pairing mechanism.

3.7 Long-range versus short-range non-local interaction

In this section, we move to show that it is not possible to obtain the same phase diagram (in particular the superconducting phase) with non-local but short-range (e.g. nearest-neighbor) interaction. In Fig. 3.13(a) we show λ as a function of V for the short-range (diamonds) and long-range (circles) interaction. Please note that V denotes the strength of the $1/r$ tail when long-range interactions are considered while it represents nearest-neighbor interactions only for the short-range version. We

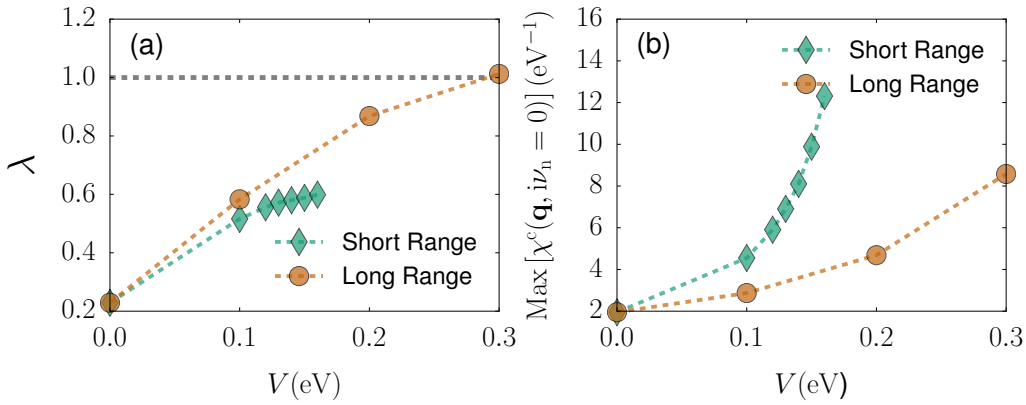

Figure 3.13: Comparison of short- and long-range interaction. Here V represents the nearest-neighbor interaction strength for short-range interaction and the $1/r$ prefactor for long-range interaction. (a) λ values as a function of V for short- (diamond) and long-range interaction (circle). (b) Maximum of static charge susceptibility as a function of V. The parameters are $U_0 = 0.7$eV, $T = 40$K and $\delta = 0.2$.

not only observe a downturn of λ upon increasing V but, most importantly, a dramatic increase in the associated charge response functions indicating a second order phase transition to a charge ordered phase (Fig. 3.13(b)). Hence, when only nearest-neighbor interaction is considered, a charge order instability will occur long before superconducting fluctuations become sizable. In the case of true long-range interactions, the situation is quite different and charge (and spin) fluctuations are enhanced but remain finite up to the point of $\lambda = 1$.

3.8 Comparison to the square lattice

As discussed above, the charge/spin pairing mechanism of our chiral SC instability depends crucially on the degeneracy of the $d_{x^2-y^2}-$ and d_{xy} pairing state. This is the case for the triangular lattice where both states belong to the same irreducible representation (E_2). For different lattice geometries where $d_{x^2-y^2}-$ and d_{xy} pairing states are not degenerate the interplay between charge- and spin fluctuation for the SC instability can be qualitatively different from our model. As an important example we mention the 2D square lattice for which $d_{x^2-y^2}-$ and d_{xy} belong to different irreducible representations B_1 and B_2, respectively. In Fig. 3.14(a) and (d) we show the corresponding λ values obtained in the square lattice as a function of the long-

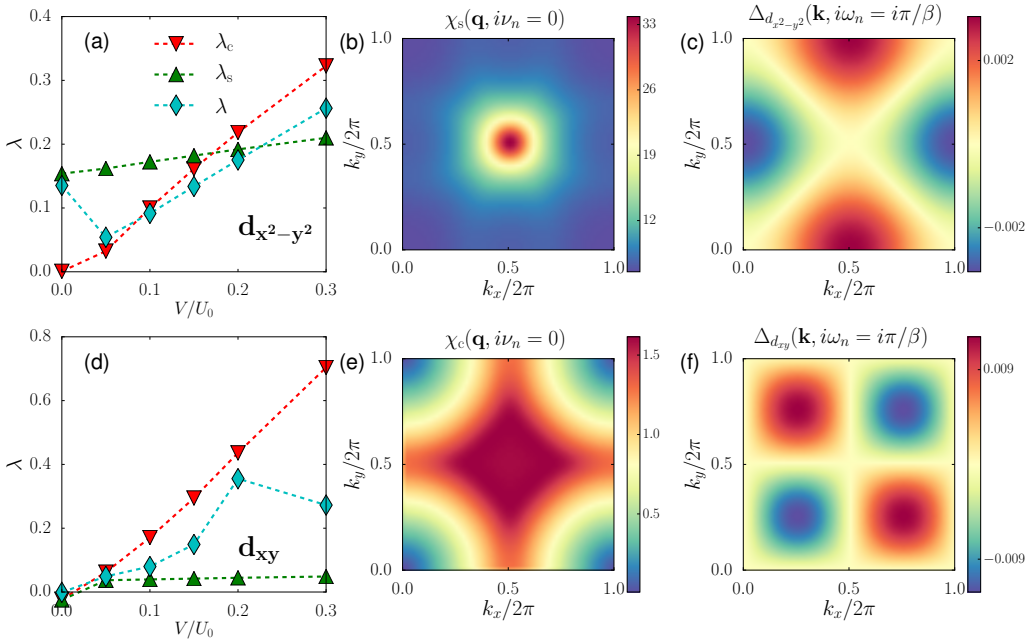

Figure 3.14: Simplified TRILEX results for the square lattice with long-range interaction. The parameters are chosen as $t = -0.25$eV and $t' = -0.2t$ corresponding to nearest-neighbor and next-nearest-neighbor hopping integrals, on-site interaction $U_0 = 2.0$eV and fixed temperature $T = 290$K. Upper panel: (a) λ values for $d_{x^2-y^2}$ pairing symmetry as a function of long-range interaction strength V computed with charge (down triangular), spin (up triangular) and combined (diamond) contributions; (b) static spin response function; (c) solved $d_{x^2-y^2}$ gap function at $i\omega_n = i\pi/\beta$. Here hole doping level is $\delta = 0.2$, and $V = 0.0$eV for (b) and (c). Lower panel:(d) λ values for d_{xy} pairing symmetry as function of long-range interaction strength V computed with charge (down triangular), spin (up triangular) and combined (diamond) contributions; (e) static charge response function; (f) solved d_{xy} gap function. Hole doping level is fixed at $\delta = 0.5$ and $V = 0.6$eV for (e) and (f).

range interaction V for both $d_{x^2-y^2}-$ and d_{xy} pairing symmetries. With the same separation of channel contribution as performed in section 3.5, we see a qualitative difference in the behavior of λ: on the triangular lattice, λ is larger than λ_c and λ_s, while on square lattice λ is in between or smaller than λ_c and λ_s.

In order to disentangle the singlet-pairing interaction in the particle-particle chan-

nel into charge- and spin contributions we use

$$V^{\text{eff}}(\mathbf{q}, i\nu_n) = W^{\text{c}}(\mathbf{q}, i\nu_n) - 3W^{\text{s}}(\mathbf{q}, i\nu_n) = \frac{U^{\text{c}}(\mathbf{q})}{1 - U^{\text{c}}(\mathbf{q})P^{\text{c}}(\mathbf{q}, i\nu_n)} - 3\frac{U^{\text{s}}}{1 - U^{\text{s}}P^{\text{s}}(\mathbf{q}, i\nu_n)} \tag{3.7}$$

$$= U(\mathbf{q}) + \underbrace{\frac{U^{\text{c}}(\mathbf{q})P^{\text{c}}(\mathbf{q}, i\nu_n)U^{\text{c}}(\mathbf{q})}{1 - U^{\text{c}}(\mathbf{q})P^{\text{c}}(\mathbf{q}, i\nu_n)}}_{\textbf{charge},-} \underbrace{-3\frac{U^{\text{s}}P^{\text{s}}(\mathbf{q}, i\nu_n)U^{\text{s}}}{1 - U^{\text{s}}P^{\text{s}}(\mathbf{q}, i\nu_n)}}_{\textbf{spin},+},$$

with $U^{\text{c}}(\mathbf{q}) = \frac{U_0}{2} + v(\mathbf{q})$. The $+(-)$ denotes the positive/negative contribution from each channel ($P^{\text{c/s}} < 0$ in our parameter range). We denote the typical pairing-scattering momentum for charge- and spin channel as Q_{c} (Fig. 3.14(e)) and Q_{s} (Fig. 3.14(b)) respectively (i.e. momenta where $\chi_{\text{c/s}}$ are maximal). In order to find a large λ value when solving Eq. (3.3) $\Delta(\mathbf{k}, i\omega_n)$ should not change sign for scattering with Q_{c} in the charge channel, while it should change sign when scattering with Q_{s}. Hence, when spin fluctuations dominate, the $d_{x^2-y^2}$(Fig. 3.14(c)) pairing symmetry is favorable in the $d-$wave singlet pairing and charge fluctuations contribute destructively. Vice versa, when charge fluctuations dominate, d_{xy}(Fig. 3.14(f)) symmetry will be the favored.

3.9 Conclusion

In conclusion we predict the existence of a dome shaped unconventional chiral d-wave superconducting phase for hole-doped triangular lattice systems with $\propto 1/r$ interactions which could be realized by hole-doping existing α phase Si(111) adatom materials. The analysis of spin and charge correlation functions reveals that lattice geometry as well as the non-local interaction are necessary conditions for the emergence of superconductivity. The nature of the pairing undergoes a crossover from a combined charge/spin mechanism in the underdoped regime towards a charge fluctuation dominated one at higher doping. We have emphasized two aspects about the induced SC: i) The true long-range character is crucial in our range of parameters. If only short-range (i.e. nearest-neighbor) interactions are considered charge ordering is overestimated and long before any SC emerges the system turns into a charge ordered insulator as proven by calculations shown in 3.7. ii) The degeneracy of $d_{x^2-y^2}-$ and $d_{xy}-$wave pairing state is important for the cumulative charge and spin interplay.

Since the origin of this degeneracy is connected to the lattice symmetry group, a different behavior can be expected for the 2D square lattice as showed in 3.8: in the square geometry with relatively large V/U_0, the $\mathbf{q}$ dependence of $\chi^{\mathrm{c}}(\mathbf{q}, i\nu_n = 0)$ favors $d_{xy}-$pairing symmetry while $\chi^{\mathrm{s}}(\mathbf{q}, i\nu_n = 0)$ prefers $d_{x^2-y^2}-$pairing symmetry, and the two channels compete with each other.

4

Matrix Product States

The continuous development of DMFT and its various extensions, has provided us with deep understanding on strongly correlated systems far beyond the scope of traditional mean-filed theory. In the previous parts of this thesis, we have applied its TRILEX extension to unveil the novel physics induced by long-range interactions in the adatom systems. We have shown the importance of **momentum resolved** spin- and charge fluctuations in the emergence of unconventional superconductivity. However, we should also point out that the spin- and charge fluctuations considered in the single-site implementation of TRILEX has a Fermi surface nesting nature, i.e., their strength and momentum dependence are mainly determined by the particle-hole processes of the quasi-particles around the Fermi surface, while the short-range spin singlet and charge bond fluctuations are not included properly. To circumvent this shortcoming, we need to enlarge our impurity size either in real- or reciprocal space, similar to the strategies that are applied in the cluster extensions of DMFT. Hence, at the core of DMFT and its various extensions, is the efficient and accurate solution of the auxiliary impurity model.

Furthermore, the class of various quantum impurity problems itself is also of long-standing interest to physicists. They describe a wide range of quantum mechanical problems that involve an interacting subsystem with a limited number of degrees of freedom (an impurity) coupled to a much larger non-interacting system (a bath) that contains a quasi-continuum of degrees of freedom. Examples include the Kondo and

heavy-fermion systems [62, 63], tunneling in dissipative systems [64], various problems in quantum optics [65], and the core-level X-ray spectrscopy [66, 67].

Over the past decades, many numerical methods have been developed to solve the impurity problems. Among which, the most prominent examples are the exact diagonalization (ED) [68, 69, 70, 71, 72, 73, 74], numerical renormalization group (NRG) [11, 75, 76, 77, 78, 79], continuous-time quantum Monte Carlo (CT-QMC) [80, 81, 82, 83, 84, 85], density-matrix renormalization group (DMRG) or matrix product states [86, 87, 88, 89, 90, 91, 92, 93, 94, 95, 96, 97, 98]. Each method has its own merits and shortcomings:

- ED represents the most straightforward approach to the solution of impurity problems. It approximates the continuum hybridization function by few energy levels (usually $5-12$) represented by bath sites in the discretized Hamiltonian. Then the Hamiltonian is solved, either by a full diagonalization or a Lanczos approach. Because of the exponential increase of the Hilbert space as the number of bath sites, the limitation of ED is the small number of bath sites it can handle. For such a small number of bath sites, it is impossible to achieve a reasonable resolution of the spectral function on real-axis, hence, most of the ED based solvers are performed on the imaginary-axis.

- NRG circumvents the exponential growth of Hilbert space encountered in ED by, instead of diagonalizing the full Hamiltonian directly, first diagonalizing a small subsystem and including effects of the rest of the bath sites in a renormalization group manner: each time a site in the rest of the bath sites is absorbed into the effective system, the Hamiltonian of the combined system is diagonalized, while only a fixed number of low lying energy states are kept to construct the new effective system. It can be performed on real-axis and also a large number of bath sites can be handled in single- and two- band calculations. It can have extremely good energy resolution for low-energy spectra, however, due to the necessarily logarithmic bath discretization [78] to guarantee the convergence of this algorithm, the resolution for high-energy features lacks satisfactory. Furthermore, its application to multi-band problems is also very challenging, because the computational costs increase exponentially as the number of bands.

- QMC in its discrete and continuous time variants represent another category

of methods, in which instead of diagonalizing the many-body Hamiltonian, correlation functions and observables are obtained by efficient sampling of the configuration space. It can solve multi-band problems efficiently, and even be maintainable to include retarded interactions. However, since it is formulated on the imaginary axes, it entails an ill-conditioned inversion problem when obtaining real-frequency spectra [60]. In addition, when applied to problems with low-symmetry interactions and/or off-diagonal Green's functions, the famous fermionic sign problem, which decreases the sampling efficiency exponentially, prevents its applications at low temperatures.

- DMRG in the MPS language is another candidate for the impurity problem. This category of method is based on an efficient parameterization of the many-body wave function: the original exponential growth of variables in the wave function is reduced to a polynomial one that exhibits a matrix product form. When implemented on the real axes, its resultant achieves a good resolution of the spectral function in both high- and low energies. However, it is limited to one and two band cases due to the exponential scaling of the complexity-or bond dimension in the matrix product states language-with the number of bands. Furthermore, the linear growth of entanglement in the real time evolution poses another hard core limit to extract long time dynamics. Alternatively, imaginary time evolution is proposed to circumvent the growth of entanglement in real time evolution [94], but this approach introduces, again, the ill-conditioned analytical continuation of data to the real-axis.

With the strengths and shortcomings of each of these methods in mind, we want to further motivate to perform calculations directly on the real-axis instead of the imaginary-axis. As already indicated in the early attempts to fit the hybridization function on the imaginary-axis with a small number of bath site parameters, aside from the ill-conditioned analytical continuation process, the information contained in imaginary time quantities are not enough to resolve the fine structure in the spectral functions [99]. For instance, as presented in [94], the accuracy of fitting the hybridization function can't be improved anymore after 9 bath sites. Impurity models with such a limited number of bath sites have a poor resolution of the spectral function. As explained in [99] in detail, even if we can keep the accuracy of data on the imaginary-axis up to 10 digits, it can be presented by a relatively small number of poles (~ 10).

Thus, we lose certain details in the spectral function, if the imaginary-axis are used to perform the calculations.

However, for calculations performed on the real-axis, we usually need a large number of bath sites ($\sim$ 100 for each band) to have a reasonable resolution of the spectra. Hence, it is usually inaccessible for the methods listed above. One of the breakthrough is the alternative approach for countering the exponential growth of computation cost by searching for an optimized local basis for representing impurity problems. This has been most actively explored using ED methods [72, 74], which are otherwise severely limited in accessible number of bands and bath sites. In Ref. [74], the authors have demonstrated that a one-band impurity problem with a few hundred bath sites, ten times of that dealt with in conventional ED, can be efficiently solved on the real-axis when represented on a optimized single-particle basis set.

From the above discussion, we can conclude that, compared to other methods, the MPS based impurity solver is promising, although further improvements are still needed to circumvent the difficulties of handling multi-band systems and accessing long time dynamics. The rest of this thesis represents our attempts in these directions. In this chapter, we will introduce the basic background of MPS and the related algorithms which are needed in the implementation of our solver.

4.1 Matrix Product States

For a general many-body wave function living on a global Hilbert space $\mathcal{H} = \otimes_i \mathcal{H}_i$ which is composed by tensor product of L local Hilbert space each spanned by local basis set $\{\sigma_i\}$, it can be expressed as

$$|\psi\rangle = \sum_{\sigma_0\sigma_1\cdots\sigma_{L-1}} c_{\sigma_1\sigma_2\cdots\sigma_L} |\sigma_1\sigma_2\cdots\sigma_L\rangle, \tag{4.1}$$

where $c_{\sigma_0\sigma_1\cdots\sigma_{L-1}}$ is the rank$-L$ complex coefficients. Its dimension is equal to d^L with d being the dimension of the local Hilbert space. The main idea of MPS is that, for systems with a local and gapped Hamiltonian, the exponential growth of $c_{\sigma_0\sigma_1\cdots\sigma_{L-1}}$ against the system size L can be reduced to a polynomial one that exhibits a matrix

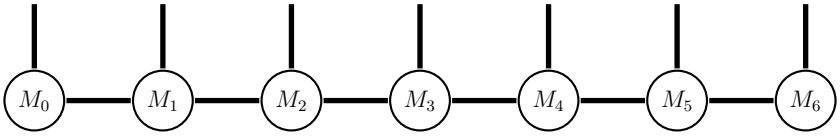

Figure 4.1: Graphic representation of the MPS. M_i represents a rank-3 site tensor with two bond legs and one physical leg.

product form [100, 101]

$$|\psi\rangle = \sum_{\sigma_0\sigma_1\cdots\sigma_{L-1}} M^{0;\sigma_0}_{b_0 b_1} M^{1;\sigma_1}_{b_1 b_2} \cdots M^{L-1;\sigma_{L-1}}_{b_{L-1} b_L} |\sigma_0\sigma_1\cdots\sigma_{L-1}\rangle, \tag{4.2}$$

where $M^{i;\sigma_i}_{b_{i-1}b_i}$ is a rank-3 tensor, and all the repeated indices are implicitly summed over. σ_i and b_i are called physical and bond leg, respectively. The first and last bond legs are dummy ones and have dimension of 1, e.g., $b_0 = b_L = 1$. The bond dimension of the MPS is defined as the largest bond dimension throughout the system $D = \max\{b_i, i \in [0, L]\}$. We can represent the MPS graphically as depicted in Fig. 4.1: on each lattice site, we have a rank-3 site tensor with a free physical leg and two bond legs each of which is connected with another nearest-neighbor site tensor. All the legs shared by two site tensors are summed over.

We can bring the site tensor into a left-normalized form by singular-value decomposition (SVD) as depicted in Fig. 4.2(a). We first group the physical and left bond legs into a combined leg, then the new formed matrix is decomposed as $M^i_{(\sigma_i b_{i-1}),b_i} \xrightarrow{\textbf{SVD}} U \cdot S \cdot V^\dagger$. The new site tensor is obtained by reforming the U matrix back into a rank-3 tensor $A^{i;\sigma_i}_{b_{i-1}b_i}$, while S and $V^\dagger$ are multiplied to the next site tensor M^{i+1}. Since the new site tensor is obtained from the SVD of M^i, we have

$$\sum_{\sigma_i} \left(A^{i;\sigma_i}\right)^\dagger A^{i;\sigma_i} = \mathbb{I}. \tag{4.3}$$

Similarly, as depicted in Fig. 4.2(b), we can also bring M^i into a right-normalized form. The resulting new site tensor B^i should satisfy

$$\sum_{\sigma_i} B^{i;\sigma_i} \left(B^{i;\sigma_i}\right)^\dagger = \mathbb{I}. \tag{4.4}$$

Graphic representation of equation (4.3) and (4.4) are depicted in Fig. 4.3.

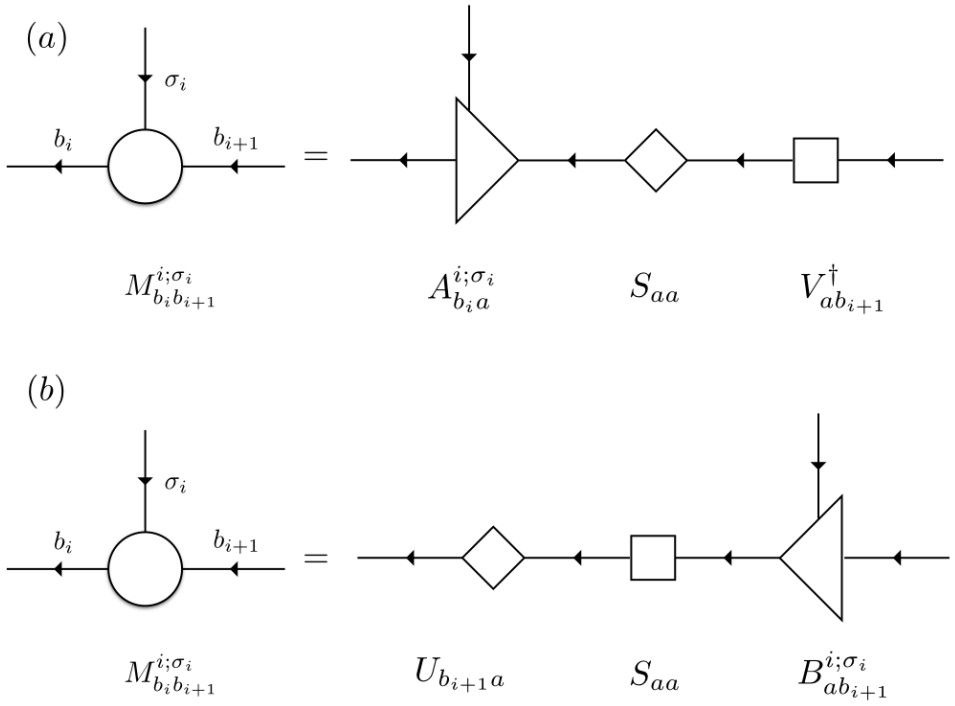

Figure 4.2: Graphic representation of taking the site tensor M^i into the (a) left-normalized and (b) right-normalized form by the SVD.

Starting from the first (last) site and bringing the site tensors into left- (right-) normalized form successively, we can achieve a complete left- (right-) normalized MPS. As will be shown in the following discussions, bringing the MPS into left- or right-normalized form can benefit the MPS related operations dramatically. We can also have an MPS in mixed form with an orthogonality center at site i meaning that the site tensors in the left of M^i are in left-normalized form, while the site tensors on the right of M^i are in right-normalized form.

4.1.1 Compression of the MPS

One should note that, MPS with a fixed bond dimension doesn't form a vector space, i.e., for two MPSs $|\psi_1\rangle$ and $|\psi_2\rangle$ with bond dimension D, their addition $|\psi\rangle = |\psi_1\rangle + |\psi_2\rangle$ will have a bond dimension different from D. To show this, assume that $|\psi_1\rangle = \sum_{\{\sigma_i\}} \mathrm{Tr}\left[\{M_1^i\}\right] |\{\sigma_i\}\rangle$ and $|\psi_2\rangle = \sum_{\{\sigma_i\}} \mathrm{Tr}\left[\{M_2^i\}\right] |\{\sigma_i\}\rangle$, then the resultant MPS

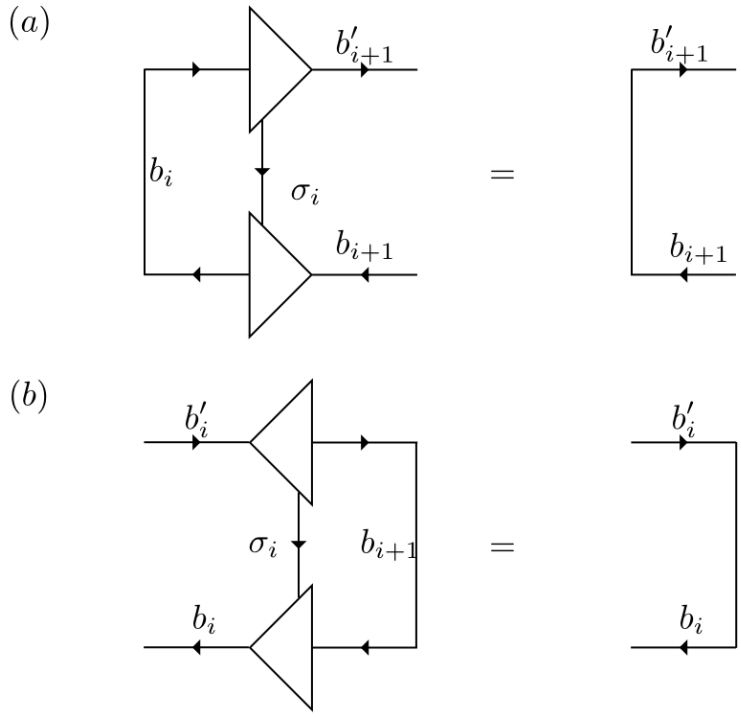

Figure 4.3: Graphic representation of the left- and right-normalization relation satisfied by (a) A^i and (b) B^i.

$|\psi\rangle = \sum_{\{\sigma_i\}} \mathrm{Tr}\left[\{M^i\}\right] |\{\sigma_i\}\rangle$ from the addition operation should satisfy

$$M^{0;\sigma_0} = \begin{pmatrix} M_1^{0;\sigma_0} & M_2^{0;\sigma_0} \end{pmatrix}, \tag{4.5}$$

for the fist site,

$$M^{i;\sigma_i} = \begin{pmatrix} M_1^{i;\sigma_i} & 0 \\ 0 & M_2^{i;\sigma_i} \end{pmatrix}, \tag{4.6}$$

for the bulk site $0 < i < L-1$ and

$$M^{L-1;\sigma_{L-1}} = \begin{pmatrix} M_1^{L-1;\sigma_{L-1}} \\ M_2^{L-1;\sigma_{L-1}} \end{pmatrix}, \tag{4.7}$$

for the last site. From Eq.(4.5), (4.6) and (4.7), it is apparent that bond dimension of the resulting MPS is increased. Another usual occasion in which the bond dimension

can be increased is the applying of many-body operators on MPS which will be elaborated in Sec.(4.3).

Although MPS reduces the exponential complexity of presenting a many-body wave function into a polynomial one, handling MPS with large bond dimension still poses challenges in practical calculations, because the computational costs usually have a polynomial dependence on the bond dimension ($\sim m^3$ for single-site ground state search). Hence, from time to time, we need to compress a MPS from a large bond dimension D' to a small one D.

To do this, consider a MPS $|\psi'\rangle$ with bond dimension D' and we want to compress it into a MPS $|\psi\rangle$ with bond dimension D ($D < D'$). The criteria for such a compression is that the Hilbert distance between these two states

$$|||\psi\rangle - |\psi'\rangle|| \tag{4.8}$$

is minimized. The most direct way to compress $|\psi'\rangle$ is to truncate each M' successively by keeping only the largest D singular values after the SVD of M'. This is done by assuming that the orthogonality center of $|\psi'\rangle$ is located at site i and performing a SVD to M'^i as

$$M'^{i;\sigma_i}_{b_i b_{i+1}} = \sum_{a=0}^{D'} U^{\sigma_i}_{b_i a} S_{aa} \left(V^\dagger\right)_{a b_{i+1}}. \tag{4.9}$$

Here, index a is summed up to D'. We can now approximate M' by M by only keeping the largest D singular values of S as

$$M^{i;\sigma_i}_{b_i b_{i+1}} = \sum_{a=0}^{D} U^{\sigma_i}_{b_i a} S_{aa} \left(V^\dagger\right)_{a b_{i+1}}. \tag{4.10}$$

To move to site $i+1$, one assign the truncated U to be the new left-normalized site tensor A^i, and multiply the truncated S and $V^\dagger$ into B^{i+1} to generate the new site tensor M'^{i+1}. The truncation error ϵ_i for each site tensor is equal to the square root of the sum of the square of the dropped singular values

$$\epsilon_i = \sqrt{\sum_{a=D+1}^{D'} S^2_{aa}}. \tag{4.11}$$

The overall error induced by such a compression can be approximated by $\epsilon = \sum_i \epsilon_i \approx L\sqrt{t_w}$, where t_w is the uniform truncation weight during the calculation. One important aspect of non-critical quasi-one-dimensional systems is, for most scenarios, that the singular values decrease very quickly (exponentially for gaped systems). Hence, the compressed MPS can form a very good representation of the original one.

Note that the SVD compression of an MPS is purely local and has an asymmetric effect for the first and last site: if we start from the left most site its truncation does not dependent on the right most site, while the truncation on the right most site instead shows a dependence on the left most site. To circumvent this problem, one can construct a variational optimization algorithm that treats all site tensors equally.

The variational compression algorithm of an MPS is an iterative sweeping mechanism which is commonly used in tensor product-state based algorithms: in order to find the global optimal solution, one sweeps multiple times through the system and finds the local optimal solution for each site. The Hilbert distance between the input MPS and output MPS reads

$$|||\psi'\rangle - |\psi\rangle|| = \langle\psi'|\psi'\rangle + \langle\psi|\psi\rangle - \langle\psi|\psi'\rangle - \langle\psi'|\psi\rangle. \tag{4.12}$$

Since $\{M^i\}$ is just a set of variational parameters, one can keep all tensors but M^i to be fixed and require a stationary solution with respect to M^i by differentiating the cost function to $\overline{M}^i$,

$$\frac{\partial}{\partial\overline{M^i}}|||\psi'\rangle - |\psi\rangle|| = \frac{\partial}{\partial\overline{M^i}}\left(\langle\psi|\psi\rangle - \langle\psi|\psi'\rangle\right) = 0. \tag{4.13}$$

Eq. (4.13) can be graphically represented as Fig. 4.4. Making use of the left- and right-normalization conditions for site tensors before and after the active site i, Eq. (4.13) can be reduced to

$$\delta_{b_i\bar{b}_i}\delta_{b_{i+1}\bar{b}_{i+1}}M^i_{b_ib_{i+1}} = L^i_{b_i\bar{b}_i}R^i_{b_{i+1}\bar{b}_{i+1}}M'^i_{b_ib_{i+1}}, \tag{4.14}$$

with L^i and R^i being the left and right rank-2 environment tensors satisfying the

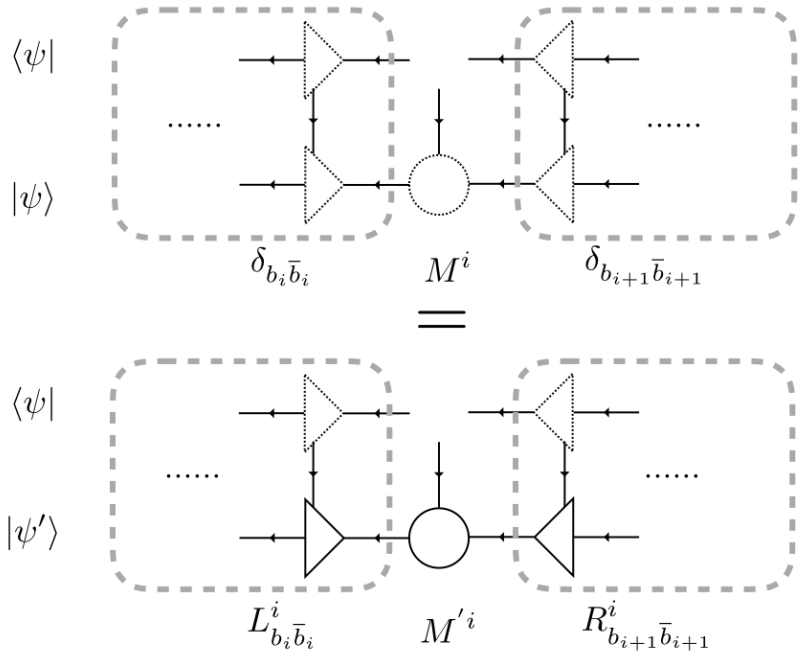

Figure 4.4: Graphic representation of the variational compression of the MPS. Here, we use dashed (real) triangles and circles to represent the target (input) tensors.

following recursive relations

$$L^{i+1}_{b_{i+1}\bar{b}_{i+1}} = \sum_{b_i,\sigma_i,\bar{b}_i} \left(L^i_{b_i\bar{b}_i} M'^{i;\sigma_i}_{b_i b_{i+1}} \right) M^{i;\sigma_i}_{\bar{b}_i\bar{b}_{i+1}}, \tag{4.15}$$

$$R^{i-1}_{b_i\bar{b}_i} = \sum_{b_{i+1},\sigma_i,\bar{b}_{i+1}} \left(R^i_{b_{i+1}\bar{b}_{i+1}} M'^{i;\sigma_i}_{b_i b_{i+1}} \right) M^{i;\sigma_i}_{\bar{b}_i\bar{b}_{i+1}}, \tag{4.16}$$

with boundary conditions $L^0_{b_0\bar{b}_0} = \delta_{b_0\bar{b}_0}$ and $R^{L-1}_{b_L\bar{b}_L} = \delta_{b_L\bar{b}_L}$.

To initialize the variational sweep process, one can start with a trial wave function from the SVD compression of $|\psi'\rangle$. By sweeping multiple times through the systems and solving the linear equation (4.14) for each site, a global optimized MPS with smaller bond dimension can be obtained . In order to make the bond dimension also adjustable, one can use a two-site variant of the single-site variational compression algorithm, i.e., instead of solving a local optimization problem for only one site tensor, one can form a local optimization problem for two site tensor $X'^{i,i+1} = M'^i \cdot M'^{i+1}$.

After obtaining the new two site tensors $X^{i,i+1}$, one decomposes it with a SVD $X^{i,i+1} \xrightarrow{\textbf{SVD}} U \cdot S \cdot V^{\dagger}$, and the new one site tensor is obtained by $U \xrightarrow{\text{reshape}} A^i$ and $S \cdot V^{\dagger} \cdot B^i \rightarrow M^{i+1}$ for left-to-right sweeping, and $V^{\dagger} \xrightarrow{\text{reshape}} B^{i+1}$, and $A^i \cdot U \cdot S \rightarrow M^i$ for right-to-left sweeping.

4.1.2 Orthogonalization of the MPS

Sometimes it is necessary to make a given MPS $|\psi\rangle$ to be orthogonal to a set of N MPSs $\{|\phi_o\rangle\}_0^{N-1}$. The most straightforward way do to this is the Gram-Schmidt orthogonalization procedure in which the target state $|\varphi\rangle$ is obtained as

$$|\psi\rangle - \frac{\langle\phi_0|\psi\rangle}{\langle\phi_0|\phi_0\rangle}|\phi_0\rangle \rightarrow |\varphi\rangle, \tag{4.17}$$

$$|\varphi\rangle - \frac{\langle\phi_o|\varphi\rangle}{\langle\phi_o|\phi_o\rangle}|\phi_o\rangle \rightarrow |\varphi\rangle, \text{for } 0 < o < N. \tag{4.18}$$

However, as mentioned in last section, since the MPS-MPS addition operation will increase the bond dimension, a compression of the resulting MPS is needed for each step of this process. The truncation error introduced by the MPS compression method then leads to a loss of orthogonality between $|\varphi\rangle$ and $|\phi_i\rangle$.

For MPS with large bond dimension, instead of using the Gram-Schmidt orthogonalization procedure, one can also target the desired state $|\varphi\rangle$ which minimizes the Hilbert distance

$$|||\varphi\rangle - |\psi\rangle||, \tag{4.19}$$

with the constraint that $\langle\varphi|\phi_o\rangle = 0$, for $o \in [0, N-1]$, in a variational manner. This is equivalent to minimize the following cost function

$$|||\varphi\rangle - |\psi\rangle + \sum_o \lambda_o\langle\varphi|\phi_o\rangle||, \tag{4.20}$$

with $\{\lambda_o\}$ being the Lagrange multipliers. By partially differentiating the cost function w.r.t the conjugate site tensor, we arrive at a set of tensor equations for the Lagrange multipliers as illustrated in Fig. 4.5. Vectors φ_i, ψ_i and ϕ_i^o represent the reshaped rank-3 tensors (with a dimension of $d \times m \times m$) for the desired state $|\varphi\rangle$, input $|\psi\rangle$ and orthogonal states $|\phi_o\rangle$, respectively. Let $\Phi_i = \{\phi_i^0, \cdots, \phi_i^{N-1}\}$ and

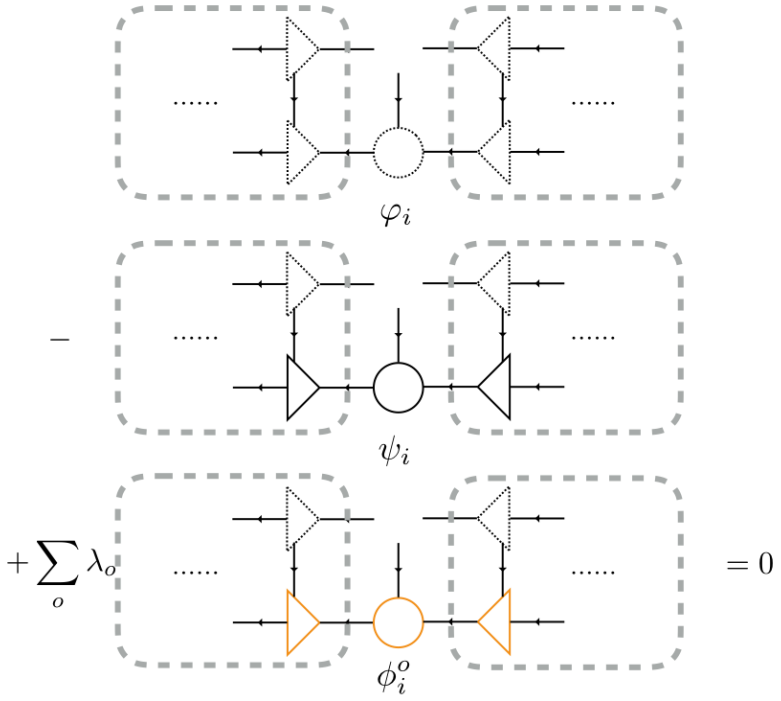

Figure 4.5: Graphic representation of the variational orthogonalization algorithm for the MPS. Here, site tensor with dark dashed, dark real and orange real edges belongs to the desired state $|\varphi\rangle$, input state $|\psi\rangle$ and orthogonal states $|\phi_o\rangle$, respectively.

$\Lambda_i = \{\lambda_i^0, \cdots, \lambda_i^{N-1}\}^T$, then the stationary equation represented in Fig. 4.5 can be reformulated as

$$\varphi_i - \psi_i + \Phi_i \cdot \Lambda_i = 0, \tag{4.21}$$

for each active site i. From the constraint that $\langle\phi_o|\varphi\rangle = 0$, we have $\phi_i^{o\dagger} \cdot \varphi_i = 0$ for $o \in [0, N-1]$. Multiplying $\Phi_i^\dagger$ from left hand side to Eq. (4.21), we arrive at

$$\Lambda_i = \left(\Phi_i^\dagger \cdot \Phi_i\right)^{-1} \Phi_i^\dagger \psi_i. \tag{4.22}$$

Note that, $\Phi_i^\dagger \psi_i$ is the vector (size N) of overlaps between the orthogonality vectors ϕ_i^o and input vector ψ_i, while $\Phi_i^\dagger \cdot \Phi_i$ is the matrix (of size $N \times N$) of overlaps between the orthogonality vectors ϕ_i^o. Since N is usually small, the vector of Lagrange multipliers can be computed exactly from Eq. (4.22). After obtaining $\{\Lambda_i\}$, it is straightforward

to update the target site tensor by Eq. (4.21).

Because of the variational nature of this orthogonalization procedure, there are two potential pitfalls concerning the limited variational space: first, according to Eq. (4.21), the variational space is bounded by the bond dimension of the input state. Hence, in order to allow for an increase of the variational space, one can adapt a two-site variant of the above algorithm and adjust the bond dimension dynamically by a SVD truncation threshold. But it will also induce a truncation error after the orthogonaliztion on each site. Hence, the best way to adjust bond dimension of the target state is to firstly apply the two-site algorithm for a few sweeps to make the bond dimension large enough, and then a few more one-site sweeps are applied to target the final desired state that is perfectly orthogonal to $\{|\phi_o\rangle\}_0^{N-1}$; second, even though the bond dimensions of site tensors in the central regions of an MPS can be quite large, their values are usually very small in the regions close to the two leads. For instance, in the ground state of the Anderson impurity model, the bond dimension far away from the impurity will be around $1-10$. Such a small bond dimension will again limit the available variational space and make the orthogonaliztion process problematic. One way to avoid this problem is, in the fist sweep, to require the target state to be orthogonal to a subset of $\{|\phi_o\rangle\}$ to make sure that the resulting φ_i has a norm larger than $\alpha|\psi_i|$ with α being a small threshold (typically we use $1e^{-3}$). Then, in the second sweep, this condition is ignored, and the set of orthogonal states is restored.

4.2 Matrix Product Operator

Once we have represented the many-body wave function in the MPS form, the Hamiltonian can also be formulated as matrix product operator (MPO). A general operator $\hat{O}$ that lives on a Hilbert space $\mathcal{H} = \bigotimes_0^{L-1} \mathcal{H}_i$, with $\mathcal{H}_i$ being the local Hilbert space on site i spanned by local basis set $\{|\sigma_i\rangle\}$, can be written as

$$\hat{O} = \sum_{\{\sigma_i\},\{\sigma_i'\}} o_{\sigma_0\cdots\sigma_{L-1};\sigma_0'\cdots\sigma_{L-1}'} |\sigma_0\cdots\sigma_{L-1}\rangle\langle\sigma_0'\cdots\sigma_{L-1}'|, \tag{4.23}$$

with $o_{\sigma_0\cdots\sigma_{L-1};\sigma_0'\cdots\sigma_{L-1}'}$ being a rank$-d^{2L}$ tensor. d is the dimension of the local Hilbert space. Similar to MPS that presents an efficient parameterization of the rank$-d^L$

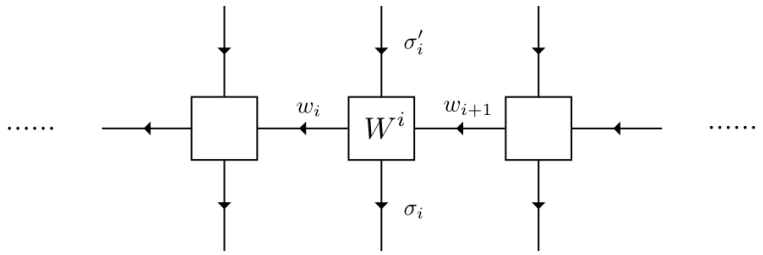

Figure 4.6: Graphic representation of the MPO. Each rank-4 site tensor W^i has two physical legs $\{\sigma_i', \sigma_i\}$ and two bond legs $\{w_i, w_{i+1}\}$.

wave function coefficient, MPO presents an efficient parameterization of this rank-d^{2L} coefficient by a contraction of L rank-4 tensors,

$$\hat{O} = \sum_{\{\sigma_i\},\{\sigma_i'\}} W^{0;\sigma_0\sigma_0'}_{w_0 w_1} \cdots W^{L-1;\sigma_{L-1}\sigma_{L-1}'}_{w_{L-1} w_L} |\sigma_0 \cdots \sigma_{L-1}\rangle\langle\sigma_0' \cdots \sigma_{L-1}'|. \tag{4.24}$$

A graphic representation of MPO is illustrated in Fig. 4.6. For each site tensor $W^{i;\sigma_i\sigma_i'}_{w_i w_{i+1}}$, we can view it as a matrix with elements being the local operators $\left(W^{i;\sigma_i\sigma_i'}\right)_{w_i w_{i+1}}$, i.e., the outer matrix indices are bond indices and inner matrix indices are physical indices. The bond dimension w_i of an MPO is determined by its underlying interaction form. We take the Hamiltonian with nearest-neighbor interaction terms as an example:

$$\hat{H} = \sum_i \left(\hat{O_i}^\dagger \cdot \hat{O}_{i+1} + \hat{O}_{i+1}^\dagger \cdot \hat{O}_i\right) + \sum_i Z_i, \tag{4.25}$$

where $\hat{O}_i$ and $\hat{Z}_i$ are arbitrary local operators. Its MPO representation has the following rank-4 tensors: for site $0 < i < L-1$

$$W^i = \begin{pmatrix} \hat{I} & 0 & 0 & 0 \\ \hat{O}^\dagger & 0 & 0 & 0 \\ \hat{O} & 0 & 0 & 0 \\ \hat{Z} & \hat{O} & \hat{O}^\dagger & \hat{I} \end{pmatrix}, \tag{4.26}$$

while for the first and last sites

$$W^1 = \begin{pmatrix} \hat{Z} & \hat{O} & \hat{O}^\dagger & \hat{I} \end{pmatrix}, \tag{4.27}$$

$$W^{L-1} = \begin{pmatrix} \hat{I} \\ \hat{O}^\dagger \\ \hat{O} \\ \hat{Z} \end{pmatrix}. \tag{4.28}$$

Since $\hat{O}$, $\hat{O}^\dagger$ and $\hat{Z}$ are local operators, they usually have only few non-zero matrix elements. For instance, the electron creation operator $c^\dagger_\sigma$ has the following matrix representation

$$c^\dagger_\uparrow = \begin{pmatrix} 0 & 0 & 0 & 0 \\ 1 & 0 & 0 & 0 \\ 0 & 0 & 0 & 0 \\ 0 & 0 & 1 & 0 \end{pmatrix}, c^\dagger_\downarrow = \begin{pmatrix} 0 & 0 & 0 & 0 \\ 0 & 0 & 0 & 0 \\ 1 & 0 & 0 & 0 \\ 0 & -1 & 0 & 0 \end{pmatrix}, \tag{4.29}$$

in the local basis spanned by $\{|\emptyset\rangle, |\uparrow\rangle, |\downarrow\rangle, |\uparrow\downarrow\rangle\}$ representing an empty state, a spin up electron occupied state, a spin down electron occupied state and a double occupied state, respectively. The minus sign in $c^\dagger_\downarrow$ comes from the local anti-commutative relation of fermions. Together with Eq. (4.26), we can see that W^i is sparse. Furthermore, unlike the bond dimension of MPS which shows an exponential growth with the system size, w_i has a constant value in this example. Generally, the bond dimension of MPO has a polynomial dependence on the range of interactions.

For a general Hamiltonian with complicated interactions, it is usually not possible to construct each W^i analytically as we have done in the above example. To handle complicated interactions, one can follow the so called finite-state machine

(FSM) [102, 103] which generates the MPO representation in an automatic way. However, as shown in [104], the FSM method becomes extremely complicated for system on a cylinder geometry (quasi two-dimensional stripe with open boundary condition in the $x-$direction and periodic boundary condition in the $y-$direction). In our implementation, we follow the compression method presented in [105], which is able to handle complicated interactions automatically while keeping the desired sparsity in the generated MPO. The basic idea is the following: we first construct the MPS representation of the single-site operators appeared in the given Hamiltonian and then use them as the basic ingredients to generated the individual terms in the Hamiltonian. The compression methods of the generated MPO work similarly to the SVD compression of MPS, i.e., for a given site tensor $W^{'i}$ of the original MPO , it is possible to find a new site tensor W^{i} with a smaller bond dimension satisfying

$$W^{'i;\sigma_i\sigma_i'}_{w_ip} = \sum_{p} W^{i;\sigma_i\sigma_i'}_{w_iw_{i+1}} T_{w_{i+1}p}, \tag{4.30}$$

with $p < w_{i+1}$. T is the transfer tensor and is absorbed into the next site tensor which is to be compressed. Different from the SVD compression of MPS in which we have $T = S \cdot V^T$ for left-to-right sweeping, usually, the transfer tensor T can not be obtained by a direct SVD of W^i [105]. The reasons for its failure are: first, as already indicated in Eq. (4.26), the site tensors are usually very sparse, and SVD of such a sparse tensor will result a dense S tensor with slowly decaying elements, which makes the truncation framework very inefficient; second, unlike the MPS which is normalized, the norm of MPO grows with the system size L. Hence, after a direct left-to-right or right-to-left SVD sweep, we will have $L-1$ bulk site tensors with elements of order 1, and one edge tensor (the first or last tensor) with exponentially large elements, which will compromise the accuracy of our calculations. To circumvent these difficulties, instead of using a direct SVD compression, one can apply the rescaled-SVD, deparallelisation and delinearisation method to compress the encountered Hamiltonian (as implemented in this thesis). For details of these algorithms we refer the reader to the original literature [105].

4.3 Applying the MPO to MPS

Applying an MPO onto an MPS is a commonly used operation in MPS related algorithms. For instance, in the calculation of single-particle Green's function within the Krylov subspace framework, the Krylov vectors are generated by applying $\hat{H}$ successively on the excited state. If the MPO is a single-site operator, then, except for the active site (where the single-site operator act on), the site tensors are left unchanged. Hence, the naive direct tensor multiplication, i.e.,

$$M'^{i;\sigma'_i}_{b'_i b'_{i+1}} = \sum_{\sigma_i} W^{i;\sigma_i\sigma'_i}_{w_i w_{i+1}} M^{i;\sigma_i}_{b_i b_{i+1}}, \tag{4.31}$$

is applicable. Where M^i and M'^i present the MPS site tensor before and after the application of the MPO (with site tensor being W^i), respectively. $b'_i = b_i \otimes w_i$ and $b'_{i+1} = b_{i+1} \otimes w_{i+1}$. However, if the MPO is not a single-site operator which makes $w_i \neq 1$, the resulting MPS will have a bond dimension of mk, with k being the bond dimension of the MPO. Since typical values of k would be around $10-100$, depending on the underlying system, it is highly desirable to have an efficient way to truncate the bond dimension from km back to m (or some value $m' < km$). As indicated in Eq. (4.31), one should also note that the application of MPO to an MPS in the naive way will destroy the orthogonality existing in the original MPS. So, if one performs a sweep of SVD truncation to the resulting MPS, the computational cost will be $\sim Ld^3k^3m^3$, which is highly inefficient.

One way to circumvent this problem is, similar to the variational compression algorithm for MPS elaborated in Sec. 4.1.1, to use a variational algorithm to minimize the Hilbert distance

$$|||\psi'\rangle - \hat{O}|\psi\rangle||, \tag{4.32}$$

with $|\psi'\rangle$ being our compressed MPS with a bond dimension of $m' < km$. However, since this process is purely local and is restricted by the number of variational parameters if $\hat{O}$ has long-range interactions or the resulting MPS is far away from its original one, it may fail to converge.

An alternative way to this problem is the so called zip-up algorithm [106] which begins by first bringing the input MPS into a right-normalized form, i.e., moving the

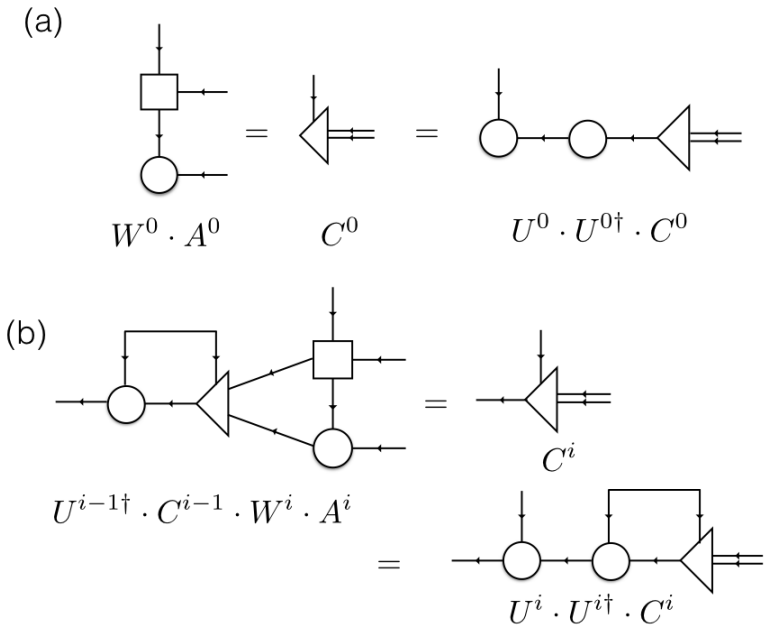

Figure 4.7: Graphic representation of the construction of (a) C^0 and (b) C^i tensor in the zip-up algorithm.

the orthogonality center to the first site, then it constructs the C tensors on the first site as

$$C^{0;\sigma_0}_{w_1 b_1} = \sum_{\sigma_1'} W^{0;\sigma_1\sigma_1'}_{w_1} A^{0;\sigma_1'}_{b_1}. \tag{4.33}$$

A SVD of C^0 is performed by regrouping its indices as $(\sigma_0, (w_1 b_1))$,

$$C^{0;\sigma_0}_{(w_1 b_1)} = \sum_{\alpha} U_{\sigma_0 \alpha} S_\alpha V^\dagger_{\alpha(w_1 b_1)}. \tag{4.34}$$

Here, we can perform a truncation of the singular values either according to a fixed maximal bond dimension or a singular value threshold. The truncated U^0 tensor is assigned to be the new site tensor, which is left-normalized by construction. Then

the successive C^i and site tensors U^i can be generated recursively as

$$C^{i;\alpha\sigma_i}_{w_{i+1}b_{i+1}} = \sum_{\beta\sigma_{i-1}\sigma_i' b_i w_i} \left(U^{i-1\dagger}\right)^{\sigma_{i-1}}_{\alpha\beta} C^{i-1;\beta\sigma_{i-1}}_{w_i b_i} W^{i;\sigma_i\sigma_i'}_{w_i w_{i+1}} A^{\sigma_i'}_{b_i b_{i+1}}, \tag{4.35}$$

$$C^{i;\alpha\sigma_i}_{(w_{i+1}b_{i+1})} = \sum_{\beta} U^{i;\sigma_i}_{\alpha\beta} S_\beta V^\dagger_{\beta(w_{i+1}b_{i+1})}. \tag{4.36}$$

A graphic representation of this algorithm is presented in Fig. 4.7. If we assume $k < m$ (usually satisfied), the leading computational cost which comes from the contraction of C^{i-1} with A^i is $\sim m^3kd$. After reaching the last site, a further right-to-left SVD sweep is performed to reduce the bond dimension to the desired value.

4.4 Ground state optimization: Density-Matrix Renormalization Group

Density-matrix renormalization group (DMRG) is a variational optimization algorithm which targets the ground state by sweeping iteratively throughout the system. For a given Hamiltonian $\hat{H}$ represented by a MPO with site tensors $\{W^i\}$, its ground state $|\psi\rangle$ is defined by the state which minimizes the energy

$$\mathbf{min}_{|\psi\rangle} \left(\frac{\langle\psi|\hat{H}|\psi\rangle}{\langle\psi|\psi\rangle} \right), \tag{4.37}$$

with the constraint that $\langle\psi|\psi\rangle = 1$. This is equivalent to

$$\mathbf{min}_{|\psi\rangle} \left(\langle\psi|\hat{H}|\psi\rangle - \lambda\langle\psi|\psi\rangle \right), \tag{4.38}$$

by introducing a Lagrangian multiplier λ. The tensors $\{M^i\}$ in the MPS serve as a set of variational parameters. It is impractical to optimize all the parameters at the same time, and the idea of DMRG is to introduce a sweeping process, similar to the variational algorithms for compression and orthogonalization of MPS which optimize a single site tensor each time. In other words, DMRG translates a global optimization problem into a series of iteratively constructed local problems. To achieve this, we start by partially differentiating Eq. (4.38) w.r.t. $M^{i\dagger}$ and requiring a stationary

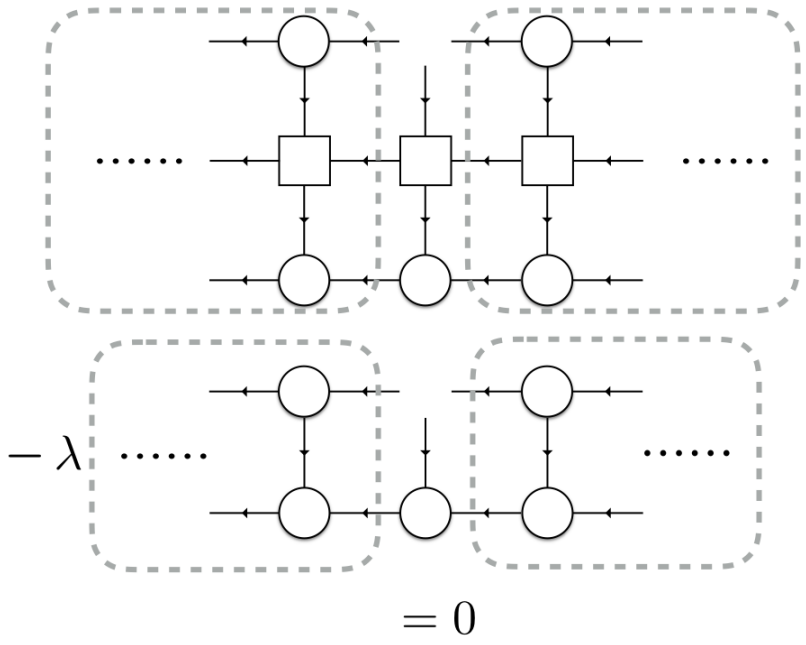

Figure 4.8: Graphic representation of Eq. (4.39).

condition as

$$\frac{\partial}{\partial M^{i\dagger}}\Big(\langle\psi|\hat{H}|\psi\rangle - \lambda\langle\psi|\psi\rangle\Big) = 0, \tag{4.39}$$

the resultant tensor equation can be graphically represented by Fig. 4.8. If i is the orthogonality center, this equation can be further reduced to

$$H^i_{\text{eff}} \cdot M^i = \lambda M^i. \tag{4.40}$$

Here $H^i_{\mathbf{eff}}$ is the effective Hamiltonian acting on the site wave function M^i, which can be constructed as

$$H^{i;\sigma_i\sigma_i'}_{b_i b_i' b_{i+1} b_{i+1}'} = \sum_{w_i w_{i+1}} L^i_{b_i b_i' w_i} W^{i;\sigma_i\sigma_i'}_{w_i w_{i+1}} R^i_{b_{i+1} b_{i+1}' w_{i+1}}, \tag{4.41}$$

where the left- and right-environment tensors L^i and R^i are constructed recursively as

$$L^i_{b_i w_i b'_i} = \sum_{b_{i-1}\sigma_{i-1}\sigma'_{i-1}w_{i-1}b'_{i-1}} L^{i-1}_{b_{i-1}w_{i-1}b'_{i-1}} A^{i-1;\sigma_{i-1}}_{b_{i-1}b_i} W^{i-1;\sigma_{i-1}\sigma'_{i-1}}_{w_{i-1}w_i} A^{i-1\dagger;\sigma'_{i-1}}_{b'_{i-1}b'_i}, \tag{4.42}$$

$$R^{i-1}_{b_i w_i b'_i} = \sum_{b_i\sigma_i\sigma'_i w_{i+1}b'_{i+1}} R^i_{b_{i+1}w_{i+1}b'_{i+1}} A^{i;\sigma_i}_{b_i b_{i+1}} W^{i;\sigma_i\sigma'_i}_{w_i w_{i+1}} A^{i\dagger;\sigma'_i}_{b'_i b'_{i+1}}, \tag{4.43}$$

with the boundary condition $L^0 = \mathbb{I}, R^{L-1} = \mathbb{I}$.

Eq. (4.40) can be recast into a standard eigenvalue problem by reshaping the site tensor M^i into a vector with dm^2 elements, while $H^i_{\mathbf{eff}}$ is reshaped into a matrix with dimension of $dm^2 \times dm^2$. Such an eigenvalue problem can be efficiently solved by the standard Lanczos algorithm to find the extreme eigenvalue and eigenvector. The updated M^i is obtained by reshaping the eigenvector corresponding to the lowest eigenvalue back to a rank-3 tensor.

Similar to all the variational methods introduced in this chapter, the simple single-site DMRG algorithm presented above can be trapped into a local minimum because of the limited variational space. The most straightforward way to go around this difficulty is to target two optimized site tensors instead of just one optimized site tensor each time. However, there are two possible drawbacks of this two-site variant: first, the computational cost of two-site DMRG scales as $\sim m^4$ for the leading term (single-site DMRG scales as $\sim m^3$), which is unfavorable for systems with large bond dimension; second, it is very slow to include long-range correlations in two-site DMRG, because, by construction, only nearest-neighbor sites can exchange particles. In order to stay in the single-site framework, alternative methods based on the density-perturbation and subspace expansion have been introduced in recent years. Details about these algorithms can be found in the original literature [107, 108].

5

Matrix Product States based impurity solver in frequency-domain

Parts of the contents presented in this chapter have been published in "Natural-Orbital Impurity Solver and Projection Approach for Green's Function", Yi Lu, **Xiaodong Cao**, Philipp Hansmann and Maurits W. Haverkort, ***Phys.Rev.B 100, 115134, 16 September 2019***

In this Chapter, we demonstrate advantages of the natural-orbital representation of the impurity model. Especially, by exploiting the energy separation of states provided by the natural-orbital representation, we propose to calculate the ground state and Green's functions of the impurity model (with a few hundred spin-orbitals) by projecting the full Hilbert space to a small subspace. The proposed projection approach is applicable for all real-space wave-function based methods and can be straightforwardly implemented in DMRG and ED. We further provide a simplification of the proposed projection scheme, which allows for efficient and accurate solution of the full impurity model by solving a subsystem with only up to dozens of spin-orbitals.

5.1 Impurity Hamiltonian

A general Anderson impurity model is described by the Hamiltonian H_{A} that contains two parts

$$H_{\mathrm{A}} = H_{\mathrm{loc}} + H_{\mathrm{bath}}, \tag{5.1}$$

where a locally interacting impurity site (H_{loc}) is coupled to a non-interacting bath (H_{bath}). There are several special cases which are of interest for the following discussions: i). **Single-band Anderson impurity model**

$$H_{\mathrm{loc}} = U n_{d\uparrow} n_{d\downarrow} + \epsilon_d n_d, \tag{5.2}$$

$$H_{\mathrm{bath}} = \sum_{l=0,\sigma}^{N_b-1} \left(v_l c_{l\sigma}^{\dagger} d_{\sigma} + v_l^{*} d_{\sigma}^{\dagger} c_{l\sigma} \right) + \sum_{l=0}^{N_l-1} \epsilon_l n_{l\sigma}, \tag{5.3}$$

where $d_{\sigma}^{\dagger}$ and d_{σ} are the electron creation and annihilation operator on the impurity site with spin $\sigma = \{\uparrow, \downarrow\}$, $c_{l\sigma}^{\dagger}$ and $c_{l\sigma}$ are the creation and annihilation operators on bath site l with spin σ; $n_{d\sigma} = n_{d\uparrow} + n_{d\downarrow}$ is the density operator on the impurity site with spin σ; $n_{l\sigma} = n_{l\uparrow} + n_{l\downarrow}$ is the density operator on $l-$th bath site with spin σ. The hybridization function can be extracted from the set of parameters $\{v_l, \epsilon_l\}$ as

$$\Delta(\omega) = \sum_{l} \frac{|v_l|^2}{w - \epsilon_l}. \tag{5.4}$$

For the Bethe lattice, the bath has a semielliptic spectral function as

$$-\frac{1}{\pi}\Delta(\omega) = \frac{2}{\pi D}\sqrt{1 - \left(\frac{\omega}{D}\right)^2}, \tag{5.5}$$

where D is the half-band width. With a given hybridization function $\Delta(\omega)$, the set of bath parameters $\{v_l, \epsilon_l\}$ can be obtained by discretizing $\Delta(\omega)$ on the frequency-axis

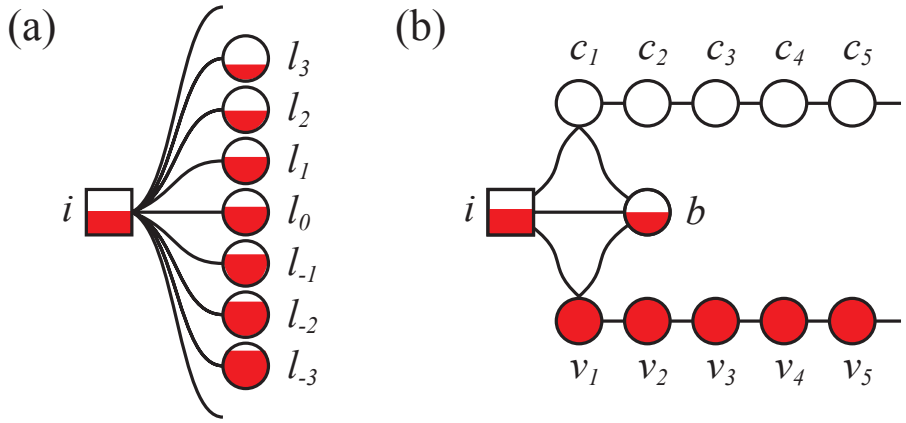

Figure 5.1: Graphical representation of an impurity model in (a) the conventional "star" geometry and (b) the natural-orbital geometry (see text). The impurity is represented by a square and bath by circles. The solid lines denote hoppings between two "sites". Each site consists of m spin-orbitals.

into $N_l = l$ intervals $\{I_l\}$ as

$$v_l^2 = \int_{I_l} d\omega \left[-\frac{1}{\pi} \mathrm{Im}\Delta(\omega) \right], \tag{5.6}$$

$$\epsilon_l = \frac{1}{v_l^2} \int_{I_l} d\omega\omega \left[-\frac{1}{\pi} \mathrm{Im}\Delta(\omega) \right]. \tag{5.7}$$

ii). **Multi-band Model**. For a multi-orbital impurity model, the interaction term is typically assumed to have a Kanamori form

$$H_{\mathrm{loc}} = H_{\mathrm{DD}} + H_{\mathrm{SF-PH}}, \tag{5.8}$$

$$H_{\mathrm{DD}} = U \sum_m n_{m\uparrow} n_{m\downarrow} + (U - 2J) \sum_{m'>m,\sigma} n_{m\sigma} n_{m'\bar{\sigma}} + (U - 3J) \sum_{m'>m,\sigma} n_{m\sigma} n_{m'\sigma},$$

$$H_{\mathrm{SF-PH}} = J \sum_{m'm} \left(d^\dagger_{m\uparrow} d_{m\downarrow} d_{m'\uparrow} d^\dagger_{m'\downarrow} + h.c. \right) - J \sum_{m'>m} \left(d^\dagger_{m\uparrow} d^\dagger m \downarrow d_{m'\uparrow} d_{m'\uparrow} + h.c. \right), \tag{5.9}$$

where H_{DD} describes the density-density interaction terms and $H_{\mathrm{SF-PH}}$ describes the spin-flip and pair-hopping terms. U is the Hubbard interaction and J is the Hund's coupling.

Star representation of the Hamiltonian (5.1) is depicted in Fig. 5.1(a).

5.1.1 Natural-orbital representation of an impurity model

The *natural orbitals* are defined as a single-particle basis set on which the ground-state single-particle density matrix of a quantum system is diagonal. They are widely used in quantum chemistry [109] as they have several advantageous features for molecular systems such as optimal convergence properties for the wave functions and energies. In the context of quantum impurity problems, they have been discussed in conjunction with configuration interaction (CI) expansion approximation [72, 73]. These methods have proven to be capable of solving impurity problems exceeding the size of those dealt with by conventional ED [68]. The caveat of employing natural orbitals for impurity models is that a naive implementation that diagonalizes the density matrix of the *whole* system inevitably mixes the impurity states with the non-interacting bath states. This transforms the original local interactions (contained in H_{loc}) into long range ones and turns a locally correlated problem into a fully correlated one, which may bring a severe penalty that overcomes the advantage of the natural orbitals, especially for large systems that contains $\mathcal{O}(10^2)$ bath sites.

In Ref. [74], a natural-orbital representation of the impurity model by restricting the optimization of the basis set only for the bath degrees of freedom was introduced. It was shown that an ED solver employing such a natural-orbital basis set substantially outperforms conventional ones and is capable of solving impurity models with the number of bath sites comparable to that achieved by NRG or DMRG solvers [74]. The resulting geometry of the impurity Hamiltonian is graphically represented in Fig. 5.1(b). The procedure for obtaining such a representation is detailed in Ref. [74]. We briefly recapitulate the steps here:

- Solve Hamiltonian (5.1) (as depicted in Fig. 5.1(a)) within mean-field methods (e.g. Hartree-Fock) and obtain the ground-state single-particle density matrix $\hat{\rho}^{\mathrm{MF}} = \left(\begin{smallmatrix} \hat{\rho}_i & \hat{\rho}_{il} \\ \hat{\rho}_{li} & \hat{\rho}_l \end{smallmatrix}\right)^{\mathrm{MF}}$, where we distinguish the impurity (i) and bath (l) parts explicitly.

- Diagonalize the bath density matrix $\hat{\rho}_l^{\mathrm{MF}}$, which leads to a new set of bath orbitals with occupation of either 0 or 1, with the exception of m (the number of impurity spin-orbitals) orbitals that have fractional occupation. We assign these orbitals to site b as shown in Fig. 5.1(b). Its density matrix $\hat{\rho}_b^{\mathrm{MF}}$ satisfies the relation $\mathrm{Tr}\hat{\rho}_b^{\mathrm{MF}} = m - \mathrm{Tr}\hat{\rho}_i^{\mathrm{MF}}$.

- Linearly combine the impurity site i and bath site b into "bonding" and "anti-bonding" sites with occupation m and 0. The former (latter) only couples to the completely filled (empty) bath sites obtained from last step, respectively. The mean-field Hamiltonian has now been separated into two decoupled terms, which describes the filled and empty spin-orbitals of the complete single-particle Hilbert space, respectively.

- Perform unitary transformation (Lanczos tridiagonalization) on the two parts of the Hamiltonian and obtain two separate empty and filled "chains" starting with the bonding and anti-bonding sites, respectively.

- Finally, reverse the unitary transformation in step (iii) and recover the i and b sites, which now couple to both the empty and filled chains. Following the convention in Ref. [74], we dub the two chains "conduction" and "valence" baths, respectively.

In the limit of $U \to 0$, these mean-field natural orbitals are exact, and the many-body ground state of the exact impurity solution can be written out using only $2m$ Slater determinants [74]. At finite U values, the exact occupation of the conduction or valence bath sites will deviate from 0 or 1, necessitating the inclusion of more states with excited electrons or holes in the conduction or valence chains. Nonetheless, the "leakage" of electrons (holes) onto a conduction (valence) site is expected to rapidly decay as a function of its distance to the impurity site, as states with electrons (holes) deep in the conduction (valence) chain are energetically unfavorable. This allows for an efficient description of the ground state and the low-energy excitations by only including states with electron (hole) excitations in the conduction (valence) bath that are localized around the impurity site.

5.2 Comparing the natural-orbital and star representation

As discussed in Ref. [93], although the star configuration introduces long-range hopping terms in the Hamiltonian, it has better performance compared with the chain configuration. The reason is that, in star configuration, the electron occupations on most bath sites are very close to empty or full. In the following discussions, we will

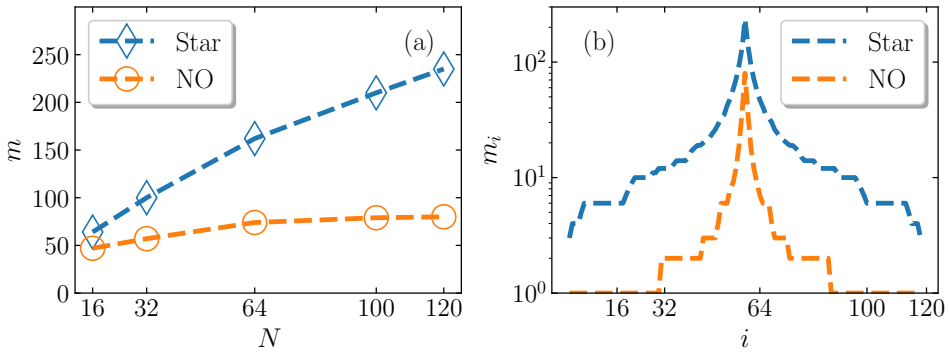

Figure 5.2: Comparison the ground state properties in the star and NO configurations. Parameters are chosen as: half-band width $D = 1$, interaction strength $U = 2D$, two-site DMRG truncation weight $t_w = 1e^{-10}$. (a) the maximal bond dimensions of the ground states in the star (blue diamond) and NO (origin cycle) basis as functions of the number of bath sites N; (b) the bond dimension distribution through the system with $N = 120$ for star (blue dashed line) and NO (origin dashed line) configuration. "NO" is the abbreviation of "natural-orbital".

only focus on the comparison between star and natural-orbital configurations by using the half-filling single-band Anderson impurity model as an example.

As the first comparison, we plot the maximal MPS bond dimension m throughout the system as function of number of bath sites N_l in Fig 5.2(a). There are two aspects we want to emphasize: first, with a fixed number of bath sites, the bond dimension of the ground state in the natural-orbital configuration is much smaller than the one in the star configuration, and this difference becomes larger as N_l gets increased; second, different from the much faster growth of m in the star configuration as N_l is increased, bond dimension in the natural-orbital configuration increases only slightly. The almost independent maximal bond dimension m against the number of bath sites in the natural-orbital configuration has a significant impact on the application of the MPS based method as an impurity solver for DMFT. Because, usually, different from the case on the imaginary-axis, the DMFT self-consistent loop on real axis needs a more refined resolution of the hybridization function to converge, meaning that a much larger number of bath sites are needed on real axis calculations. Hence, if we can have an almost constant maximal bond dimension after some number of bath sites, the overall computational cost (typically $\sim m^3$) can be tremendously reduced. These two ground state features of natural-orbital configuration highlight its advantage to

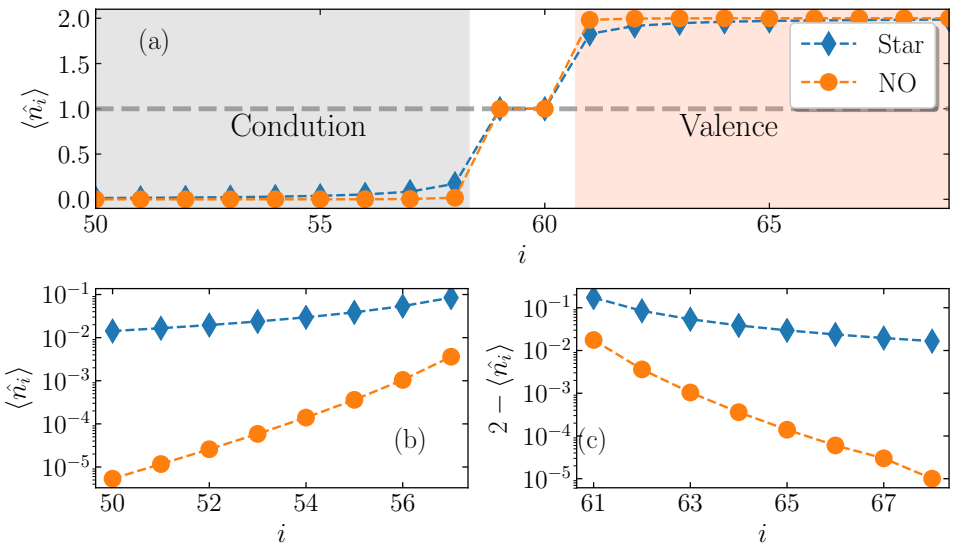

Figure 5.3: Comparison of ground state density distribution in the star and natural-orbital configurations. Parameters are chosen the same as Fig. 5.2 for $N = 120$. (a) density distribution of the ground state for the star (blue diamond) and natural-orbital (origin cycle) configuration. (b) and (c) log plot of the density distribution in the conduction and valence chain, respectively. "NO" is the abbreviation of "natural-orbital".

the star configuration which is commonly used in literature. Furthermore, as depicted in Fig 5.2(b), compared to the star configuration, the natural-orbital configuration will not only result in a much smaller maximal bond dimension, but the overall bond dimension distribution through the whole system has also a better profile.

The reason that the natural-orbital configuration has a better representativity than the usual implemented star (and also chain) configuration can be revealed in the ground state density distribution as depicted in Fig. 5.3. Although, both star and natural-orbital configuration have a similar density distribution profile, the bath site density shows an exponential convergence to empty for conduction chain and full for valence chain as a function of its distance to the impurity site in natural-orbital configuration, while its convergence is much slower in star configuration.

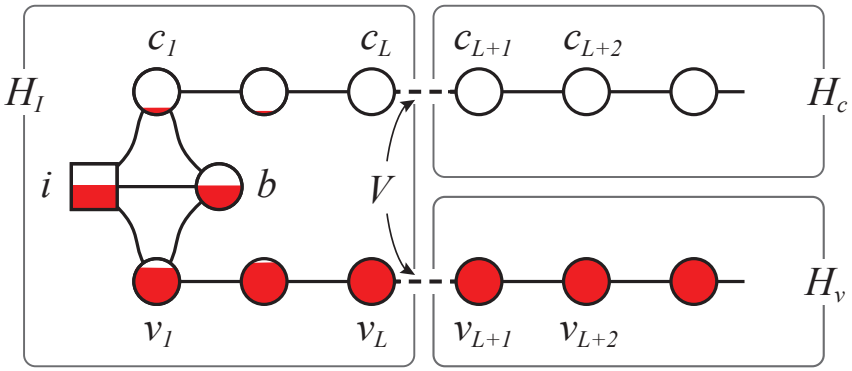

Figure 5.4: Separating the full Anderson impurity Hamiltonian H_{A} defined on the natural orbitals into four parts H_{I}, H_{c}, H_{v}, and V. Each Hamiltonian acts on the sites enclosed by its corresponding box. The hybridization operator V (dashed bonds) connects H_{I} to H_{c} and H_{v}. H_{c} are H_{v} are termed as projection region.

5.3 Ground-state projection

So far we have rewritten the impurity Hamiltonian (5.1) on the natural-orbital basis and shown the fast convergence of the density distribution in this basis. Such a representation has an optimal scaling behavior with respect to the number of bath sites, as adding empty (filled) bath sites at the end of the conduction (valence) chains incurs little to none cost for describing the ground state. However, the computation complexity is still expected to scale exponentially with the number of impurity spin-orbitals, which may become intractable for full d/f-orbital impurities that are each coupled to a few hundred bath sites.

To further reduce the computation cost and alleviate the scaling problem for the ground state, we propose to project the full Hilbert space onto a subspace that only contains states with completely empty conduction (filled valence) sites with indices $l > L$ (Fig. 5.4), with L as a tunable parameter controlling the trade-off between projection accuracy and computation cost. Note that a single L is used here for simplicity. For a general multi-orbital impurity model, L does not need to be the same for the conduction and valence bath or for different spin-orbitals. The projection essentially separates the full Hamiltonian H_{A} into three parts: an impurity Hamiltonian H_{I} of a much smaller system, as well as H_{c} and H_{v} describing

two truncated bath chains that are coupled to H_{I} via hybridization V. The Anderson impurity Hamiltonian is then

$$H_{\mathrm{A}} = H_0 + V, \tag{5.10}$$

where

$$H_0 = H_{\mathrm{I}} + H_{\mathrm{v}} + H_{\mathrm{c}}. \tag{5.11}$$

The projected ground state wave function is given as

$$|\Phi_0\rangle = |\phi_{\mathrm{I}}\rangle \otimes |0_c\rangle \otimes |1_v\rangle. \tag{5.12}$$

Here, $|\phi_{\mathrm{I}}\rangle$ is the exact ground state of H_{I} that can be efficiently computed by ED or DMRG methods for moderately large L, and $|0_v\rangle$ ($|1_c\rangle$) denotes the product states of completely empty conduction (filled valence) sites with indices $l > L$. $|\Phi_0\rangle$ is the exact solution of H_0. The projected ground-state energy is

$$E_0(L) \equiv \langle\Phi_0|H_{\mathrm{A}}|\Phi_0\rangle = \langle\phi_{\mathrm{I}}|H_{\mathrm{I}}|\phi_{\mathrm{I}}\rangle + \sum_{l>L,m} \epsilon^v_{lm}, \tag{5.13}$$

where the second term is the sum of on-site energies of all spin-orbitals with indices m at each site l in the truncated valence chain. The accuracy of the projected ground-state wave function can be assessed by calculating the deviation of Eq. (5.13) from the exact ground-state energy when the latter is attainable, or by calculating the energy variance of the projected ground-state using the full Hamiltonian H_{A} as

$$\begin{aligned} \delta E_0(L)^2 &\equiv \langle\Phi_0|H_{\mathrm{A}}^2|\Phi_0\rangle - E_0(L)^2 \\ &= \delta E_{\mathrm{I}}(L)^2 + \delta V(L)^2, \end{aligned} \tag{5.14}$$

with

$$\begin{aligned} \delta E_{\mathrm{I}}(L)^2 &= [\,\langle\phi_{\mathrm{I}}|H_{\mathrm{I}}^2|\phi_{\mathrm{I}}\rangle - \langle\phi_{\mathrm{I}}|H_{\mathrm{I}}|\phi_{\mathrm{I}}\rangle^2] \\ \delta V(L)^2 &= \langle\Phi_0|V^2|\Phi_0\rangle\,. \end{aligned}$$

The first term $\delta E_{\mathrm{I}}(L)^2$ is intrinsic to the numerical method of choice that solves H_{I}. The second term $\delta V(L)^2$ originates from the imposed projection and therefore scales exponentially to zero with increasing L.

5.3.1 Excited-state projection and Green's Functions

The central object of interest for an impurity problem is the impurity Green's function $G_{\mathrm{imp}}(\omega)$. On the *real-frequency* axis, it is defined as

$$G_{\mathrm{imp}}(\omega) = G^{+}(\omega) - G^{-}(-\omega)^{*}, \tag{5.15}$$

where $G^{\pm}(\omega)$ are the retarded Green's functions for electron addition $(+)$ and removal $(-)$ at the impurity site i:

$$G^{+}(\omega) = \lim_{\eta \to 0^{+}} \langle \Psi_0 | d \frac{1}{\omega - H_{\mathrm{A}} + i\eta} d^{\dagger} | \Psi_0 \rangle \,, \tag{5.16}$$

$$G^{-}(\omega) = \lim_{\eta \to 0^{+}} \langle \Psi_0 | d^{\dagger} \frac{1}{\omega - H_{\mathrm{A}} + i\eta} d | \Psi_0 \rangle \,, \tag{5.17}$$

with $|\Psi_0\rangle$ the impurity ground state. The Green's functions can be directly calculated in the frequency domain using the Lanczos method, which is an approach generally adopted in ED-based solvers [68, 69, 70, 71, 72, 73, 74]. For DMRG solvers, $G_{\mathrm{imp}}(\omega)$ is also commonly obtained via Fourier transform from the real-time Green's functions [110, 96]. While the proposed projection scheme is applicable for both methods, in this chapter, we will focus on the direct calculation in the frequency domain, while calculation in the time-domain is left to the next chapter.

The idea of our projection method is to obtain the impurity Green's function of the full system $G_{\mathrm{imp}}(\omega)$ from that of the projected system $G_0(\omega)$ given by H_0 and succesive non-perturbative expansion in the hybridization V. Such an expansion can in principle be done using diagrammatic methods and the Dyson equations. This requires knowledge not only on the impurity Green's function of H_0, but also on electron (hole) propagators starting at site c_L (v_L). Here, however, we employ a method based on Hilbert space reductions, which has the advantage that we can use standard Lanczos routines for solving the Green's functions of impurity models.

The method is based on the notion that we can connect to each operator H with a fixed number of electrons a Hilbert space $\mathcal{H}$. We start with the projected subspace $\mathcal{H}_0 = \mathcal{H}_{\mathrm{I}} \otimes |1_v\rangle \otimes |0_c\rangle$ defined for the ground-state calculation, where $\mathcal{H}_{\mathrm{I}}$ is the Hilbert space of the subsystem H_{I}. To obtain $G_0^{\pm}(\omega)$, we use the Lanczos method and construct a series of M Krylov vectors $|\tilde{\nu}_j\rangle = H_{\mathrm{I}}^{j} a_i^{(\dagger)} |\phi_{\mathrm{I}}\rangle \in \mathcal{H}'_{\mathrm{I}}$, where the prime denotes the Fock subspaces of electron removal (addition) with respect to $\mathcal{H}_{\mathrm{I}}$.

After orthogonalizing each $|\tilde{\nu}_j\rangle$ to the previous states and proper normalization, the resultant set of vectors $\{|\nu_j\rangle\}$ become the basis set of a subspace (Krylov space) $\mathcal{K}^M$ of $\mathcal{H}'_{\mathrm{I}}$ with dimension M. The Hamiltonian H_{I} is represented as a tridiagonal matrix $\overline{H}_{\mathrm{I}}$ on $\mathcal{K}^M$, and $G_0^{\pm}(\omega)$ can be straightforwardly calculated as the leading element of the resolvents $G_0^{\pm}(\omega) = (\omega + i\eta - \overline{H}_{\mathrm{I}})^{-1}_{00}$, which is conveniently expressed as a continued fraction [74]. The corresponding impurity Green's functions $G_0^{\pm}(\omega)$ are identical to those of the subsystem H_{I}.

The $G_0^{\pm}(\omega)$ obtained above are in general quite different from the Green's functions $G^{\pm}(\omega)$ of the full system, especially for small L values, due to the limited degrees of freedom. To obtain a more accurate description, we need to relax the projection condition to include more excited states. This can be done by allowing electron (hole) excitations into the completely empty conduction (filled valence) chains. As states with higher-order excitations are energetically more costly and therefore contribute less to the Green's functions, the number of excited particles p serves as a control parameter for the projection. Conceptually this is similar to the restricted active space method used in quantum chemistry.

The proposed projection scheme can be implemented in ED and DMRG solvers by targeting a specific $U(1)$ symmetry sector for the bath chains in each step of the Lanczos or time-evolution process when computing the Green's function. Here, we combine it with further simplification by manually identifying the relevant states for p-particle excitations. While it might seem cumbersome at first, the advantage of such a procedure is that it allows for the calculation of the *full* Green's function by evaluating Hamiltonian matrix elements on the basis of $\mathcal{K}^M$ and their derived states with singly ($p = 1$) and doubly ($p = 2$) excited particles in the bath chains. This essentially reduces the solution of a many-body problem H_{A} with a few hundred spin-orbitals to that of the much smaller subsystem H_{I}.

5.3.2 $p = 1$ PROJECTION

In the following, we derive the expression of the Hamiltonian and the Green's functions on the expanded subspace that includes single-electron (hole) excitations into the conduction (valence) chain. For simplicity, we assume a single-orbital model, as the generalization to multi-orbital case is straightforward. We further omit spin indices as the expressions are spin independent.

The expanded states with single-particle excitations in the bath chains can be obtained by acting with H_{A} on the initial subspace $\mathcal{H}_0' = \mathcal{H}_{\mathrm{I}}' \otimes |1_v\rangle \otimes |0_c\rangle$. As $\mathcal{H}_0'$ is closed with respect to H_0, the singly excited states are then generated by $V\mathcal{H}_0'$. Note that $\mathcal{H}_I'$ is still exponentially large for a sufficiently large L, in practice we approximate it by $\mathcal{K}^M$, which is known to provide an accurate representation for H_{I}. $\mathcal{H}_0'$ is then replaced by $\overline{\mathcal{H}}_0' = \mathrm{span}(|\psi_j\rangle = |\nu_j\rangle \otimes |1_v\rangle \otimes |0_c\rangle \, | j = 0, \ldots, K)$. The $p = 1$ expanded vector space $\mathcal{H}_1'$ is therefore approximately given as

$$\mathcal{H}_1' \approx \overline{\mathcal{H}}_1' = \mathrm{span}(\{\left|\psi_{jk}^e\right\rangle\}) + \mathrm{span}(\{\left|\psi_{jk}^h\right\rangle\}),$$

where

$$\begin{aligned} \left|\psi_{jk}^e\right\rangle &= t_c c_L \, |\nu_j\rangle \otimes |e_k\rangle = |\eta_j\rangle \otimes |e_k\rangle \,, \quad \text{and} \\ \left|\psi_{jk}^h\right\rangle &= t_v v_L^\dagger \, |\nu_j\rangle \otimes |h_k\rangle = |\zeta_j\rangle \otimes |h_k\rangle \,, \end{aligned}$$

where $|e_k\rangle = |1_v\rangle \otimes c_{L+k}^\dagger \, |0_c\rangle$ and $|h_k\rangle = v_{L+k} \, |1_v\rangle \otimes |0_c\rangle$ $(k \geq 1)$ are the single electron and hole states of the truncated bath chains. We have relabeled the fermionic operators on the conduction and valence sites by $c^{(\dagger)}$ and $v^{(\dagger)}$, respectively. V is now explicitly given as $V = t_c c_L^\dagger c_{L+1} + t_v v_L^\dagger v_{L+1} + \mathrm{H.c.}$, where $t_{c(v)}$ is the hopping between conduction (valence) bath sites L and $L+1$ (see Fig. 5.4). It is easily seen that $\overline{\mathcal{H}}_1'$ is orthogonal to $\overline{\mathcal{H}}_0'$. We can evaluate the matrix elements of $H_{\mathrm{A}} = H_0 + V$ on the $p \leq 1$ subspace as

$$\begin{aligned} \langle\psi_j| \, H_0 |\psi_k\rangle &= \langle\nu_j|H_I|\nu_k\rangle = H_{jk}^I \\ \langle\psi_{jk}^e| \, H_0 |\psi_{lm}^e\rangle &= \langle\eta_j|H_I|\eta_l\rangle \, \delta_{km} + \langle e_k|H_c|e_m\rangle \, \delta_{jl} \\ &= H_{jl}^{I\eta} \delta_{km} + H_{k,m}^c \delta_{jl} \\ \langle\psi_{jk}^h| \, H_0 |\psi_{lm}^h\rangle &= \langle\zeta_j|H_I|\zeta_l\rangle \, \delta_{km} + \langle h_k|H_v|h_m\rangle \, \delta_{jl} \\ &= H_{jl}^{I\eta} \delta_{km} + H_{km}^v \delta_{jl}. \end{aligned} \tag{5.18}$$

and

$$\begin{aligned} \langle\psi_j| \, V |\psi_{kl}^e\rangle &= \langle\eta_j|\eta_k\rangle \, \delta_{0l} = V_{jk}^\eta \delta_{0l} \\ \langle\psi_j| \, V \left|\psi_{kl}^h\right\rangle &= \langle\zeta_j|\zeta_k\rangle \, \delta_{0l} = V_{jk}^\zeta \delta_{0l}. \end{aligned} \tag{5.19}$$

Note that we have defined the ground-state energy to be zero. The elements of the

matrices $H^I(\equiv \overline{H}_I)$, H^c, and H^v are already known. One only needs to evaluate the (M-dimensional) matrices $H^{I\gamma}$ and V^γ ($\gamma = \eta, \zeta$), with the latter identified with the overlap matrix of $\{|\gamma\rangle\}$. Note that the states $\{|\psi_{jk}^{e(h)}\rangle\}$ are not orthonormal. To bring them into an orthonormal form, one can solve the generalized eigenvalue problem $H^{I\gamma}$ with respect to V^γ and obtain the eigenvector matrix T^γ. The above matrices are then expressed on the orthonormal basis set as $\tilde{H}^{I\gamma} = T^{\gamma\dagger} H^{I\gamma} T^\gamma$, which is the diagonal eigenvalue matrix, and $\tilde{V}^\gamma = V^\gamma T^\gamma$. The Green's function can then be calculated by inverting the full $H_{\rm A}$ defined on $\overline{\mathcal{H}}^1$.

5.3.3 $p = 2$ PROJECTION

We further relax the projection condition to allow double excitations. The full $p \leq 2$ subspace is given by $H_{\rm A}^2 \mathcal{H}_0' = \mathcal{H}_0' + \mathcal{H}_1' + V^2 \mathcal{H}_0'$. The $p = 2$ subspace $\mathcal{H}_2'$ is then spanned by the subset of doubly excited states in $V^2\mathcal{H}_0' = V\mathcal{H}_1'$. Similar to the $p = 1$ case, we approximate $\mathcal{H}_2' \approx \overline{\mathcal{H}}_2' = V\overline{\mathcal{H}}_1'$. Under such approximation, the states in $\overline{\mathcal{H}}_2'$ are given as

$$
\begin{aligned}
\psi_{jkl}^{e\uparrow e\downarrow} &= t_c^2 c_{L,\uparrow} c_{L,\downarrow} |\nu_j\rangle \otimes |e_{k\uparrow} e_{l\downarrow}\rangle = |\lambda_j\rangle \otimes |e_{k\uparrow} e_{l\downarrow}\rangle \\
\psi_{jkl}^{h\uparrow h\downarrow} &= t_v^2 v_{L,\uparrow}^\dagger v_{L,\downarrow}^\dagger |\nu_j\rangle \otimes |h_{k\uparrow} h_{l\downarrow}\rangle = |\mu_j\rangle \otimes |h_{k\uparrow} h_{l\downarrow}\rangle \\
\psi_{jkl}^{e\sigma h\sigma'} &= t_c t_v c_{L,\sigma} v_{L,\sigma'}^\dagger |\nu_j\rangle \otimes |e_{k\sigma} h_{l\sigma'}\rangle = |\theta_j\rangle \otimes |e_{k\sigma} h_{l\sigma'}\rangle
\end{aligned}
$$

which describe two-electron, two-hole, and electron-hole excitations into the bath chains. The spin indices are recovered here considering the Pauli principle. The Hamiltonian matrix elements for H_0 read

$$
\begin{aligned}
\langle \psi_{jkl}^{e\uparrow e\downarrow} | H_0 | \psi_{mno}^{e\uparrow e\downarrow} \rangle &= H_{jm}^{I\lambda} \delta_{kn} \delta_{lo} + H_{kn}^c \delta_{jm} \delta_{lo} + H_{lo}^c \delta_{jm} \delta_{kn} \\
\langle \psi_{jkl}^{e\sigma h\sigma'} | H_0 | \psi_{mno}^{e\sigma h\sigma'} \rangle &= H_{jm}^{I\theta} \delta_{kn} \delta_{lo} + H_{kn}^c \delta_{jm} \delta_{lo} + H_{lo}^v \delta_{jm} \delta_{kn},
\end{aligned}
\tag{5.20}
$$

with $H^{I\lambda}$ and $H^{I\theta}$ the Hamiltonian matrices evaluated on the basis set $\{|\lambda\rangle\}$ and $\{|\theta\rangle\}$. The matrix elements for V are given as

$$
\begin{aligned}
\langle \psi_{jk}^{e\uparrow} | V | \psi_{lmn}^{e\uparrow e\downarrow} \rangle &= \langle \theta_j | \theta_l \rangle \, \delta_{k,m} \delta_{0,n} = V_{jl}^\theta \delta_{k,m} \delta_{0,n} \\
\langle \psi_{jk}^{e\downarrow} | V | \psi_{lmn}^{e\uparrow e\downarrow} \rangle &= \langle \theta_j | \theta_l \rangle \, \delta_{k,m} \delta_{0,n} = V_{jl}^\theta \delta_{0,m} \delta_{k,n}.
\end{aligned}
\tag{5.21}
$$

Similar expressions can also be derived for the excited-hole states. Same as for the $p = 1$ case, the expanded states $\{|\lambda\rangle\}$, $\{|\mu\rangle\}$, $\{|\theta\rangle\}$ need to be orthonormalized.

Finally we emphasize that, as we approximate the electron addition/removal Hilbert space $\mathcal{H}_0'$ of the subsystem H_I by $\mathcal{K}^M$, the completeness of the $p = 1$ and $p = 2$ states depends on M and the results should be tested for convergence in M.

5.4 DMFT loop on real-axis

We now demonstrate an application of the natural-orbital solver presented above in the context of DMFT [111, 112]. Within DMFT, a Hubbard model is mapped onto a single-impurity Anderson model supplemented by a self-consistency condition that identifies the impurity Green's function with the local lattice one. The central ingredient of DMFT is thus the (iterative) calculation of the impurity Green's function. The steps for constructing the DMFT self-consistency loop entirely on the real-frequency for a general Hamiltonian can be found in e.g. Ref. [74, 98]. It should be noted that the prerequisite of such constructions is to include a sufficiently large number ($\mathcal{O}(10^2)$) of bath sites in the Hamiltonian (5.1), which is necessary for an accurate real-frequency representation of the bath Green's function.

In the following sections, we focus our discussion on the calculation of the one-band Hubbard model on the Bethe lattice with infinite coordination number, for which the DMFT mapping is exact. In addition, for benchmark purposes we assume spin-symmetric couplings and particle-hole symmetry, as there is abundant literature containing high quality results obtained from different numerical methods. In this case, the the DMFT loop can be greatly simplified, as the imaginary part of the bath hybridization function $\tilde{\Delta}(\omega) \equiv -\frac{1}{\pi}\operatorname{Im}\Delta(\omega) = \sum_l |V_l|^2 \delta(\omega - \epsilon_l)$ is related to the impurity spectral function $A_\mathrm{imp}(\omega) \equiv -\frac{1}{\pi}\operatorname{Im} G_\mathrm{imp}(\omega)$ as $\tilde{\Delta}(\omega) = \frac{D^2}{4} A_\mathrm{imp}(\omega)$, where D is the half-bandwidth of the semi-elliptic non-interacting density of states. The spin indices for the observables are omitted hereafter for the ease of notation.

Within each DMFT loop, the bath parameters are obtained by a discrete representation of the hybridization function over $N_l \sim \mathcal{O}(10^2)$ poles. We employ a scheme similar to Ref. [78] by discretizing the frequency-axis into N_l intervals $\{I_l\}$. Here we chose the intervals such that the weight V_l^2 is equal for each bath site. The impurity spectral function $A_\mathrm{imp}(\omega)$ is then obtained by solving the resulting impurity model with our solver described in in Sec. 5.1, which leads to an update of the hybridization

function

$$\tilde{\Delta}(\omega) = \frac{D^2}{4}\left[\alpha A'_{\mathrm{imp}}(\omega) + (1-\alpha)A_{\mathrm{imp}}(\omega)\right], \tag{5.22}$$

with $\alpha \in [0, 1)$ a mixing factor that allows for under-relaxation by mixing in the spectral function $A'_{\mathrm{imp}}(\omega)$ from the previous loop. The convergence is reached once $A_{\mathrm{imp}}(\omega) = A'_{\mathrm{imp}}(\omega)$.

5.5 Results

We note that while the natural-orbital representation and projection scheme in Sec. 5.1 can be readily implemented in existing ED solvers [74], we adopt the MPS-based DMRG method [90] here for computing the impurity ground state and Green's functions, which is expected to be more efficient for large L values considering the quasi one-dimensional geometry in Fig. 5.1(b). We use the zip-up method (see section 4.3) when multiplying a Hamiltonian to MPS [113] for generating the Krylov states. Note that due to the relatively small size of the subsystem H_{I}, the total truncated weight of the MPS in each Lanczos step can be kept well below 10^{-16}.

In the following, we present DMFT results obtained for the one-band Hubbard model on the Bethe lattice using the proposed projection method. The total number of bath sites is set to $N_l = 301$, with each bath chain of full length 150. The calculation is performed for interaction values U/D ranging from 1/16 to 16, including both the itinerant and atomic limits. Especially, we focus our discussion on three representative values $U/D = 1.0$, 2.0, and 4.0, which correspond to weakly-correlated metal, strongly-correlated metal, and Mott insulator ground states in DMFT, respectively [112].

5.5.1 Ground state convergence

We start by discussing the ground-state results for the different U values. Fig. 5.5(a) shows the number of electrons per spin-orbital on the first 10 conduction bath sites in the converged DMFT ground state. Note that this is identical to the hole occupation in the valence chain due to the particle-hole symmetry. In the metallic regime with U/D from 1/16 to 2, n_l on each site converges towards 0 with decreasing U values. This is expected as the natural orbitals are exact in the $U \to 0$ limit. For a given U, we

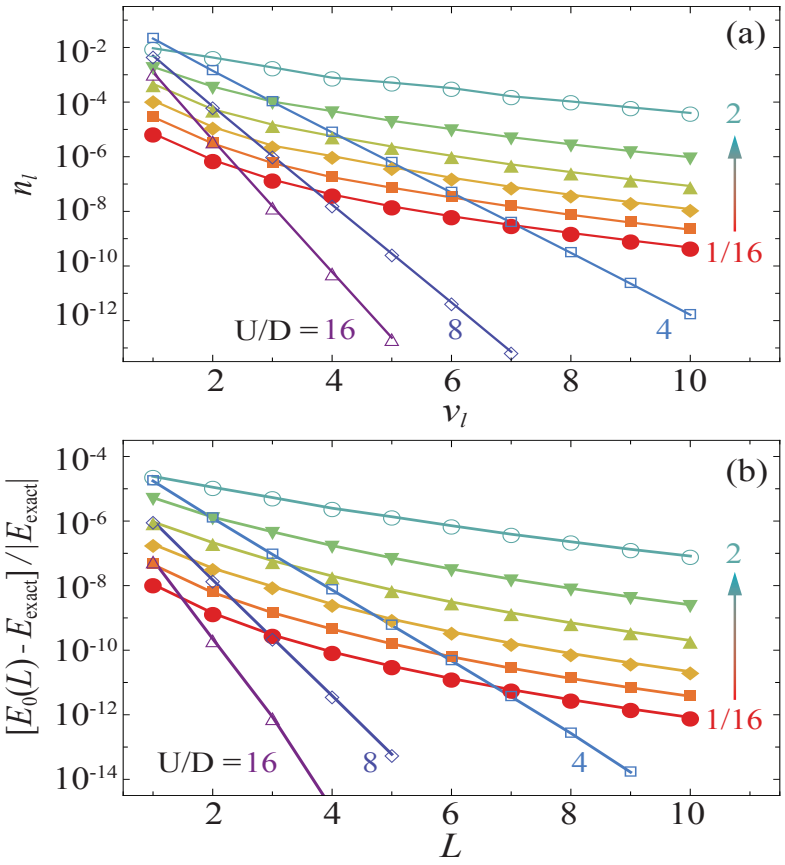

Figure 5.5: (a) Number of electrons per spin-orbital on the first 10 conduction bath sites in the converged DMFT ground state for U/D values ranging from $1/16$ to 16 as a geometric sequence with common ratio 2. The values are noted next to each curve. (b) Normalized ground-state energy deviation $[E_0(L) - E_{\rm exact}]/|E_{\rm exact}|$ as a function of L.

observe near-exponential decay of n_l with increasing site index l. Exact exponential decay of n_l is observed for the insulating cases with $U/D \geq 4$, as any particle-hole excitations into the bath chains is suppressed by the Mott gap of approximately $U - 2D$. The slowest convergence is observed for the correlated metals with $U/D \sim 2$, yet the electron density reaches below 10^{-3} within the first two to four bath sites for all the cases considered here. Closer inspection of the ground-state wave function reveals that even for the worst cases, states with completely empty conduction (filled valence) bath sites for $l \geq 2$ comprise more than 99% of the total weight, which justifies the proposed $p = 0$ projected wave function in Sec. 5.3 as a valid approximation for the exact ground state.

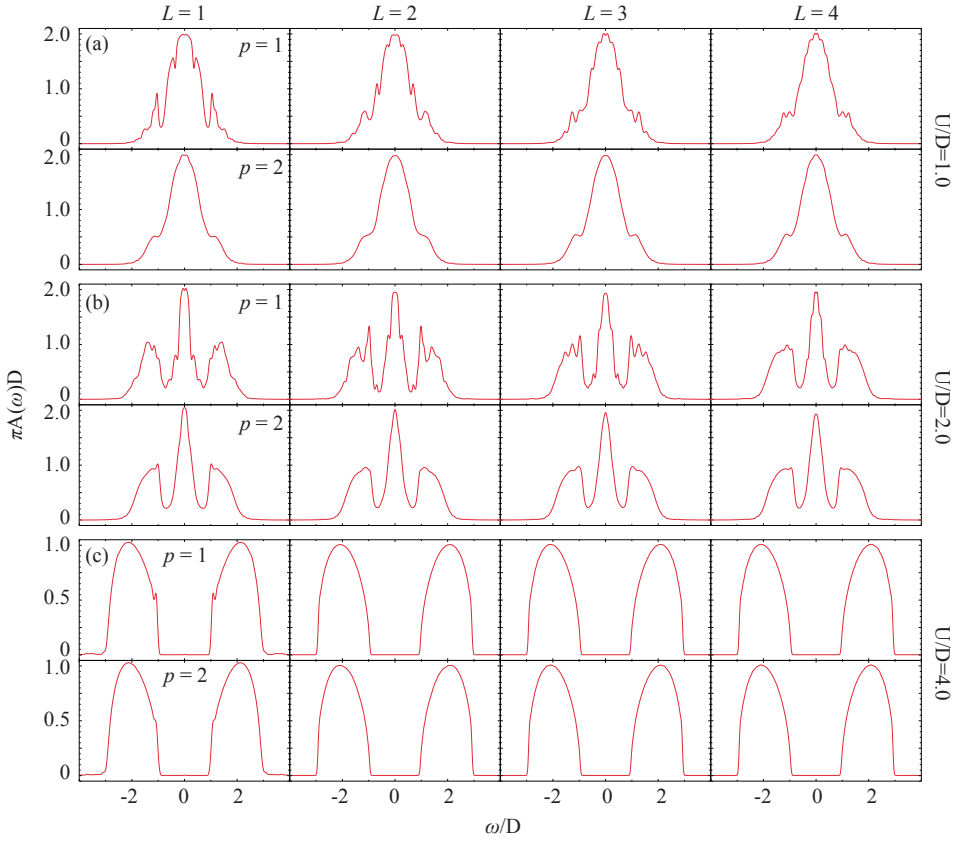

Figure 5.6: DMFT spectral functions for (a) $U/D = 1.0$, (b) $U/D = 2.0$, and (c) $U/D = 4.0$ calculated with different projection parameters (L, p).

Fig. 5.5(b) shows the relative error of the projected ground-state energy $E_0(L)$ (Eq. (5.13)) when applying projection at bond L between bath sites L and $L+1$ (see Fig. 5.4). As the energy deviation is directly correlated with the ground-state electron (hole) density in the conduction (valence) chains, one observes that $E_0(L)$ converges exponentially to the exact DMRG ground-state energy for the full system E_{exact}.

5.5.2 Green's Functions

We proceed to calculate the DMFT Green's functions with a few different sets of control parameters (L, p). The calculated spectral functions are presented in Fig. 5.6(a)–(c) for $U/D = 1.0$, 2.0, and 4.0, respectively. The spectra are convoluted with a

Gaussian kernel with full width at half maximum of $0.04D$.

The first row of each panel shows the spectral functions calculated with $p = 1$. Within each row, the results are presented for $L = 1$ on the left up to $L = 4$ on the right. For all U values, the spectra retain the general line shape of previous results [74, 95, 96]. This is best seen for the $U/D = 2.0$ case in Fig. 5.6(b), where the spectra show a sharp resonance at $\omega = 0$ and two broad Hubbard bands at approximately $\omega = \pm U/2$. Especially, the Luttinger pinning [114] at $\omega = 0$ with the condition $\pi D A(\omega = 0) = 2.0$ is fulfilled to a high accuracy for the metallic cases in Fig. 5.6(a) and (b). This suggests that the $p = 1$ projected states, i.e. those with only single-particle excitations in the bath sites, indeed capture the low-energy physics of the impurity model. On the other hand, we notice spurious oscillatory features/small peaks on the side of the quasiparticle peak or on the Hubbard bands, most noticeably for the metallic cases. As the amplitude of these features decreases with increasing L, they can be attributed partially to the missing of states with multi-particle excitations in bath sites close to the impurity site in the $p = 1$ projected subspace. We also note that for the insulating case in Fig. 5.6(c), there is some small residual weight (smaller than 10^{-4}) close to $\omega = 0$ for $L = 1$, which vanishes for $L \geq 2$.

The second row of each panel shows the spectral functions calculated with $p = 2$. Compared to the $p = 1$ results, the oscillatory features are greatly suppressed and smooth spectra are recovered for all U and (L, p) values. The results for $L = 3$ and 4 are in excellent agreement with previous results obtained using time evolving block decimation (TEBD) [96]. For the case of $U/D = 2.0$, two sharp side peaks can be observed at the inner edges of the Hubbard bands, in line with previous ED or DMRG results [74, 95, 96, 93]. We do note that the exact size of the side peaks is L dependent, and shows a converging behavior with increasing L similar to that of a Fourier spectral decomposition with increasing frequency cutoff. In Ref. [96] it was pointed out that the peak position and size are dependent on the system size (number of bath sites), and are likely related to the time-dependent probability of the impurity being doubly occupied. For the insulating case, we note that the change of $A(\omega)$ between the $p = 1$ and $p = 2$ results is less than 10^{-3} at all frequencies for $L \geq 2$.

Figure 5.8 shows the DMFT spectral functions obtained for $U/D = 1.0$ and 2.0 with $p = 2$ and $L = 2, 3, 4$. Compared to the quasi-exact results by solving the full impurity model [96], the key spectral features including the width of the quasi-particle

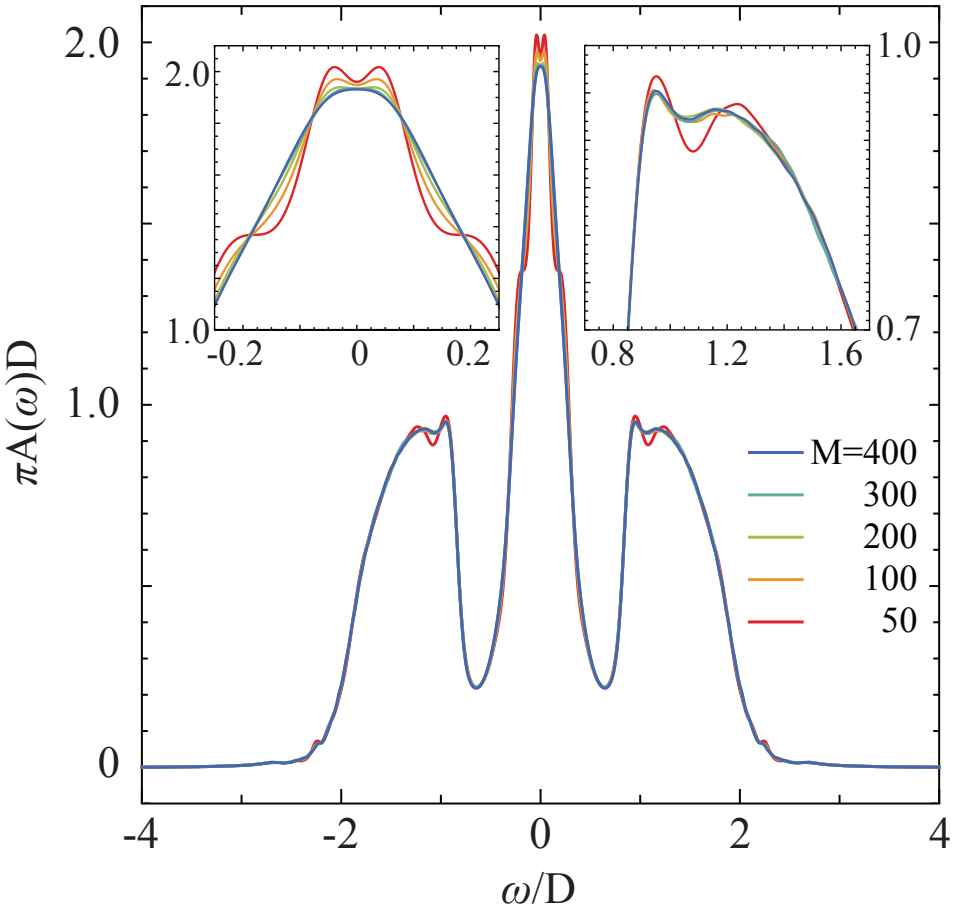

Figure 5.7: DMFT spectral function for $U/D = 2.0$ with different sizes of the initial Krylov space M. The insets show the detail of the quasiparticle peak and the Hubbard band.

peak and the size and position of the Hubbard bands are well reproduced already with $L = 2$.

As mentioned before, the convergence of the projected results depends on the size of the initial Krylov space M. Fig. 5.7 shows the DMFT spectral functions with $(L, p) = (4, 2)$ for $U/D = 2.0$ calculated with M ranging from 50 up to 400. The details of the quasiparticle peak and the upper Hubbard band are shown in the insets. For small M values, small oscillations are seen on the side of the quasiparticle peak, whose amplitude decreases with increasing M. The line shape becomes smooth and converges between $M = 300$ and 400. The size of the side peak on the Hubbard band is also seen to be M dependent, which becomes static for $M \geq 100$. For all spectra

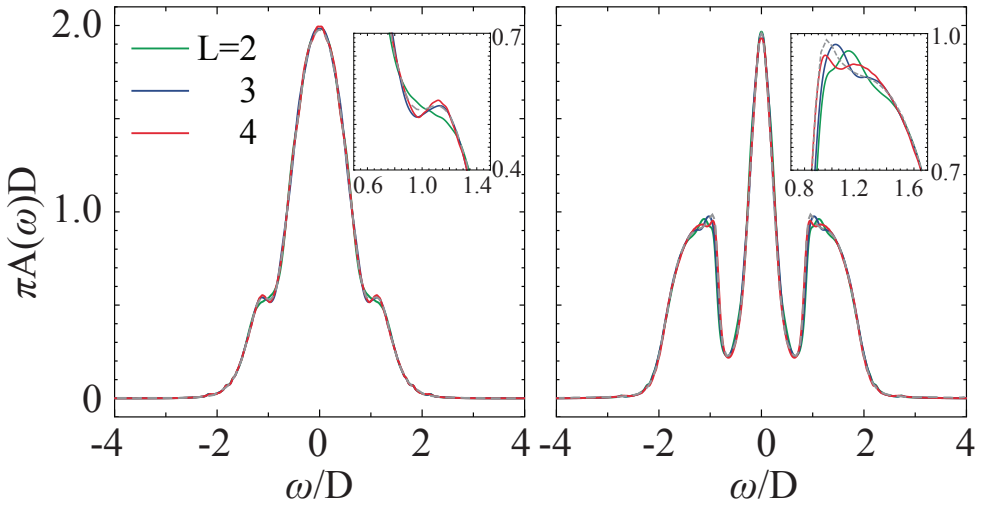

Figure 5.8: DMFT spectral functions for (a) $U/D = 1.0$ and (b) $U/D = 2.0$ for $L = 2$, 3, and 4 (solid lines), in comparison to results obtained by TEBD (dashed lines) reproduced from Fig. 1 in Ref. [96]. Note that the TEBD results are calculated with 119 bath sites.

shown in Fig. 5.6, their convergence in M is tested, which typically requires a value no more than a few hundred.

Finally, we comment on the computation cost of the proposed projection method. The most time-consuming part of the method is the generation of the initial Krylov space $\mathcal{K}^M$ and evaluating the Hamiltonian and overlap matrix element of the Krylov states as described in Sec. 5.3.1. The computation time then strongly depends on L and the size of the Krylov space M. For $(L, p) = (1, 2)$, calculating one $G(\omega)$ takes less than two minutes using a single CPU core (with $G^{\pm}(\omega)$ less than one minute each). The computation cost increases substantially with increasing L due to the increase of system size, and consequently the necessary increase of M. For the most challenging case of $U/D = 2.0$ and $(L, p) = (4, 2)$, calculating one $G(\omega)$ with $M = 300$ takes about two hours on a node with two eight-core processors (Intel Xeon E5-2630 v3, 2.40 GHz). However, as shown in Fig. 5.7, the spectral function calculated with $M = 100$ already closely resembles the converged result and correctly reproduces all the key features. It takes about twenty minutes to compute.

5.6 Conclusion

In conclusion, in this chapter, we have proposed a projection scheme for efficiently solving impurity models represented on a natural-orbital basis set. The natural-orbital representation and the projection scheme are generally applicable for fermionic impurity models regardless of number of orbitals or the form of interactions. We have shown that for a one-band Hubbard model solved within DMFT, accurate Green's functions can be calculated directly on the real frequency axes for all interaction strengths in the matter of minutes while including a few hundred bath sites. While the presented results are obtained within the DMRG framework using the Lanczos method, we expect the proposed method to work equally well with wave-function based techniques when calculating spectral functions, e.g. correction-vector method [115], dynamical DMRG [116], and various time-evolution methods [88] (see chapter 6). For multi-band problems, the exponential scaling of the computation cost with respect to the number of orbitals may still pose challenges for ED and MPS-DMRG with large L values. In chapter 7, by constructing the TTPS representation of the general multi-band impurity problems in the natural-orbital representation, an efficient and general-purpose impurity solver can be achieved.

6

Matrix Product States based impurity solver in time-domain

In the last chapter, we have introduced the projection framework for impurity systems on the frequency-axis. By separating the whole impurity Hamiltonian into three parts: including a small interacting subsystem which contains the impurity, a non-interacting bath part and the hybridization between these two parts, we can generate the Green's function of the full impurity problem from the one of the small interacting subsystem. This is achieved by expanding the Green's function of the small interacting subsystem w.r.t. the hybridization order in a successive non-perturbative manner. For the half-filling single-band Hubbard model on the Bethe lattice, an expansion to the second order is enough to converge the spectra to an acceptable accuracy. This corresponds to allow maximal 2 electrons (holes) in the projected conduction (valence) band. However, there are several potential pitfalls of this method:

- first, since the subsystem Green's function is calculated by the Krylov subspace method, it suffers from the fact that the high energy spectra can not be resolved accurately;
- second, it is tremendously difficult to extend the expansion to higher orders. The possible hopping terms from the impurity subsystem to the rest of the con-

duction or valence band grows quickly to intractable numbers as the expansion order is increased;

- third, it is not easy to extend this method to complicated multi-band systems. This difficulty originates from the facts that i) the MPS is not an efficient representation of the many-body wave function of a general multi-band impurity system (see next chapter); ii) the computation of the Krylov vectors poses a global change to the wave function conducted by the MPO-MPS operation, and, hence, results in a very quick growth of the MPS bond dimension.

In this chapter, we extend the projection framework to the time-domain which circumvents some of these difficulties encountered on the frequency-domain: the wave function is evolved locally and the expansion to higher order is straightforward. This chapter is organized as follows: In section 6.1, we introduce the projection framework in the time-domain; section 6.2 and 6.3 present discussions on the results of the single-band Anderson model and the DMFT solutions of the single-band Hubbard model on the Bethe lattice.

6.1 Particle number projection in the time-domain

In the previous chapter, we have established the advantage of the natural-orbital representation of the impurity model. In this section, we will make use of the natural-orbital representation and further introduce a particle number projection framework in the time-domain to improve the computation efficiency of computing the one-particle Green's function.

To compute the Green's function, after having already obtained the ground state $|0\rangle$ from DMRG, one needs to evolve the excited state to time t as $|\psi(t)\rangle = e^{\mp i\left(\hat{H}-E_0\right)t} d^{(\dagger)}|0\rangle$. Since the impurity Hamiltonian written in the natural-orbital basis might have long-range terms, the time-dependent variational principle (TDVP) [117, 118] is adapted in this thesis to evolve the state. The main idea of the TDVP method is to project the action of $\hat{H}$ to the tangent space of the MPS manifold by introducing a tangent space projector $\hat{P}_{T_{|\psi\rangle}}$. Here, besides $\hat{P}_{T_{|\psi\rangle}}$, following the same spirit of the projection framework on the frequency-domain presented in the last chapter, we further introduce an electron (a hole) number projector $\hat{P}^{c(v)}_{L,N_{e(h)}}$, which constrains the maximal number of electrons (holes) $N_{e(h)}$ allowed in the projected conduction

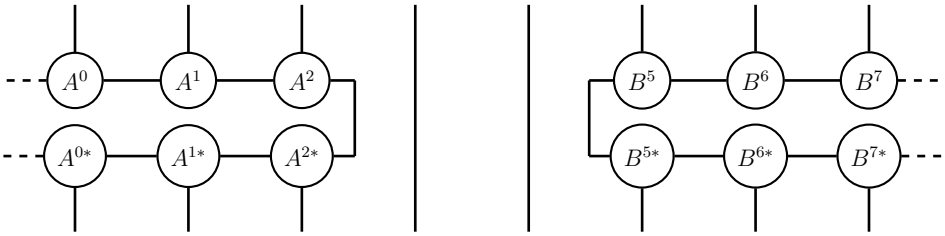

Figure 6.1: Graphic representation of the two-site tangent space projector acting on site 3 and 4. Here $A^i(B^i)$ represents the left- (right-) normalized MPS site tensor.

(valence) band. Here, L is the number of bath sites which are not subjected to occupation restrictions (see Fig. 5.4). Furthermore, in the rest of this thesis we will call the b site depicted in Fig. 5.4 as the "active" site and relabel it as a.

To allow a dynamical adjustment of the bond dimension during the time evolution, we will focus on the two-site variant of the TDVP algorithm. Together with the particle number projector, the time-dependent Schrödinger equation is now written as

$$\frac{d}{dt}|\psi(t)\rangle = -i\hat{P}^c_{L_c,N_e}\hat{P}^v_{L_v,N_h}\hat{P}_{T_{|\psi\rangle}}\hat{H}|\psi(t)\rangle. \tag{6.1}$$

The tangent space projector $\hat{P}_{|\psi\rangle}$ can be decomposed into

$$\begin{aligned}\hat{P}_{|\psi\rangle} = &\sum_{n=1}^{N-1} \hat{P}_L^{1:n-1} \otimes \hat{1}_n \otimes \hat{1}_{n+1} \otimes \hat{P}_R^{n+2:N} \\ &- \sum_{n=2}^{N-1} \hat{P}_L^{1:n-1} \otimes \hat{1}_n \otimes \hat{P}_R^{n+1:N},\end{aligned} \tag{6.2}$$

with a graphical representation of the first line as Fig. 6.1, while the second line can be represented in a similar way.

By acting $\hat{P}_{T_{|\psi\rangle}}$ on a MPS $|\psi\rangle$, the first sum contains all MPSs that differ at most on two nearest neighbor sites from $|\psi\rangle$, while the second sum removes all MPSs that differ at most on one site (except the first site) from $|\psi\rangle$. With such a decomposition of the tangent space projector, TDVP evolves $|\psi(t)\rangle$ at time t to $t + \Delta t$ by a successive left-to-right and right-to-left sweeping, which is similar to the standard two-site DMRG algorithm [118]. The difference is that, instead of solving a

local eigenvalue problem as in DMRG, in TDVP, one needs to solve the following local forward and backward problem, taking left-to-right sweeping as example (while right-to-left sweeping is similar),

$$\hat{X}_n\left(t+\frac{\Delta t}{2}\right)=\exp\left(-i\frac{\Delta t}{2}\hat{H}_n^{(2)}\right)\hat{X}_n\left(t\right), \tag{6.3}$$

$$\hat{M}^{\sigma_{n+1}}\left(t+\frac{\Delta t}{2}\right)=\exp\left(i\frac{\Delta t}{2}\hat{H}_{n+1}^{(1)}\right)\hat{M}^{\sigma_{n+1}}\left(t\right). \tag{6.4}$$

Here, $\left[\hat{X}_n\right]^{\sigma_n\sigma_{n+1}}_{b_{n-1}b_{n+1}}=\sum_{b_n}\hat{M}^{\sigma_n}_{b_{n-1}b_n}\hat{M}^{\sigma_{n+1}}_{b_nb_{n+1}}$ is the two-site wave function. The effective two- and one-site Hamiltonian $\hat{H}_n^{(2)}$ and $\hat{H}_n^{(1)}$ are constructed iteratively during the sweeping process by

$$\left[\hat{H}_n^{(2)}\right]^{\sigma_n\sigma_{n+1}b_{n-1}b_{n+1}}_{\sigma'_n\sigma'_{n+1}b'_{n-1}b'_{n+1}}= \tag{6.5}$$
$$\sum_{w_{n-1}w_nw_{n+1}}\hat{L}^{b'_{n-1}b_{n-1}}_{w_{n-1}}\hat{W}^{\sigma'_n\sigma_n}_{w_{n-1}w_n}\hat{W}^{\sigma'_{n+1}\sigma_{n+1}}_{w_nw_{n+1}}\hat{R}^{b'_{n+1}b_{n+1}}_{w_{n+1}},$$

and

$$\left[\hat{H}_n^{(1)}\right]^{\sigma_nb_{n-1}b_n}_{\sigma'_nb'_{n-1}b'_n}=\sum_{w_{n-1}w_n}\hat{L}^{b'_{n-1}b_{n-1}}_{w_{n-1}}\hat{W}^{\sigma'_n\sigma_n}_{w_{n-1}w_n}\hat{R}^{b'_nb_n}_{w_n}, \tag{6.6}$$

where L and R represent the left- and right-environment tensors satisfying the following recursive relations

$$\hat{L}^{b'_nb_n}_{w_n}=\sum_{b'_{n-1}b_{n-1}w_{n-1}}\hat{L}^{b'_{n-1}b_{n-1}}_{w_{n-1}}\hat{M}^{\dagger\sigma'_n}_{b'_{n-1}b'_n}\hat{W}^{\sigma'_n\sigma_n}_{w_{n-1}w_n}\hat{M}^{\sigma_n}_{b_{n-1}b_n}, \tag{6.7}$$

$$\hat{R}^{b'_{n-1}b_{n-1}}_{w_{n-1}}=\sum_{b'_nb_nw_n}\hat{R}^{b'_nb_n}_{w_n}\hat{M}^{\dagger\sigma'_n}_{b'_{n-1}b'_n}\hat{W}^{\sigma'_n\sigma_n}_{w_{n-1}w_n}\hat{M}^{\sigma_n}_{b_{n-1}b_n}, \tag{6.8}$$

with the boundary condition that $\hat{L}^{b'_0b_0}_{w_0}=\hat{R}^{b'_{N+1}b_{N+1}}_{w_{N+1}}=\mathbb{I}_3$ is a rank-3 identity tensor.

Equation (6.3) and (6.4) can be solved by the Krylov exponential solver to very high precision. Similar to the two-site DMRG, bond dimension of the MPS will increase along the time evolution. Hence, in order to suppress the growth of the bond dimension, after obtaining the new two-site wave function $\hat{X}_n$, a SVD factorization

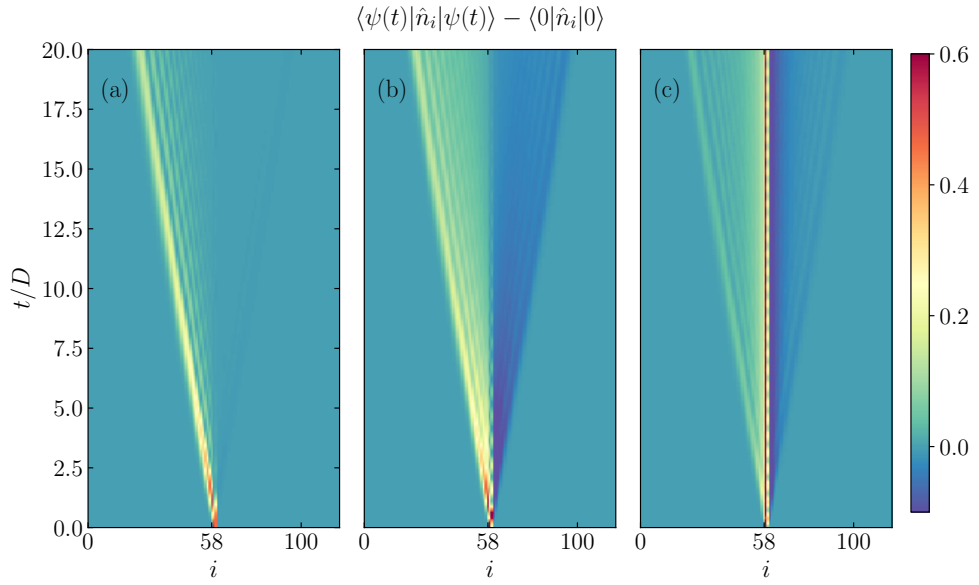

Figure 6.2: Density propagation through the system for different U values. From left to right panel, U is chosen as (a) $U = 0.25D$, (b) $U = 2D$ and (c) $U = 4D$. D is the half band width of the semi-elliptic density of states, and $N = 118$. The impurity/active site is located at $i = 58/59$.

and successive truncation of singular values w.r.t. a desired truncation weight t_w are usually performed. ***The effect of particle number projector is to restrict the maximal number of allowed electrons (holes) in the rest of the conduction (valence) band.*** One should note that, by increasing the allowed particle number ($N_{e(h)}$) or number of bath sites before the projection (L), we should be able to recover the pseudo-exact solution given by the TDVP (for the analysis of error introduced by TDVP, we refer to [117, 118, 119, 120]).

6.2 Application to the single-band Anderson impurity model

We start the discussions about the applicability of our projection framework by first studying the density propagation of the perturbed state $|\psi(t)\rangle = e^{-i\hat{H}t}d^\dagger|0\rangle$ with different U values. Although the leading velocity of the wave packets for different U values are approximately the same, the amplitude is slightly suppressed by increasing

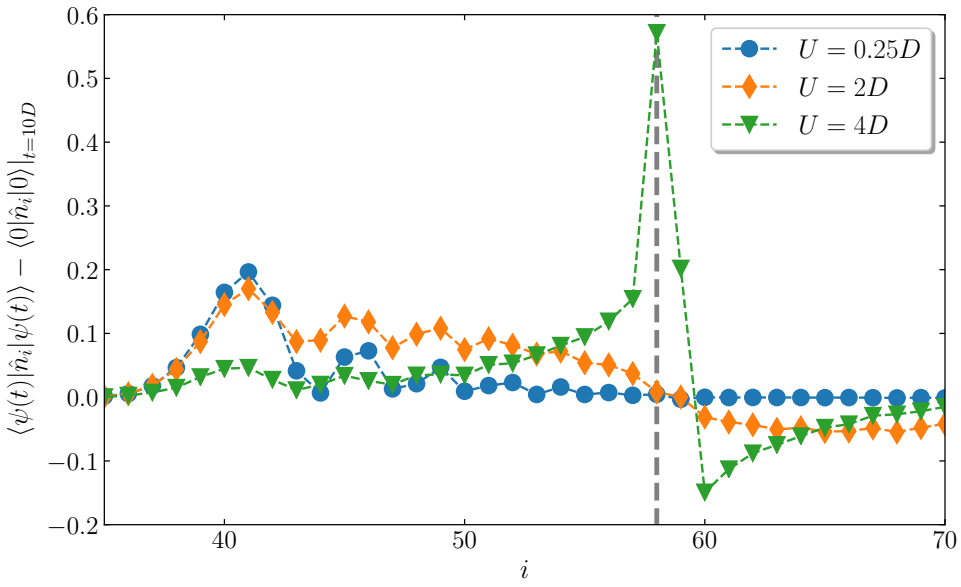

Figure 6.3: The snapshot of density propagation through the system at $t = 10D$ for $U = 0.25D$ (blue circle), $U = 2D$ (orange diamond) and $U = 4D$ (green down triangle). D is the half band width of the semi-elliptic density of states, and $N = 118$. The impurity site is located at $i = 58$ (indicated by the gray dashed line).

U from $0.25D$ to $2D$ and is strongly suppressed by further increasing U to $4D$ as shown in Fig. 6.2. Furthermore, for $U = 0.5D$ and $U = 2D$, the excitation on the impurity is more delocalized and keeps no residue for long times, while for $U = 4D$, it is more localized and leaves an almost constant residue on the impurity site. This behavior is connected with the formation of a Kondo singlet state between local moment on the impurity with moments on the bath sites (indicated by the Schrieffer-Wolff limit $U \sim 2D$), which is more clearly shown in Fig. 6.3 by a time snapshot of the density propagation.

After having gained some intuitive understanding on how the excitation propagates through the system, we move on to the analysis of the distribution of number of leaked electrons in the conduction bath sites of the perturbed states $|\psi(t)\rangle = e^{-i\hat{H}t}d^\dagger|0\rangle$. The ground state $|0\rangle$ is computed by the standard two-site DMRG with a truncation weight of $1e^{-10}$, and $|\psi(t)\rangle$ is evolved by two-site TDVP with a truncation weight of $1e^{-9}$. Fig. 6.4(a)-(c) show the weight of state $W_{N_e}(t)$ containing N_e electrons in the conduction bath sites as function of time for three interaction values $U = 0.25D$,

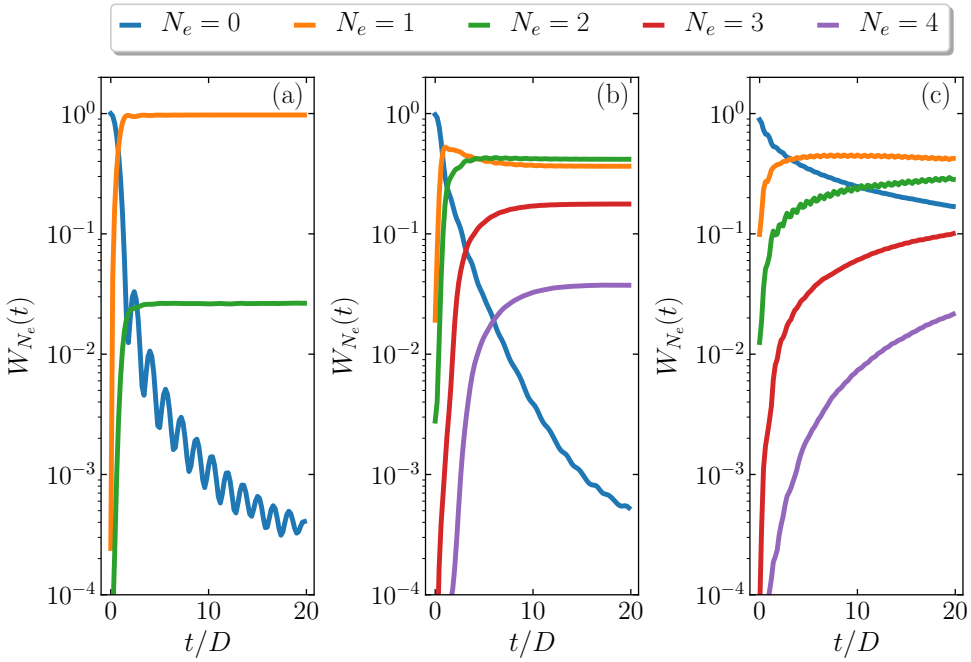

Figure 6.4: The weight of states with N_e electrons leaked into the conduction bath sites as functions of time for different U values. From left to right panel, U is chosen as $0.25D$, $2D$ and $4D$, respectively. D is the half band width of the semicircle density of states.

$U = 2D$ and $U = 4D$. At $t = 0$, $W_{N_e}(0)$ shows an exponential decrease for larger N_e values and, as the perturbation begins to propagate through the system, $W_{N_e}(t)$ with large N_e value begins to increase, while $W_0(t)$ decreases. However, states with small N_e values still dominate the dynamics of the system. For instance, when $U = 2D$, we have $W_0(t > 10D) + W_1(t > 10D) + W_2(t > 10D) = 0.38\% + 37\% + 42\% \approx 80\%$, and when $U = 0.25D$ we even have $W_1(t > 5) \approx 97\%$. Such a dominant contribution from small N_e values justifies that a truncation of the wave function with respect to the number of leaked electrons in the conduction bath sites can be well controlled. One should also note that, for the Anderson impurity model, by comparing $W_{N_e}(t)$ for different U values in Fig. 6.4, the truncation of states with respect to leaked electrons is more challenging for large U values. However, in DMFT large U values usually introduce a Mott charge gap in the spectra and suppress the leaking of electrons into the conduction band (and also holes into the valence band). This makes our projection framework more efficient.

One can expect that once going deeper into the conduction (valence) band (by

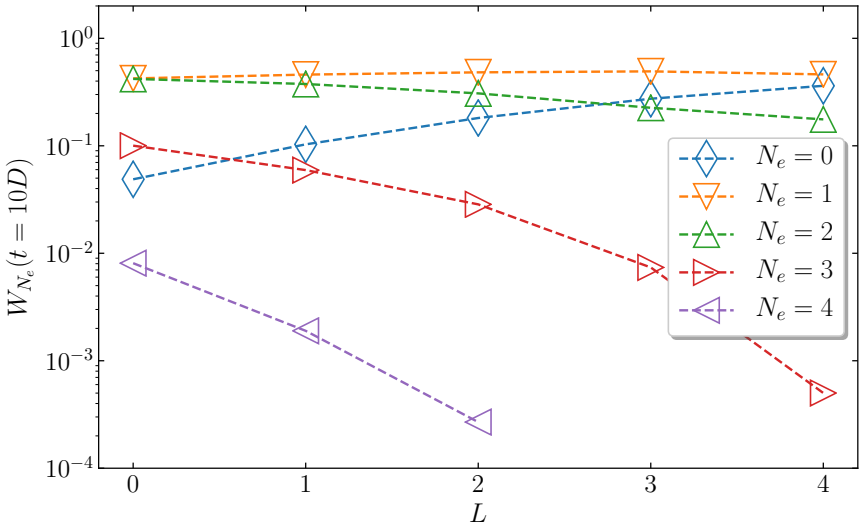

Figure 6.5: The weight of state having N_e electrons leaked into the conduction band as a function of the impurity subsystem size L. U is fixed to be $2D$.

increasing L), similar to the density profile of the ground state, contributions from the states containing higher leaked electrons (holes) to the total wave function $|\psi(t)\rangle$ will be further suppressed. This expectation is justified by the $W_{N_e}(t)$ distribution as function of L as shown in Fig. 6.5. We can clearly see that, when L is increased, $W_{N_e}(t)$ is suppressed for large N_e values ($N_e = 2, 3, 4$ in the plot) and increased for small N_e values ($N_e = 0, 1$ in the plot).

Finally, we turn to the single-particle Green's function and verify its convergence in L and $N_{e(h)}$. Here we fix the interaction strength as $U = 2D$ which represents a challenging case. Fig. 6.6(a) shows the real part of $G^{>}(t)$ calculated with different projection parameter combinations (L_e, L_h, N_e, N_h): with L_e (L_h) the number of free sites in the conduction (valence) band (ie., the unprojected region), and N_e (N_h) the allowed maximum number of electrons (holes) in the projected region. For $L_c = L_h = L = 1, N_e = N_h = N_f = 1$, the Green's function can be reliably computed only in a narrow short time region ($t < 2D$), while for the long time region, a large oscillation around the exact data is observed. Such an oscillating error can be understood from the following intuitive picture:once the excitation wave packet reaches the projector, only states with $[0, \cdots, N_{e(h)}]$ leaked electrons (holes) are allowed to continue to

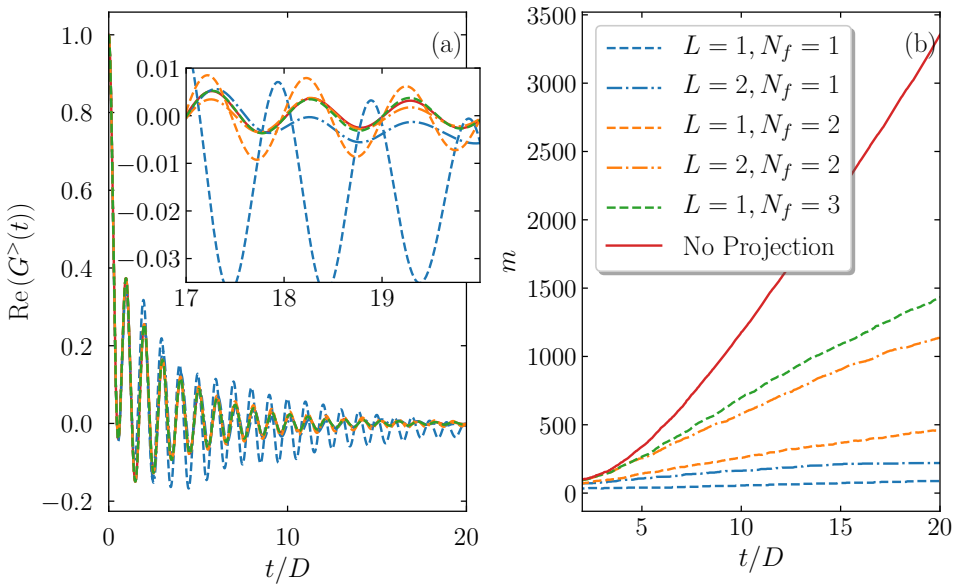

Figure 6.6: (a) Real part of the greater Green's function $G^{>}(t)$ with $U = 2D$ computed from different projection parameters: $L = 1, N_f = 1$ (green dashed); $L = 2, N_f = 1$ (green dash dotted); $L = 1, N_f = 2$ (blue dashed); $L = 2, N_f = 2$ (blue dash dotted) and $L = 1, N_f = 3$ (cyan dashed). As a reference, we also plot the data obtained without projection (red real). The insert shows an enlarged plot in the large time region. (b) the bond dimension between the impurity and the active site as a function of time for different projection parameters (same symbolism as (a)).

propagate, while states with larger number of leaked electrons (holes) are truncated. Hence, if L is too small to filter out the high energy excitations or the allowed leaked electrons (holes) number is too small, the excitation wave pocket will be blocked and form artificial bounded states located between the electron and hole projectors. As expected, when L or N_f is increased, the derivation to the exact result decreases exponentially as shown in the insert of Fig. 6.6(a).

To show the computational cost averted by our projection framework, we plot the bond dimension between the impurity and active site m (the largest one through the system) as a function of time in Fig. 6.6(b) for different (L, N_f) combinations. As a reference, we also plot the bond dimension for calculation without projection. We can see that, compared with the one without projection, the bond dimension of calculation with projection enjoys a much slower growth. Hence, our projection framework provides a systematic framework, which balances the desired accuracy and

computational cost, to compute the impurity Green's function.

6.3 Application to the single-band Hubbard model on the Bethe lattice

In the previous section, we have shown that the particle number projection method can be used as a well controlled method to achieve a balance between accuracy and efficiency for the Anderson impurity model. In this section, we further use it as the impurity solver for the DMFT solution of the single-band Hubbard model on the Bethe lattice at half-filling. During the self-consistent loop, the truncation weight for the DMRG search of the ground state is chosen as $1e^{-10}$, and $1e^{-9}$ for the TDVP time-evolution. A Lorentz kernel $\eta = 0.05D$ of the form $e^{i\omega t - \eta|t|}$ is used in the Fourier transformation from $G(t)$ to $G(\omega)$.

In Fig. 6.7, we show the spectral functions for three typical U values: $U = D$ corresponds to a weekly correlated metal; $U = 2D$ corresponds to a strongly correlated metal; $U = 4D$ corresponds to a Mott-insulator. In all interaction regions, we observe a fast convergence of the Green's function w.r.t. L and N_f by comparing with the quasi-exact TEBD data. Furthermore, even with $L = 1$ and $N_f = 1$, the main features of the spectral function are already revealed. For both $L = 1$ and $L = 2$, once we allowed more than 1 electron (hole) in the conduction (valence) band, the spectra is converged w.r.t. N_f.

6.4 Conclusion

In conclusion, we have extended the particle number projection framework formulated on the frequency-domain to the time-domain. This extension circumvents several shortcomings encountered in frequency-domain calculations: first, it is straightforward to take into account corrections to the Green's function from the higher order excitation processes; second, the excited state is evolved locally which contracts to the global changing of the state in frequency-domain. To justify the validity of the projection framework, we performed a comprehensive analysis of the density propagation process and particle number distribution during the time evolution of the impurity model. A fast decrease of the weight of states w.r.t. the number of leaked

electrons (holes) in the conduction (valence) band is observed. This guarantees the fast convergence of the projection method w.r.t. the size of the unprojected region and the number of the allowed leaked particles. Finally, this projection framework is used as an impurity solver for DMFT to solve the single-band Hubbard model on the Bethe lattice. The obtained Green's functions show a great agreement with the exact data and converges quickly as the projection parameters (L and N_f) are increased.

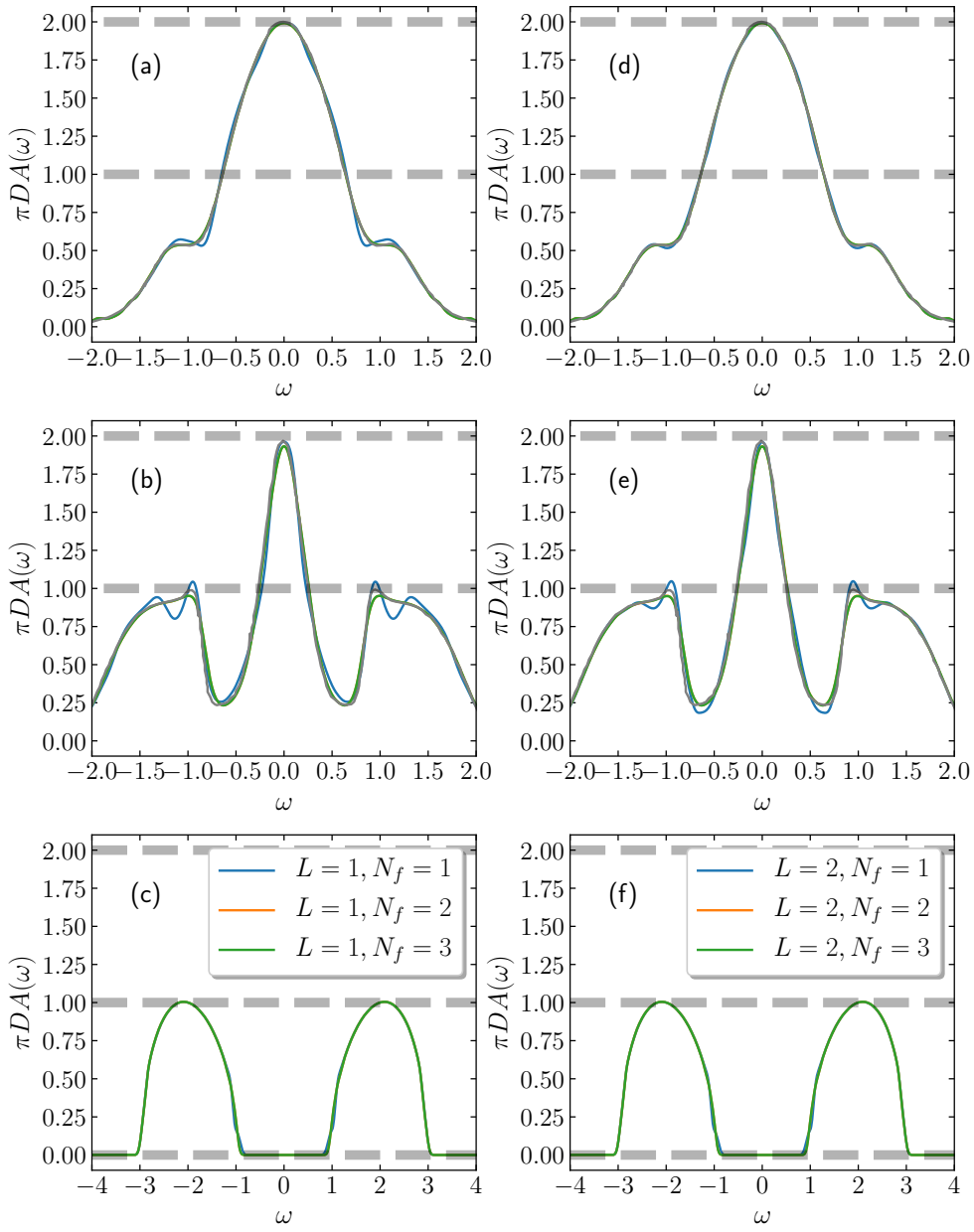

Figure 6.7: DMFT Spectral function of the single band Hubbard model on the Bethe lattice with different projection combinations and interaction strengths. (a) - (c) corresponds to $U = D, U = 2D, U = 4D$ with L being fixed to be $L = 1$ and N_f varying from 1 (blue line), 2 (orange line) and 3 (green line). (d) - (f) have the same parameters setting as (a) - (c) expect for $L = 2$. The gray real lines in (a), (b), (d) and (e) indicate the TEBD data taken from Ref. [96].

7

Tree Tensor Product states: an efficient multi-band impurity solver on the real-axis

Part of this chapter is presented in the preprint
"Efficient real-aixs tree tensor product states impurity solver in the natural-orbital basis", **Xiaodong Cao**, Yi Lu, Philipp Hansmann and Maurits W. Haverkort, ***in preparation***

In the last two chapters, the single band Hubbard model is solved within the DMFT approximation with a MPS based impurity solver that combines the rotation to the natural-orbital basis and the particle-number projection performed either on the frequency- or time-domain. However, the chain geometry of the MPS is best suited for quasi one-dimensional systems [90], hence its applications to impurity problems are limited on single- and two-band cases [96][97] for real-axis calculations. Although the MPS based impurity solver has been successfully used to solve the three-band model [94] on the imaginary-axis, the over fitting of the hybridization function and the ill-conditioned analytical continuation process put a limitation on its accuracy.

In this chapter, by first analyzing the disadvantage of using the MPS to solve multi-band impurity systems, we propose a tree tensor product state (TTPS) which is able to encode the complicated entanglement structures of multi-band impurity

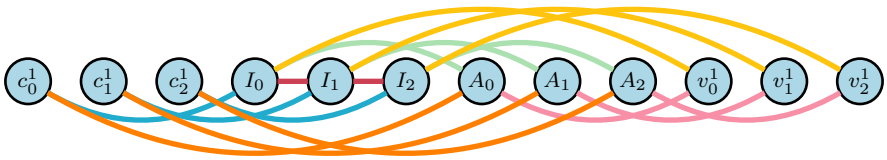

Figure 7.1: Placing the impurity and bath sites of a three-band model on the chain geometry in the interaction dominated way. Here I_i stands for the $i-$th impurity site, and A_i stands for the $i-$th active site. $c_i^j(v_i^j)$ stands for the $j-$th conduction (valence) bath site of the $i-$th orbital. The red lines represent the intra-impurity interactions, while the green, yellow, blue, orange and pink lines correspond to the hopping terms between the impurity and active sites, impurity and valence sites, impurity and conduction sites, active and conduction sites and active and valence sites.

systems in a more efficient way. Then, the key algorithms of TTPS are presented and their computational costs and potential pitfalls are discussed. Finally, we present the discussions on the application to $SrVO_3$ and further potential applications.

7.1 Modeling multi-band impurity systems with tensor product states

The intrinsic difficulty of using MPS to solve multi-orbital models can be illustrated as follows: when we place the impurity and bath sites in an "interaction" dominated way (illustrated in Fig 7.1), the entanglement between the impurity sites of different bands can be very large because of the inter-band interactions. However, as already indicated in the single-band system, the entanglement between the impurity and active site can be also very large. Since the entanglement between two sites is transferred through the auxiliary degrees of freedom living on the bonds that connect them, bond dimensions of the bonds that connect the impurity and active site belonging to the same band (e.g., I_0 and A_0 in Fig. 7.1) can be very large and make the calculation infeasible. One can also choose to place the impurity and active site belonging to the same band together. With such an ordering, however, the entanglement generated by the inter-band interactions will again increase bond dimensions of the bonds that connect the separated impurity sites.

In order to optimize the overall entanglement of the system, one can, in principle,

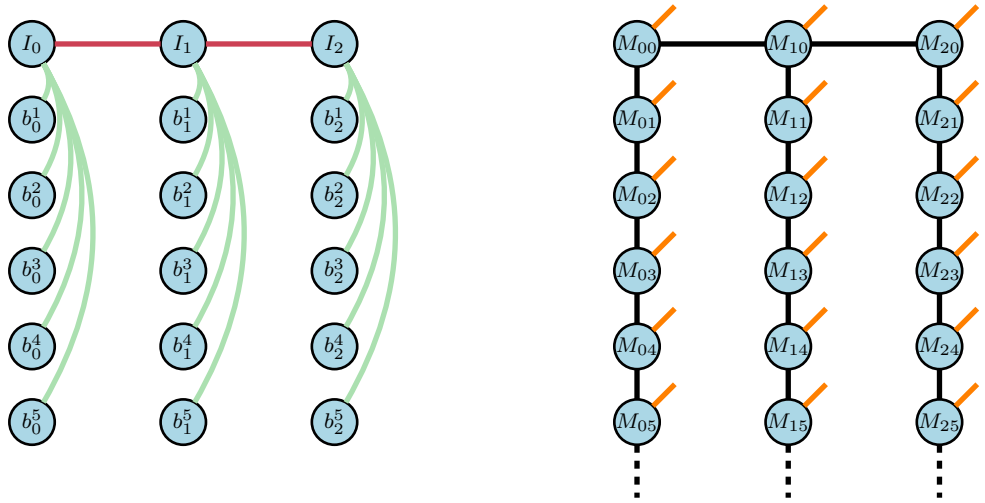

Figure 7.2: (left) Fork geometry for a three-band impurity model. Here I_i stands for the $i-$th impurity, b_i^j stands for the $j-$th bath site of the $i-$th band. The red lines connecting two impurity sites represent the interaction between them, and the green lines connecting the impurity and bath sites represent the hopping terms between them. (b) The fork tensor product states. Here, except site I_1, each site has a rank-3 tensor with two bond legs (black) and one physical leg (orange). The dashed lines at the edges of the fork represent the dummy bond legs. On site I_1, there is a rank-4 site tensor M_{10} with three bond legs and one physical leg. The indices of M_{ij} have the meaning that the $i-$th branch and $j-$th steps into the fork.

use the mutual-information [121] to reorder the sites. Because of the chain geometry of the MPS, however, the average distance between two arbitrary sites will increase linearly w.r.t. the total number of sites N. Hence, for typical DMFT calculations on the real-axis which need a large number of bath sites ($\sim 100 - 1000$) for a reasonable resolution of the spectra, the MPS has a very bad scaling to the number of bands (similar to the application of the MPS to quasi one-dimensional systems, in which the computational cost increases exponentially with the width of the sample).

In conclusion, the main disadvantage of the MPS for multi-band systems is the mixing of degrees of freedom that belong to different bands. Hence, if sites belonging to different bands are placed into separated chains and these chains are connected only through the impurity sites, we can achieve a geometry that optimizes both entanglement between the different impurity sites and entanglement between the impurity and bath sites belonging to the same band. This is the key idea behind the so called fork tensor product states (FTPS) [98] which is illustrate in Fig. 7.2.

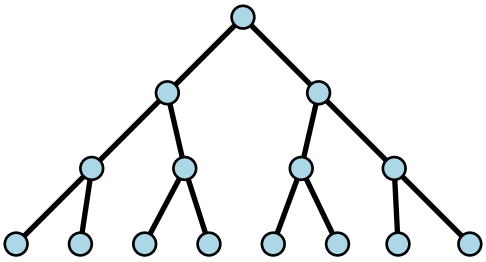

Figure 7.3: A depth 3 binary tree geometry. Each node can have two child nodes and one parent node.

In this tensor-network state, each site has a rank−3 site tensor M_{ij} (i represents the branch index and j represents the steps into that branch), with two bond legs and one physical leg, except the impurity sites having two impurity neighbors (I_1 for the three-band model depicted in Fig. 7.2) which have three bond legs and one physical leg. Such an explicit separation of bath degrees of freedom of different bands in the fork geometry assures that there is no intermediate auxiliary bonds between the impurity sites and each impurity site is connected with its bath sites directly, hence, it provides a better representation of the entanglement structure for multi-band systems. However, as discussed in the last chapter, the star geometry ordering of the bath sites within the same band does not provide the best one-particle basis set that minimizes the overall entanglement. The natural-orbital basis provides a better one-particle basis for the impurity problem.

One should note that, the FTPS is a specific case of the more general tree tensor product state [122]. In Fig. 7.3, we plot a binary tree geometry with depth $\Delta = 3$. In this geometry, each node can have two child nodes (a and b) and a parent node (r). One of the most important properties of the tree geometry with coordinate number z and depth Δ is that, the distance between two arbitrary sites scales **logarithmically** with the total number of sites N, which differs from the linear scale of the chain geometry. This can be understood from the fact that the largest distance between two sites in a general tree geometry with coordinate number z is 2Δ, and we also have

$$N = 1 + \sum_{i=1}^{\Delta} (z-1)^j = \frac{(z-1)^{\Delta+1} - 1}{z-2}. \tag{7.1}$$

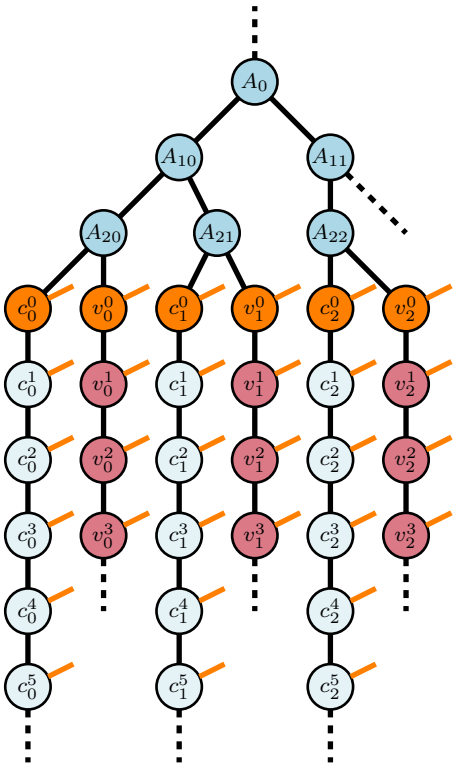

Figure 7.4: Sketch of the proposed tree tensor product states for a three-band impurity model. Here, A_{ij} represents the auxiliary rank-3 tensor which locates at the $i-$th depths from the root and $j-$th branch in that depth level. c_i^j represents the $j-$th conduction bath site of the $i-$th impurity, and v_i^j represents the $j-$th valence bath site of the $i-$th impurity. Here, we use a light cyan (red) color to indicate that the filling on the conduction (valence) bath sites are almost empty (full). The orange and black legs represent the physical and bond legs, and the black dashed ones represent the dummy bond legs.

Such a logarithmic scaling promotes tensor-network states based on tree geometry to be able to capture more complicated entanglement structures than MPS and FTPS.

Inspired by the above considerations, we propose the following tree tensor product states for general multi-orbital systems: for impurity systems with N_o orbitals, we use $2N_o$ non branching fork to represent their conduction- and valence bands separately. These non branching forks are connected by auxiliary rank-3 tensors. A sketch of this tensor product states for $N_o = 3$ is presented in Fig. 7.4. In this proposed tensor product states, we have a rank-3 tensor (two bond legs and one physical leg) on each of the physical impurity and bath sites. Conduction and valence channels belonging to the same band are first connected by an auxiliary rank-3 tensor with three band

legs (A_{20} connects c_0^0 and v_0^0). Then degrees of freedom belonging to different bands are connected by auxiliary rank-3 tensors with three bond legs of higher hierarchy in the tree (A_{10} connects A_{20} and A_{21}). The main benefit of the TTPS is that, additional to the separation of degrees of freedom belonging to different bands as achieved also in the FTPS, this network has a further explicit separation of degrees of freedom within the same band into a conduction and valence channel by the rotation into the natural-orbital basis. Once rotated into the natural-orbital basis, the filling of bath sites on the conduction channel are almost empty and decrease exponentially to zero with the distance to the impurity site. And the filling of the bath sites in the valence channel are almost full and show an exponential convergence to 2 with the distance to the active site. With such a fast converged density distribution we might expect that the most entangled sites are located close to the last branching auxiliary tensors (A_{20}, A_{21} and A_{22} in Fig. 7.4). Hence, the proposed TTPS captures the correct entanglement structure of a general multi-band impurity model, i.e., the strongly entangled sites are connected with an optimized minimal distance. Another benefit of TTPS is that, since it separates the conduction and valence channel explicitly, we can resolve the spectral function in an optimized way: we can assign the number of bath sites for the conduction and valence channel according to the filling of this band. For the $SrVO_3$ case which has a filling of one electron occupying three bands, giving 100 total bath sites for each band, we can assign 16 bath sites to the valence channel and 84 bath sites to the conduction channel.

7.2 Tree Tensor Product states

The basic ingredient of the proposed TTPS, or more general binary tree tensor product states, is the rank-4 site tensor $M^{i_p}_{i_r i_a i_b}$ living on each node, which can be graphically represented as:

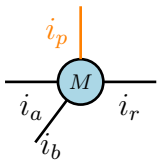

,

where i_r, i_a, i_b is the root, a-child and b-child bond leg, respectively, and i_p is the physical leg which forms a complete basis set for the local Hilbert space. For a

Hubbard site, the physical leg has a dimension of $d = 4$ ($i_p \in \{|0\rangle, |\uparrow\rangle, |\downarrow\rangle, |\uparrow\downarrow\rangle\}$). In our proposed TTPS, the auxiliary rank-3 tensors can be generated by simply setting the physical leg to be a dummy vacuum leg, while the rank-3 site tensors living on the impurity and bath sites can be generated by setting i_b to be a dummy vacuum leg. By working on the general rank-4 tensors, or equivalently, on the binary tree geometry, we can further branch the conduction and valence channels in our current network for future applications. Similar to MPS, we can also encode the symmetry information of the underlying systems into the site tensors. Currently, we have implemented the abelian $U(1)$ symmetry, the non-abelian $SU(2)$ symmetry is left for future study.

With the properly constructed site tensors on a tree geometry, the many-body wave function can be constructed as:

$$|\psi\rangle = \sum_{\{\sigma_i\}} \mathrm{tr}\Big\{\{M^{i_p}_{i_r i_a i_b}\}\Big\}|\sigma_0 \cdots \sigma_{L-1}\rangle. \tag{7.2}$$

Here, the trace operator tr{ } means that all the connected bond legs in the tensor-network are contracted. For a system of L sites, different from the Ldm^2 scaling in the MPS, the number of parameters used in the TTPS now has a cubic scaling as Ldm^3 w.r.t. the bond dimension m. The allowed maximal bond dimension m determines how much entanglement can be encoded in the TTPS. When $m \to \infty$, we recover an exact representation of the many-body wave function.

For the MPS, we can bring the state into a left-/right-normalized form by performing the SVD to its site tensors recursively by starting from the leftmost/rightmost site. Similarly, we can bring the TTPS into a root-normalized form by starting from the leafs of the TTPS (the bottom nodes), and moving upwards until the root node (top most node) of this network with the following operation to each site tensor M:

U is reshaped to the rank-4 site tensor A satisfying $\sum_{i_p i_a i_b} A^{i_p}_{i_r (i_a i_b)} A^{\dagger i_p}_{(i_a i_b) i_{r'}} = \delta_{i_{r'} i_r}$. $S \cdot V$ is transferred to its root site tensor. Here the hermitian operator acts on the root index i_r and the combined index $(i_a i_b)$.

The bipartite nature (i.e., any cut of the bond legs connecting two sites will separate the network into two disconnected parts) of the TTPS makes it possible to extend the efficient DMRG algorithm for ground state optimization and TDVP algorithm for time evolution developed for the MPS to TTPS. In the following, we will elaborate on such extensions and analyze the performance of these algorithms.

7.3 Compression of TTPS

Similar to the MPS, TTPS does not form a complete vector space neither. Addition of two TTPSs of bond dimension m_1 and m_2 will result in a TTPS of bond dimension $m_1 + m_2$. Also, by applying a general operator represented by the tree tensor product operator (TTPO) on the TTPS , its bond dimension will increase inevitably. As the most straightforward compression method, here we present the SVD compression algorithm for TTPS.

In the SVD-compression of a MPS, we first perform a right-to-left sweep without truncating the singular values to bring the MPS into a right-normalized form, then a successive left-to-right sweep with the desired truncation accuracy is performed. This guarantees that when the SVD is performed to a site tensor, its left site tensors are all left-normalized and right site tensors are all right-normalized, during the final left-to-right truncating sweep. In other words, we have constructed a left- and right-orthonormalized basis set for this site tensor. In the TTPS, since each site tensor has three bond legs, it is a bit more complicated to perform the SVD compression properly, i.e., when a SVD truncation is performed to a specific bond leg, we must ensure that the other two bond legs are in the properly normalized form or equivalently forming a proper orthonormalized basis set. To achieve this, we perform the SVD truncation in the following recursive way: starting from the top most node, for each node tensor, we first bring its b-child sub-tree into root-normalized form without truncating the singular values followed by an a-normalization of the current node tensor also without truncation of the singular values. Then, we descent into the a-child sub-tree and perform the same procedure to truncate it. After the a-child sub-tree is properly truncated, an a-normalization of the current site tensor followed by a root-normalization to its a-child site tensor are conducted with the desired truncation accuracy. Then, we descent into the b-child sub-tree and perform the SVD compression to it with the same recursive procedure as done for the a-child sub-tree.

Finally, this site tensor is brought into r-normalized form with the desired truncation accuracy. Such a truncation process ensures that each bond leg is truncated in both directions. For a bond connecting an a-child site tensor and its parent tensor, e.g., it is truncated first by a r-normalization followed by an a-normalization of its parent node tensor and finally by another r-normalization.

The recursive visiting of nodes in the tree network presented above is frequently used in the TTPS related algorithms. To demonstrate how this visiting procedure works, let's use the TTPS presented in Fig. 7.4 as an example: we start from node A_0, then the site tensors are visited in the following sequence: $A_0 \xrightarrow{a} A_{10} \xrightarrow{a} \cdots \xrightarrow{a} c_0^0 \xrightarrow{a} \cdots \xrightarrow{a} c_0^5 \xrightarrow{r} \cdots \xrightarrow{r} c_0^0 \xrightarrow{r} A_{20} \xrightarrow{b} v_0^0 \xrightarrow{a} \cdots \xrightarrow{a} v_0^3 \xrightarrow{r} \cdots \xrightarrow{r} v_0^0 \xrightarrow{r} A_{20} \xrightarrow{r} A_{10} \xrightarrow{b} A_{21} \cdots$ (visiting the second band) $\cdots$ (visiting the third band) $\cdots A_{11} \xrightarrow{r} A_0$. Here the superscript of each arrow indicates how this bond leg is normalized (a, b and r stands for a-, b- and r-normalized respectively). Hence, we visit the site tensors by going along the edge of the tree in an counter-clockwise direction.

7.4 Overlap and expectation value of two TTPS

To compute the overlap between two TTPSs $\langle\psi_2|\psi_1\rangle$, we contract the tensor network recursively as:starting from the leafs of the tree network, for each node, we first check that whether it has an a-child or not. If it has one, we construct the a-environment tensor E_a for it, and if not we use an identity rank-2 tensor as the a-environment tensor; after the a-environment tensor has been constructed, the b-environment tensor E_b is constructed in the same way. Finally, the new a- or b-environment tensor (depending on whether the current node is an a-child or b-child to its root node) is constructed as:

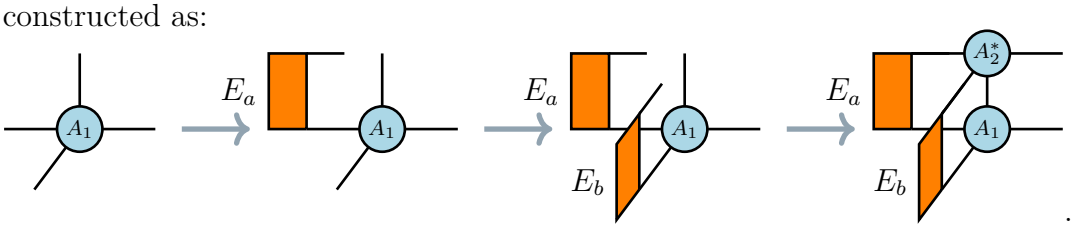

Once the many-body operator and state are represented by the TTPO and TTPS, we can compute the expectation value of any operator overlapped by two states $\langle\psi_2|\hat{O}|\psi_1\rangle$ in a recursive way which is similar to the one used for the evolution of the

overlap value as presented above. For a node that does not have an a- or b-child, a rank−3 split tensor is used as the initial environment tensor, instead of an identity rank−2 tensor. This split tensor is constructed by using the operator and state child legs as the two outgoing legs. The new environment tensor is constructed as:

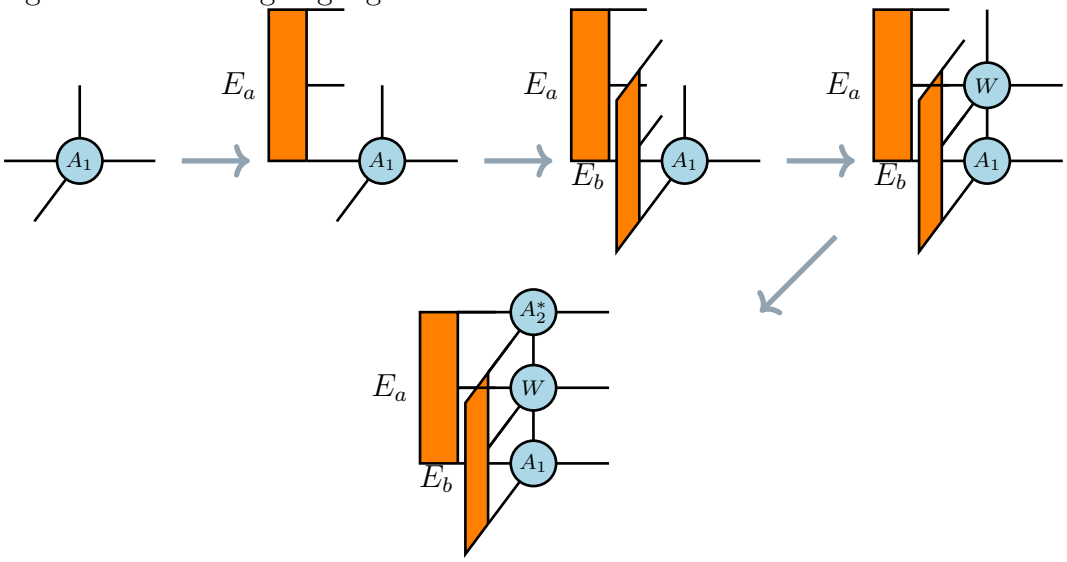

Noting that, the contraction order is that we first contract the site tensor A_1 with the two environment tensors E_a and E_b successively, then the resultant rank−6 tensor is contracted with the operator site tensor W followed by a final contraction with $A_2^\dagger$. The total computational cost will be $\sim m \cdot (wm \cdot dm^2) + m \cdot (wm \cdot dm \cdot wm) + dm^2 \cdot (m^3 \cdot wd) + dm^2 \cdot (wm^2)$, with a leading order of $\sim m^5$.

7.5 Applying the TTPO on TTPS: the zip-up Algorithm

The zip-up algorithm proposed for the MPS approximates the new state resulting from applying a general operator on a given state has been shown to be very efficient and accurate. In our impurity solver implementation on the frequency-domain, it is used as the key algorithm to generate the Krylov subspace for the excited states. To extend it to the TTPS, we follow the same strategy as applied in the MPS: we first bring the TTPS into a r-normalized form without truncating it. Next, by starting from the root node, each site tensor is updated as follows: if the node has a root node, then the tensor on its root node is brought into the correct normalized form, i.e., if

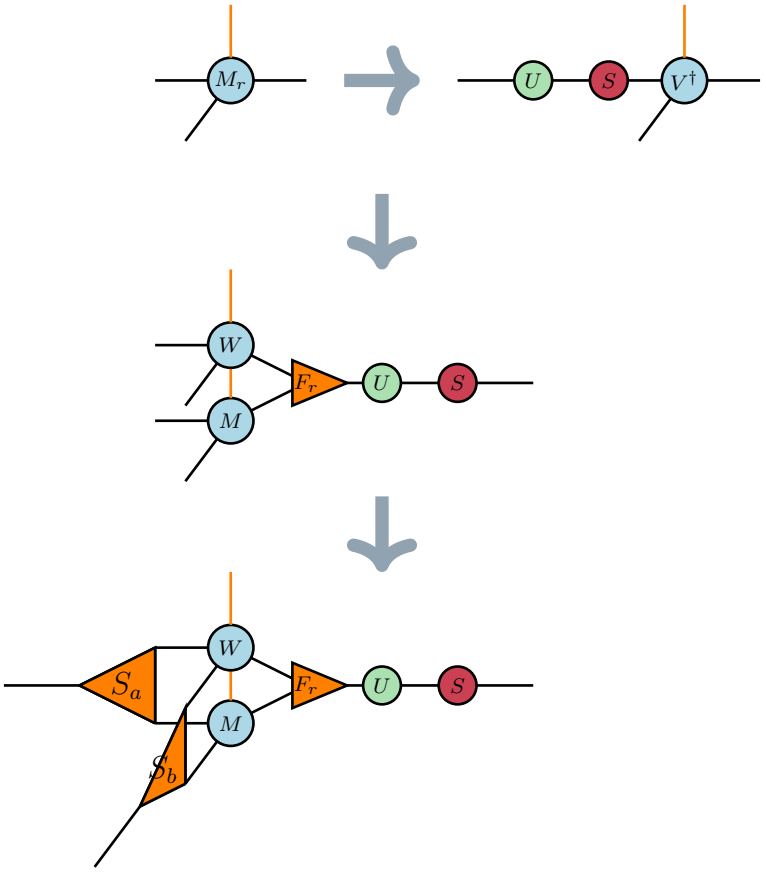

Figure 7.5: Local update of the site tensor in the zip-up algorithm. Here, F_r represents the rank-3 fusing tensor, and $S_{a,b}$ represents the rank-3 a-/b-child splitting tensor, respectively.

this node is an a(b)-child, then the tensor on its r-node is a(b)-normalized. Then, the tensor on the current node is updated as depicted in Fig. 7.5. After the local update, we descent into its a-child and b-child sub-tree (if they exist), and update them recursively. Once its a- and b-child sub-tree are both updated, the site tensor is brought into root-normalized form. Note that, up to now, all the normalization operations are performed with a relaxed truncation threshold. Finally, the updated TTPS is truncated with the desired accuracy by a overall root-normalization. This procedure is summarized in Algorithm. 1.

Algorithm `zipUpAlgo()`

Input: TTPS $|\psi\rangle$, **TTPO** $\hat{O}$, **Truncation Thresholds** trunc

`/* root normalize the state without truncation */`

root-normalize the input state $|\psi\rangle$ without truncating it

`/* relax the truncation thresholds */`

truncR = relaxed truncation thresholds of trunc

`/* apply the TTPO onto` $|\psi\rangle$ `with a relaxed truncation threshold, typically, the bond dimension is twice enlarged. The recursive routine starts from the root node of the input state. */`

error + = `zipUpRec(`$|\psi\rangle$,$|\psi\rangle$*.r,* $\hat{O}$*.r, truncR*`)`

error + = truncating $|\psi\rangle$ with trunc

return *error*

Procedure `zipUpRec(`$|\psi\rangle$, aptr, optr, iLeg, trunc`)`

`/* recursive routine for zip-up algorithm */`

error $\leftarrow$ 0

if *aptr has a-child* **then**

  error + = `zipUpSite(`*aptr, optr, iLeg, trunc*`)`

  error + = `zipUpRec(`$|\psi\rangle$*, aptr*$\rightarrow$*a, optr*$\rightarrow$*a, aLeg, trunc*`)`

  if *aptr has b-child* **then**

    error + = `zipUpRec(`$|\psi\rangle$*, aptr*$\rightarrow$*b, optr*$\rightarrow$*b, bLeg, trunc*`)`

  end

  error + = root-normalize aptr

  return *error*

end

if *aptr has b-child* **then**

  error + = `zipUpSite(`*aptr, optr, iLeg, trunc*`)`

  error + = `zipUpRec(`$|\psi\rangle$*, aptr*$\rightarrow$*b, optr*$\rightarrow$*b, bLeg, trunc*`)`

  error + = root-normalize aptr

  return *error*

end

error + = `zipUpSite(`*aptr, optr, aLeg, trunc*`)`

error + = root-normalize aptr

return *error*

Procedure `zipUpSite(`aptr, optr, iLeg, trunc`)`

`/* update the local site tensor for zip-up algorithm, see Fig. 7.5 for detail implementation. */`

Algorithm 1: The Zip-up Algorithm for TTPS

7.6 Time dependent variational principle algorithm for the TTPS

Although, the original TDVP is derived for the MPS, it can also be extended to the TTPS in a similar way as we have adapted for previous algorithms. The key to this extension is to design a recursive update framework, which is summarized in Algorithm 2. The procedure ensures that each site tensor M is forward propagated twice with each time evolved by $\frac{\Delta t}{2}$. Each bond tensor C is also updated twice with each time propagated by $-\frac{\Delta t}{2}$

$$M(t+\frac{\Delta t}{2}) = e^{-i\hat{H}^{(1)}_{\mathbf{eff}}\frac{\Delta t}{2}} \cdot M(t), \tag{7.3}$$

$$C(t-\frac{\Delta t}{2}) = e^{i\hat{H}^{(0)}_{\mathbf{eff}}\frac{\Delta t}{2}} \cdot C(t). \tag{7.4}$$

Here, $\hat{H}^{(1)}_{\text{eff}}$ is the single site effective Hamiltonian on this site which can be graphically represented as:

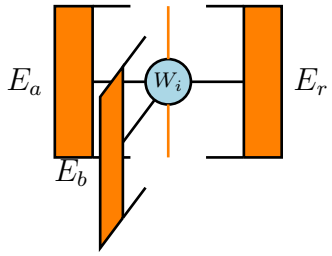

,

while $\hat{H}^{(0)}_{\text{eff}}$ is the zero-site effective Hamiltonian which has the same formula as in the MPS and can be graphically represented as:

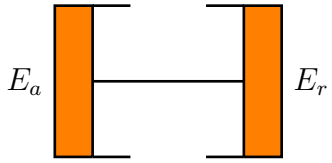

.

E_a, E_b and E_r are the environment tensors which can be constructed iteratively during the sweep. For instance, the environment tensor on its a-child node can be constructed

as

$$(E_a)^{i_4}_{i'_r i_r} = \tag{7.5}$$

$$\sum_{i_3 i'_p i'_3} \left(\sum_{i_1 i_p i_b} \left(\sum_{i_2} \left((E^a_a)^{i_3}_{i_1 i_2} (M_a)^{i_p}_{i_r i_2 i_b} \right)_{i_1 i_3 i_p i_r i_b} \sum_{i'_1} \left((E^b_a)^{i'_3}_{i'_1 i_b} (W_a)^{i'_p i_p}_{i'_r i_1 i'_1} \right)_{i_1 i'_p i'_r i_p i'_3 i_b} \right)_{i_3 i'_p i'_r i_r i'_3} \right.$$

$$\left. (M^\dagger_a)_{i'_p i_4 i_3 i'_3} \right), \tag{7.6}$$

here E^a_a and E^b_a are the a- and b-environment tensors of its a-child node. M_a and W_a are the state and operator site tensors of its a-child node. E_b and E_r can be constructed in the same way. Such a sweeping procedure leads to a Trotter decomposition error of second order, i.e., $\sim \mathcal{O}(\Delta t^3)$.

We also note that, by replacing the Krylov exponentializing solver used to solve Eq. (7.3) with the Lanczos eigen solver, we can adapt this algorithm directly to find the ground state, i.e., DMRG for the TTPS. The difference is that, instead of sweeping throughout the network just once as in the TDVP, in DMRG, we sweep multiple times until the desired accuracy is achieved.

Since the single-site algorithm can not increase the bond dimension during the local update process, we need to add noise terms to help DMRG get out of local minima. For the single-site TDVP, instead, there is no way to increase the bond dimension during the time-evolution process. Because of the increasing entanglement during the time-evolution and the lack of strategies to adjust the bond dimension dynamically limits the applicability of the single-site TDVP for general systems. For simple systems, the single-site TDVP algorithm can typically be very efficient and accurate. For demonstration and benchmark purposes, we construct an impurity model with three independent bands, and each of them has a semicircular DOS and intra-band Hubbard U interaction. As indicated in Fig. 7.6, the single-site TDVP for the TTPS with a relative small bond dimension $m = 20$ can already produce reliable results for both hall-filled and doped cases, by comparing with the quasi-exact data computed from single-band case with a much larger bond dimension ($m = 300$).

However, for more complicated systems, the single-site TDVP can fail to extract the long-time dynamics behavior correctly, because of the increasing entanglement

Algorithm `evolveSingleTree()`

- `evolveSite(`$\hat{H}^{(0)}_{eff}$, M, $\frac{\Delta t}{2}$`)`
- **if** *this node has a-child* **then**
  - `evolveSingleChild(`*aLeg*`)`
- **end**
- **if** *this node has b-child* **then**
  - `evolveSingleChild(`*bLeg*`)`
- **end**
- `evolveSite(`$\hat{H}^{(0)}_{eff}$, M, $\frac{\Delta t}{2}$`)`

Procedure `evolveSingleChild(`iLeg`)`

- **if** *iLeg* == *aLeg* **then**
  - $U, S, V^\dagger \leftarrow \mathrm{SVD}(M)$
  - $M \leftarrow V^\dagger$
  - $C \leftarrow U \cdot S$
  - `evolveBond(`$\hat{H}^{(0)}_{eff}$, C, $-\frac{\Delta t}{2}$`)`
  - `evolveSingleTree(` *its a-child*`)`
  - $U_a, S_a, V_a^\dagger \leftarrow \mathrm{SVD}(M_a)$
  - $M_a \leftarrow U_a$
  - $C_a \leftarrow U_a \cdot S_a$
  - `evolveBond(`$\hat{H}^{(0)}_{eff}$, C_a, $\frac{\Delta t}{2}$`)`
- **else if** *iLeg* == *bLeg* **then**
  - $U, S, V^\dagger \leftarrow \mathrm{SVD}(M)$
  - $M \leftarrow V^\dagger$
  - $C \leftarrow U \cdot S$
  - `evolveBond(`$\hat{H}^{(0)}_{eff}$, C, $-\frac{\Delta t}{2}$`)`
  - `evolveSingleTree(` *its b-child*`)`
  - $U_b, S_b, V_b^\dagger \leftarrow \mathrm{SVD}(M_b)$
  - $M_b \leftarrow U_b$
  - $C_b \leftarrow U_b \cdot S_b$
  - `evolveBond(`$\hat{H}^{(0)}_{eff}$, C_b, $\frac{\Delta t}{2}$`)`

Procedure `evolveSite(`$\hat{H}^{(1)}_{\mathbf{eff}}$, M, Δt`)`

- `/* using Krylov subspace method to exponentialize the effective 1-site Hamiltonian */`
- $M \leftarrow e^{-i\hat{H}^{(1)}_{\mathrm{eff}}\Delta t}M$

Procedure `evolveBond(`$\hat{H}^{(0)}_{\mathrm{eff}}$, C, Δt`)`

- `/* using Krylov subspace method to exponentialize the effective 0-site Hamiltonian */`
- $C \leftarrow e^{-i\hat{H}^{(0)}_{\mathrm{eff}}\Delta t}C$

Algorithm 2: Single-site TDVP time-evolution algorithm for TTPS.

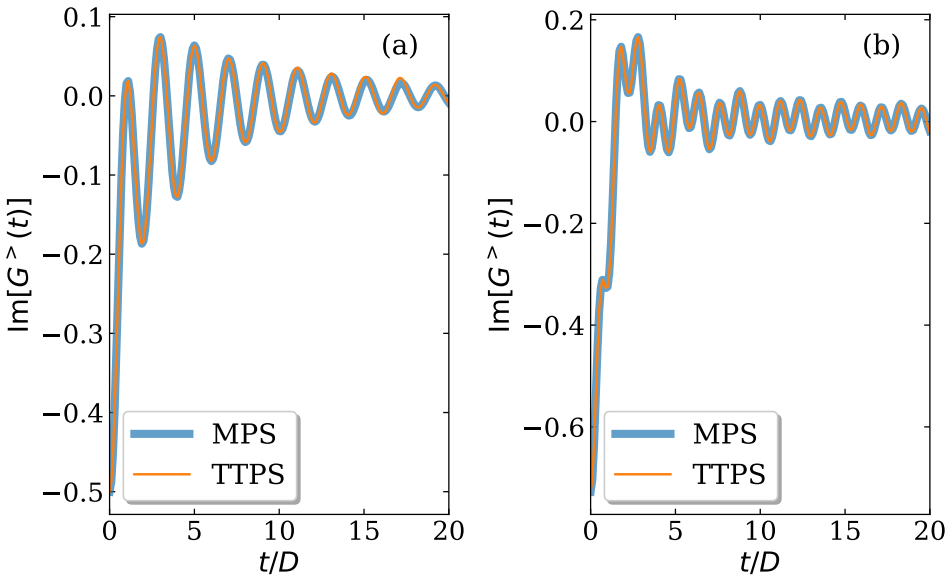

Figure 7.6: One-particle Green's function for the (a) half-filled and (b) doped three-band impurity model. The quasi-exact MPS solutions of $G^{>}(t)$ are obtained by evolving a single-band Anderson impurity model with the two-site TDVP algorithm with truncation weight $t_w = 1e^{-9}$ and maximal bond dimension 300, while the TTPS results are obtained by solving the impurity problem of three independent bands (each of them is constructed with the same parameters as the single-band model used in the MPS calculation) with the single-site TDVP algorithm with a bond dimension of 20. The Hubbard interaction is chosen to be $U = 2D$, and half-band width $D = 1$. For the doped case, we shift the overall filling by putting a chemical potential $\mu = -3.0$.

during the time-evolution. To circumvent this drawback, a two-site variant can be adapted. The key difference is that during the local update procedure, instead of updating only one site tensor, two site tensors are updated simultaneously. The two-site effective Hamiltonian can be graphically represented as:

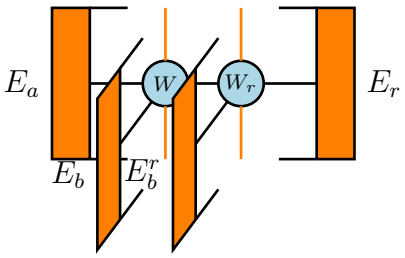

Now, $\hat{H}^{(2)}_{\text{eff}}$ is used to forward propagate the state, while $\hat{H}^{(1)}_{\text{eff}}$ is used to backward propagate the state. Since $\hat{H}^{(2)}_{\text{eff}}$ has a dimension of d^4m^8, compared with $\hat{H}^{(1)}_{\text{eff}}$ which

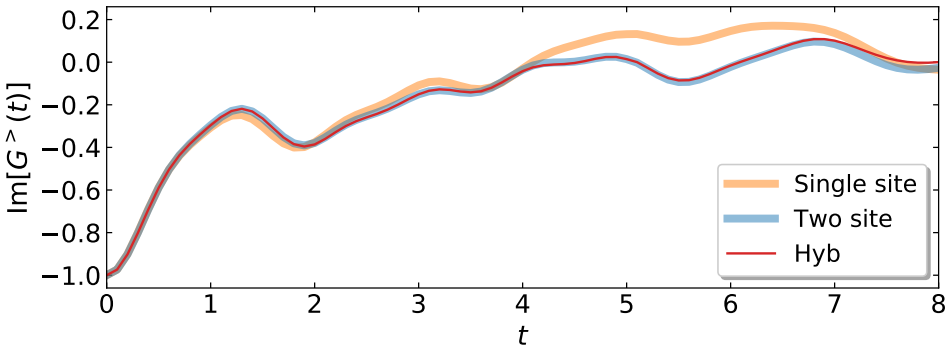

Figure 7.7: Comparing greater Green's functions computed from the single-site (orange line), two-site (cyan line) and hybrid (green dot) TDVP time-evolution algorithm. Here, the maximal bond dimension are fixed to be $m = 50$ for all cases. The time step is chosen to be $\Delta t = 0.1$. In the hybrid TDVP, the system is evolved by the two-site TDVP to 4 with a truncation weight of $t_w = 1e^{-8}$ (same as the pure two-site TDVP). In the construction of the impurity model, for each band, we use 30 sites for the conduction channel and 10 sites for the valence channel.

has a dimension of d^2m^6, we can expect that the two-site TDVP is computationally much heavier. To achieve a balance between accuracy and computational cost, one can adapt a hybrid framework: the system is evolved by the two-site TDVP to some point of time, then we switch to the single-site TDVP and evolve the state to the final time. This framework enables the dynamic adjustment of bond dimensions while maintaining the computational cost reasonable.

To compare the performance of the different time-evolution frameworks, we compute the Green's function of of an impurity model with three degenerate bands and each of them has an input DOS taking from $SrVO_3$. The interaction on the impurity is of density-density type. This system will be studied in detail in the latter discussions, and here it is used just for demonstration purpose. In Fig. 7.7, Green's functions computed from different time-evolution frameworks are plotted. We can see that with the same fixed maximal bond dimension ($m = 50$ for the plot), the hybrid TDVP exhibits a good agreement with the computational much more expensive pure two-site TDVP in a large time region, while the pure single-site TDVP fails to capture the correct long-time behaviors. Hence, in later discussions, unless specified, we will use the hybrid TDVP to evolve the underlying TTPS.

7.7 Application to $SrVO_3$

The $SrVO_3$ has a cubic crystal symmetry and the V $3d$ orbitals are split into two degenerate e_g and three degenerate t_{2g} orbitals. The three degenerate t_{2g} orbitals which are filled by one electron form the correlated subspace for this system. The non-interacting density of states is obtained from the FPLO [123, 124] implementation of the DFT, and the local interaction is assumed to have a density-density or Kanamori form as described in section 5.1. Here we have chosen the interaction parameters to be $U = 4eV$ and $J = 0.6eV$ as the physical relevant case.

Before presenting the DMFT results, we first analyze the atomic energy levels created by the density-density interaction to gain some insights. Since there is just one electron occupying the three degenerate t_{2g} orbitals in the atomic limit, we can expect a single hole excitation peaked at $-\epsilon$ in the removal spectra, with ϵ the on-site single-particle energy, and three single electron-excitation generated energy levels peaked at $U - 3J$, $U - 2J$ and $U + \epsilon$. Here, the $U - 3J$ level corresponds to the six degenerate high spin states formed by two electrons $\{|\uparrow,\uparrow,0\rangle, |\uparrow,0,\uparrow\rangle, |0,\uparrow,\uparrow\rangle, |\downarrow,\downarrow,0\rangle, |\downarrow,0,\downarrow\rangle, |0,\downarrow,\downarrow\rangle\}$, the $U - 2J$ level corresponds to the six degenerate low spin states $\{|\uparrow,\downarrow,0\rangle, |\uparrow,0,\downarrow\rangle, |0,\uparrow,\downarrow\rangle, |\downarrow,\uparrow,0\rangle, |\downarrow,0,\uparrow\rangle, |0,\downarrow,\uparrow\rangle\}$, and the $U+\epsilon$ level corresponds to the three degenerate doubly occupied states $\{|\uparrow\downarrow,0,0\rangle, |0,\uparrow\downarrow,0\rangle, |0,0,\uparrow\downarrow\rangle\}$. The higher particle excitations can result more complicated multiplets, but due to their large excitation energies, their weights are expected to be small. Once placed in a solid, we can expect that these discrete atomic levels will be shifted and broadened by their hybridization with the conduction bands.

For all the results shown in the following, we use a number of $N_c = 50$ conduction bath sites and $N_v = 18$ valence bath sites for each band, and have tested that an increasing of the number of bath sites does not change the results. The ground state is calculated with a truncation weight of $t_w^{gs} = 1e^{-12}$ and a minimal sweeping number of 30. To calculate the Green's function, we first evolve the excited states to $t = 4eV^{-1}$ by the two-site TDVP with a truncation weight of $t_w^{ev} = 1e^{-8}$ and a maximal bond dimension m, then we turn to the single-site TDVP to evolve to $t = 16eV^{-1}$. The time step is chosen as $\Delta t = 0.1eV^{-1}$. Finally, the time series is further extrapolated to $1000eV^{-1}$ by the linear-prediction method [125]. In the Fourier transformation to the frequency-axis, we use a Gaussian broadening in the kernel $e^{i\omega t-(\eta t)^2}$ of $\eta = 0.04eV$ to avoid the cutoff effects.

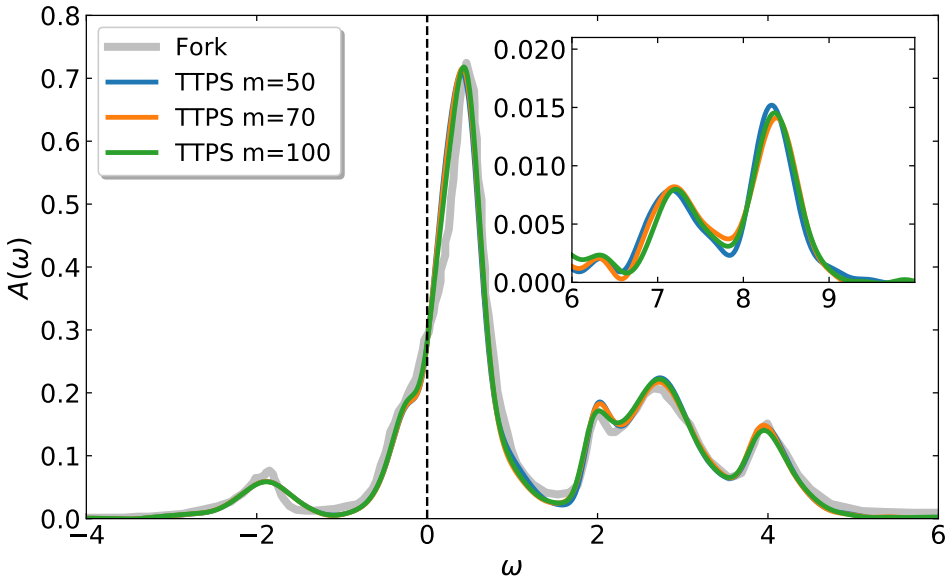

Figure 7.8: DMFT spectral functions of $SrVO_3$ with different bond dimensions. Here we have used the density-density interaction with $U = 4eV$ and $J = 0.6eV$. The blue, orange and green line corresponds to $m = 50, 70, 100$, respectively. The grey line is the FTPS result taken from [98] which is shown as a reference. The insert shows the two-electron excitations at higher energies.

The DMFT spectral functions with the density-density interaction for different m values are shown in Fig. 7.8. As discussed above, the main features of the spectral function consist of a hole-excitation peak in the removal spectra, and three single electron-excitation peaks in the upper Hubbard band. This is indeed the case as shown in Fig. 7.8. Profoundly, we are able to resolve these features already with a very small bond dimension $m = 50$, although the spectral function can be slightly changed by further increasing m. We should emphasis that these fine peak structures originated from the atomic multiplets are not present in the spectral function obtained from the QMC solver performed on the imaginary-time axis [98]. They are smeared out by the ill-conditioned analytical continuation process. Furthermore, as shown in the insert, besides the one-electron excitations, we are even able to resolve the two-electron excitations which have higher excitation energies. As shown in Fig. 7.9 and its insert, similar situation is observed for the Kanamori interaction:we are able to resolve the fine structures of the spectral function with a relative small bond dimension. For both type of interactions, we also plot the FTPS results from Ref. [98]

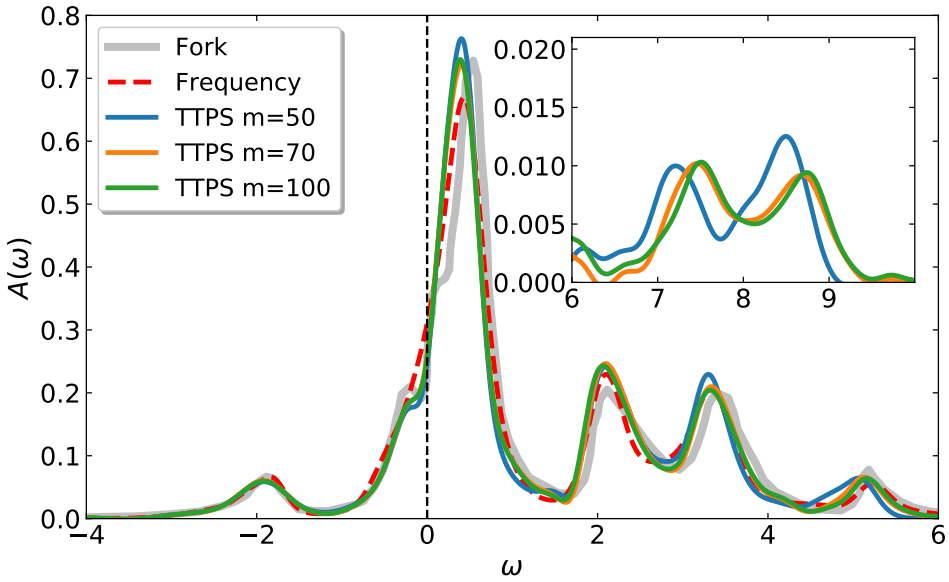

Figure 7.9: DMFT spectral functions of $SrVO_3$ with different bond dimensions. Here we have used the Kanamori interaction with $U = 4eV$ and $J = 0.6eV$. The blue, orange and green real line corresponds to $m = 50, 70, 100$, respectively. The grey line is the FTPS result taken from [98] which is shown as a reference. The insert shows the two-electron excitations at higher energies. The red dashed line is the spectra calculated from the projection method on the frequency-dome presented in chapter 5.

as for comparison. We observe a good overall agreement with the FTPS results, but small differences are found. These differences might come from the fact that we are using input DOS generated by different DFT implementations.

Finally, the computational time used for above calculations are:each DMFT loop takes about 28 minutes up to 2.5 hours by increasing the bond dimension m from 50 to 150 on a node with two ten-core processors(Intel Xeon E5-2630 v4, 2.20GHz).

7.8 Conclusion

In conclusion, despite the fact that the rotation to the natural-orbital representation can optimize the one-particle basis and results a small ground state entanglement for impurity problems, the chain geometry of the MPS is not suitable for multi-band models. This can be revealed from the following example:consider a multi-band impurity model which has a comparable band-width and interaction strength, then

the entanglement between the impurity and active sites belonging to the same band can be quite large, while the entanglement between the impurity sites can also be very large because of the inter-band interactions. Hence, there is no way of ordering on the chain geometry that can optimize the impurity-active and impurity-impurity entanglement at the same time. Furthermore, it is inevitable to introduce long-range hoppings when placing the bath sites of a multi-band impurity model on a chain geometry. Hence, alternative tensor product-states that are able to capture the entanglement structure of a general multi-band impurity model in an optimized way are desirable. The FTPS represents one of these attempts, it separates the degrees of freedom belonging to different bands by placing them on different forks. In this chapter, by further noting that the FTPS belongs to the more general tree tensor product states, we propose a TTPS representation of the many-body wave function of a general multi-band impurity model rotated in the natural-orbital basis. The advantage of this proposed TTPS is that it separates not only the degrees of freedom belonging to different bands, but also the conduction and valence band belonging to the same band explicitly. Together with all the benefits from the rotation to the natural-orbital basis, this solver has the potential to tackle problems that are not accessible in other methods. For benchmark and demonstration purposes, the prototypical compound $SrVO_3$ are solved in DMFT with the proposed solver. The obtained Green's function shows a fast convergence with the bond dimension and resolves the atomic multiplets correctly, and also shows a greet agreement with the FTPS results.

8

Conclusion and outlook

Correlated electron systems provide one of the most profound playgrounds for the exploring of novel physics. The interplay between correlation effects, orbital physics and lattice symmetries poses challenges for the development of universal concepts and methods for this category of materials. DMFT presents one of the most successful methods that is able to capture the relevant physics to a wide range of materials. Despite these successes, the local approximation to the self-energy which founds the basis of DMFT limits its applicability to systems in which non-local correlation effects are significant. Extensions of DMFT to include non-local correlations can be categorized into two directions, i.e., the diagrammatic extensions and cluster extensions. Methods following the diagrammatic extension to DMFT try to include diagrams which are not included in DMFT, exemplary examples are GW+(E)DMFT, FLEX+DMFT, DΓA and also the TRILEX method, while methods following the cluster extension to DMFT intend to enlarge the impurity size either in real- or momentum space, since the correlation effects within the impurity are correctly captured in DMFT. In this thesis, we have presented the adatom surface system as an exemplary example in which the non-local correlations and interactions can have significant impact on the emergence of exotic phases, and then we further devoted to the development of impurity solver which has the potential to pursue DMFT calculations with large cluster size and/or complicated multi-band structure on the real-axis. Here, we recapitulate the main results of each part.

In the first part of this thesis, we started with a short review of the general background of DMFT, then proceeded with a unified derivation of the (E)DMFT and TRILEX self-consistent equations. Then, motivated by the study of the interplay between charge-, spin- and pairing-instability in cuprates, the adatom surface systems which have a half-filling phase diagram that hosts competing exotic phases, are studied by the TRILEX method. A dome shaped superconducting phase is found in the vicinity of a strong spin fluctuating metal phase in the low doping region and a strong charge fluctuating metal phase in the high doping region. There are two interesting features of this superconducting phase: first, its superconducting critical temperature has a positive dependence on the long-range interaction strength; second, its paring symmetry is of chiral $d-$wave, which has a non-trivial topology invariant. By a close analysis of the individual contribution from the charge- and spin channel, we find a cumulative contributions from these two channels to the superconducting instability, which is a resultant of the underlying triangular lattice symmetry. Furthermore, the novel effects of the long-range interaction are reflected by its simultaneous enhancement of both the charge- and spin-fluctuations. Together with the cumulative contributions of the spin- and charge-fluctuations to the superconducting instability, the simultaneously enhancement of the spin- and charge-fluctuation by the long-range interaction explains the positive dependence of T_c on the long-range interaction strength. The uniqueness of the adatom systems are shown by the absent of superconductivity in systems that have a non-local but short-range interactions, and systems that have a different lattice symmetry. This synergic behavior of spin- and charge-fluctuations in triggering the superconducting instability provides a fundamental different scenario to the one on the square lattice that has competing spin- and charge-contributions.

In the second part of this thesis, we present the development of efficient solver for the general impurity models. It can be helpful for the extensions of DMFT by enlarging the impurity size, or solving multi-band systems with low symmetry. Starting with an introduction to the natural-orbital representation of a general impurity model, we established its superior to the commonly used star and chain representations by comparing the ground state properties (including entanglement distribution and density profile) in these representations. The profound small entanglement in the ground state and fast convergence of bond dimension with the number of bath sites promote the natural-orbital representation as the method of choice for the general

impurity problems. Furthermore, the fast (almost exponential) convergence of the density in the conduction (valence) bath sites to empty (fully occupied) motivates us to propose a projection framework that reduces the computation of the full impurity Green's function to solely computing the one of a small subsystem. This is done by first separating the whole system into three distinct parts including an impurity subsystem, the conduction and valence bath sites, and the hybridization between them. Next, we compute the Green's function of the small impurity subsystem, while the impurity Green's function of the whole system is obtained by expanding the subsystem Green's function with respect to the hybridization terms. We further formulated the one- and two-particle projection framework for general impurity models on the frequency-domain. The applicability of this projection framework is elucidated by the single-band Anderson impurity model and DMFT solution of the single-band Hubbard model on the Bethe lattice. Fast convergence of the Green's function with the expansion order and subsystem size are observed by comparing with the quasi-exact date from literature. To counter the difficulty to extend to higher order expansions and avoid the global changing of the wave function in the generation of the Krylov vectors on frequency-domain, we further extended this projection framework to the time-domain and observed a similar convergence of the Green's function with the subsystem size and expansion order. The proposed projection framework provides a balance between accuracy and computational cost for the impurity problems. Although, the projection framework has the same approximation criterion for calculations performed on the frequency- and time-domain, the choosing of on which domain to perform the calculation can be case dependent:the frequency-domain is best suited for spectroscopy calculations which usually have a quite large damping factor, while the time-domain is suited for non-equilibrium calculations and can be easily extended to higher expansion orders when needed.

Although the proposed projection framework can reduce the computational cost of solving the impurity problem, the entanglement structure of a multi-band impurity system is not represented by the MPS in an optimized way. To correctly capture the entanglement structure of multi-band impurity systems in the natural-orbital representation, we designed the TTPS which separates not only the degrees of freedom belonging to different bands but also the conduction and valence degrees of freedom within the same band explicitly. With such a combination of using the natural-orbital representation and the tree tensor product-states parameterization of the many-body

wave function, we proposed an impurity solver which has the potential to solve the impurity models inherited from DMFT calculations which are not accessible in other methods. To demonstrate the power of our method, the prototypical compound $SrVO_3$ is studied in DMFT with our solver. Indeed, our method resolves the peak features of the spectral function correctly and shows a fast convergence with the bond dimension. The application of this solver to more complicated systems, for instance Sr_2VO_4, Sr_2RuO_4 and also cluster extensions of DMFT are left for future study.

In summary, we have shown the importance and necessity of the inclusion of non-local correlations in the standard DMFT by the TRILEX study of the hole-doped adadom surface systems. Furthermore, the essential roles of the long-range interaction and lattice symmetry in triggering the superconducting pairing are revealed by analyzing the momentum resolved response functions. In order to include non-local correlations in the cluster extensions of DMFT and also handle multi-band systems, we move on to develop efficient impurity solver which lies at the core of DMFT calculations. By rotating to the natural-orbital basis, a projection framework on both the frequency- and time-domain are proposed and tested. Furthermore, to counter the intrinsic difficulties of the MPS representation of the many-body wave function of a multi-band system, we have proposed the TTPS to capture the entanglement structures correctly. This solver has been tested by solving the prototypical $SrVO_3$ and shows a great potential for further applications.

Acknowledgments

During the past four years of my Ph.D. study in Stuttgart, I have had the chance to work with many excellent people and participated in many interesting and challenging projects. This work would not be possible without the help of many people.

First and foremost, I want to thank my supervisor Dr. Philipp Hansmann for his continues mentoring and support. Throughout my Ph.D. study, discussions with him were always stimulating and inspiring. He led me into the research field of strongly correlated systems and guide me through the projects presented in this thesis. He also gave me the freedom to choose topic, and provided me supports when I was thwarted.

During the last two years of my Ph.D., I was fully dedicated in the developing of the new impurity solver and I want to thank Dr. Yi Lu and Prof. Maurits W. Haverkort for their invaluable insights and help on this project. Without them, there is no chance to achieve what was presented in this thesis. I am also in debt to Yi for sharing me knowledge on a variety range of research fields. I am grateful to my colleagues and friends in Stuttgart:Daniil Mantadakis, Schmid Michael and Stefan Kaeser. Daniil was my office mate for the past four years, he encouraged me when I was depressed and provided me unlimited help when I struggled. Without his company, life will be in another dim color. I appreciate the friendship with him sincerely. Michael was always full of energy and passion to his study and inspired me many times. Stefan was like a source of happiness in our group, his optimist helped me a lot when I was struggling with the bugs in my code. I thank Dr.Wenbin Rui for helping me on the topology aspect of matter, and also being a good friend and providing me encourage and help.

I thank Thomas Ayral for teaching me on the CT-QMC code and TRILEX method. I thank Prof. Oliver Parcollet for stimulating discussions on TRILEX and providing the elegant TRIQS library. I thank Prof. Dirk Manske for his support and stimulating discussions on the superconductivity pairing mechanism. I thank Prof. Dr. Sabine Andergassen for teaching me the many-body theory. I own my thank to Cornelia Hille for sharing me the insights on the Emery model and cRPA method. I thank Dr.Demetrio Vilardi and Dr. Ciro Taranto for teaching me FRG. I

thank Dr. Dobrautz Werner for the delightful times on the balcony and help on the Zusammenfassung.

I also want to thank my Chinese colleagues and friends during my stay in Stuttgart: Zhi-cheng Zhong, Wen-bin Rui, Yu-Xin Zhao and Li-Cheng Wang for sharing this period of shining memory in my life.

Last but not least, I want to thank my parents and girl friend for their continues support and unconditional love! This thesis is dedicated to you!

List of Figures

List of Algorithms

References

[1] Walter Metzner and Dieter Vollhardt. Correlated lattice fermions in $d = \infty$ dimensions. *Phys. Rev. Lett.*, 62:324–327, Jan 1989.

[2] Fusayoshi J. Ohkawa. Electron correlation in the hubbard modelin d=∞ dimension. *Journal of the Physical Society of Japan*, 60(10):3218–3221, 1991.

[3] Fusayoshi J. Ohkawa. Electron correlation in the hubbard model in d=+∞ dimension: Heavy electrons in the mott-transition region. *Journal of the Physical Society of Japan*, 61(5):1615–1632, 1992.

[4] Antoine Georges and Gabriel Kotliar. Hubbard model in infinite dimensions. *Physical Review B*, 45(12):6479, 1992.

[5] Qimiao Si and J. Lleweilun Smith. Kosterlitz-thouless transition and short range spatial correlations in an extended hubbard model. *Phys. Rev. Lett.*, 77:3391–3394, Oct 1996.

[6] G Rohringer, H Hafermann, A Toschi, AA Katanin, AE Antipov, MI Katsnelson, AI Lichtenstein, AN Rubtsov, and K Held. Diagrammatic routes to non-local correlations beyond dynamical mean field theory. *arXiv preprint arXiv:1705.00024*, 2017.

[7] Thomas A. Maier, Mark Jarrell, Thomas Pruschke, and Matthias H. Hettler. Quantum cluster theories. *Reviews of Modern Physics*, 77(July):1027–1080, 2005.

[8] M. H. Hettler, A. N. Tahvildar-Zadeh, M. Jarrell, T. Pruschke, and H. R. Krishnamurthy. Nonlocal Dynamical Correlations of Strongly Interacting Electron Systems. *Physical Review B*, 58(12):R7475, 1998.

[9] A. I. Lichtenstein and M. I. Katsnelson. Antiferromagnetism and d -wave superconductivity in cuprates: A cluster dynamical mean-field theory. *Physical Review B*, 62(14):R9283, 2000.

[10] Gabriel Kotliar, Sergej Y. Savrasov, Gunnar Pálsson, and Giulio Biroli. Cellular dynamical mean field approach to strongly correlated systems. *Phys. Rev. Lett.*, 87:186401, Oct 2001.

[11] Kenneth G. Wilson. The renormalization group: Critical phenomena and the kondo problem. *Rev. Mod. Phys.*, 47:773–840, Oct 1975.

[12] Ping Sun and Gabriel Kotliar. Extended dynamical mean-field theory and GW method. *Phys. Rev. B*, 66:085120, Aug 2002.

[13] Ping Sun and Gabriel Kotliar. Many-body approximation scheme beyond gw. *Phys. Rev. Lett.*, 92:196402, May 2004.

[14] Thomas Ayral, Silke Biermann, and Philipp Werner. Screening and nonlocal correlations in the extended hubbard model from self-consistent combined *gw* and dynamical mean field theory. *Phys. Rev. B*, 87:125149, Mar 2013.

[15] Motoharu Kitatani, Naoto Tsuji, and Hideo Aoki. Flex+dmft approach to the *d*-wave superconducting phase diagram of the two-dimensional hubbard model. *Phys. Rev. B*, 92:085104, Aug 2015.

[16] A.N. Rubtsov, M.I. Katsnelson, and A.I. Lichtenstein. Dual boson approach to collective excitations in correlated fermionic systems. *Annals of Physics*, 327(5):1320 – 1335, 2012.

[17] E. G. C. P. van Loon, H. Hafermann, A. I. Lichtenstein, A. N. Rubtsov, and M. I. Katsnelson. Plasmons in strongly correlated systems: Spectral weight transfer and renormalized dispersion. *Phys. Rev. Lett.*, 113:246407, Dec 2014.

[18] E. G. C. P. van Loon, M. Schüler, M. I. Katsnelson, and T. O. Wehling. Capturing nonlocal interaction effects in the hubbard model: Optimal mappings and limits of applicability. *Phys. Rev. B*, 94:165141, Oct 2016.

[19] Hartmut Hafermann, Erik G. C. P. van Loon, Mikhail I. Katsnelson, Alexander I. Lichtenstein, and Olivier Parcollet. Collective charge excitations of strongly correlated electrons, vertex corrections, and gauge invariance. *Phys. Rev. B*, 90:235105, Dec 2014.

[20] A. Toschi, A. A. Katanin, and K. Held. Dynamical vertex approximation: A step beyond dynamical mean-field theory. *Phys. Rev. B*, 75:045118, Jan 2007.

[21] Thomas Ayral and Olivier Parcollet. Mott physics and spin fluctuations: A unified framework. *Phys. Rev. B*, 92:115109, Sep 2015.

[22] Thomas Ayral and Olivier Parcollet. Mott physics and spin fluctuations: A functional viewpoint. *Phys. Rev. B*, 93:235124, Jun 2016.

[23] Jaksa Vucicevic, Thomas Ayral, and Olivier Parcollet. Trilex and $gw+$ edmft approach to d-wave superconductivity in the hubbard model. *Phys. Rev. B*, 96:104504, 2017.

[24] Thomas Ayral, Jaksa Vucicevic, and Olivier Parcollet. The fierz convergence criterion: a controlled approach to strongly-interacting systems with small embedded clusters. *arXiv preprint arXiv:1706.01388*, 2017.

[25] John Hubbard. Electron correlations in narrow energy bands. *Proceedings of the Royal Society of London. Series A. Mathematical and Physical Sciences*, 276(1365):238–257, 1963.

[26] Junjiro Kanamori. Electron correlation and ferromagnetism of transition metals. *Progress of Theoretical Physics*, 30(3):275–289, 1963.

[27] Martin C Gutzwiller. Effect of correlation on the ferromagnetism of transition metals. *Physical Review Letters*, 10(5):159, 1963.

[28] Thomas Ayral. *Nonlocal Coulomb Interactions and Electronic Correlations: Novel Many-Body Approaches*. PhD thesis, Ecole Polytechnique, 2015.

[29] Antoine Georges, Gabriel Kotliar, Werner Krauth, and Marcelo J. Rozenberg. Dynamical mean-field theory of strongly correlated fermion systems and the limit of infinite dimensions. *Rev. Mod. Phys.*, 68:13–125, Jan 1996.

[30] G. Kotliar, S. Y. Savrasov, K. Haule, V. S. Oudovenko, O. Parcollet, and C. A. Marianetti. Electronic structure calculations with dynamical mean-field theory. *Rev. Mod. Phys.*, 78:865–951, Aug 2006.

[31] Pierre Weiss. L'hypothèse du champ moléculaire et la propriété ferromagnétique. *J. Phys. Theor. Appl.*, 6(1):661–690, 1907.

[32] Gordon Baym and Leo P. Kadanoff. Conservation laws and correlation functions. *Phys. Rev.*, 124:287–299, Oct 1961.

[33] Gordon Baym. Self-consistent approximations in many-body systems. *Phys. Rev.*, 127:1391–1401, Aug 1962.

[34] F. Aryasetiawan, M. Imada, A. Georges, G. Kotliar, S. Biermann, and A. I. Lichtenstein. Frequency-dependent local interactions and low-energy effective models from electronic structure calculations. *Phys. Rev. B*, 70:195104, Nov 2004.

[35] J George Bednorz and K Alex Müller. Possible hight c superconductivity in the ba- la- cu- o system. *Zeitschrift für Physik B Condensed Matter*, 64(2):189–193, 1986.

[36] Andrea Damascelli, Zahid Hussain, and Zhi-Xun Shen. Angle-resolved photoemission studies of the cuprate superconductors. *Rev. Mod. Phys.*, 75:473–541, Apr 2003.

[37] J Zaanen, GA Sawatzky, and JW Allen. Band gaps and electronic structure of transition-metal compounds. *Physical Review Letters*, 55(4):418, 1985.

[38] FC Zhang and TM Rice. Effective hamiltonian for the superconducting cu oxides. *Physical Review B*, 37(7):3759, 1988.

[39] Sergej Schuwalow, Daniel Grieger, and Frank Lechermann. Realistic modeling of the electronic structure and the effect of correlations for sn/si(111) and sn/ge(111) surfaces. *Phys. Rev. B*, 82:035116, Jul 2010.

[40] Philipp Hansmann, Loïg Vaugier, Hong Jiang, and Silke Biermann. What about u on surfaces? extended hubbard models for adatom systems from first principles. *Journal of Physics: Condensed Matter*, 25(9):094005, 2013.

[41] P. Hansmann, T. Ayral, L. Vaugier, P. Werner, and S. Biermann. Long-range coulomb interactions in surface systems: A first-principles description within

self-consistently combined *gw* and dynamical mean-field theory. *Phys. Rev. Lett.*, 110:166401, Apr 2013.

[42] Gang Li, Philipp Höpfner, Jörg Schäfer, Christian Blumenstein, Sebastian Meyer, Aaron Bostwick, Eli Rotenberg, Ralph Claessen, and Werner Hanke. Magnetic order in a frustrated two-dimensional atom lattice at a semiconductor surface. *Nature communications*, 4:1620, 2013.

[43] Philipp Hansmann, Thomas Ayral, Antonio Tejeda, and Silke Biermann. Uncertainty principle for experimental measurements: Fast versus slow probes. *Scientific reports*, 6, 2016.

[44] Sen Zhou and Ziqiang Wang. Nodal $d + id$ pairing and topological phases on the triangular lattice of $\mathrm{na}_x\mathrm{coo}_2 \cdot y\mathrm{h}_2\mathrm{O}$: Evidence for an unconventional superconducting state. *Phys. Rev. Lett.*, 100:217002, May 2008.

[45] Shi-Quan Su, Zhong-Bing Huang, Rui Fan, and Hai-Qing Lin. Numerical study of ferromagnetic fluctuations and pairing correlations in the single-band hubbard model on the triangular lattice. *Phys. Rev. B*, 77:125114, Mar 2008.

[46] Kazuhiko Kuroki. Spin-fluctuation-mediated $d{+}id'$ pairing mechanism in doped $\beta{-}m\mathrm{NCl}$ ($m = \mathrm{Hf}, \mathrm{Zr}$) superconductors. *Phys. Rev. B*, 81:104502, Mar 2010.

[47] Rahul Nandkishore, LS Levitov, and AV Chubukov. Chiral superconductivity from repulsive interactions in doped graphene. *Nature Physics*, 8(2):158–163, 2012.

[48] Kuang Shing Chen, Zi Yang Meng, Unjong Yu, Shuxiang Yang, Mark Jarrell, and Juana Moreno. Unconventional superconductivity on the triangular lattice hubbard model. *Phys. Rev. B*, 88:041103, Jul 2013.

[49] Maximilian L. Kiesel, Christian Platt, Werner Hanke, Dmitry A. Abanin, and Ronny Thomale. Competing many-body instabilities and unconventional superconductivity in graphene. *Phys. Rev. B*, 86:020507, Jul 2012.

[50] Maximilian L. Kiesel, Christian Platt, Werner Hanke, and Ronny Thomale. Model evidence of an anisotropic chiral $d{+}id$-wave pairing state for the water-intercalated $\mathrm{na}_x\mathrm{coo}_2 \cdot y\mathbf{h}_2\mathbf{O}$ superconductor. *Phys. Rev. Lett.*, 111:097001, Aug 2013.

[51] Annica M. Black-Schaffer, Wei Wu, and Karyn Le Hur. Chiral d-wave superconductivity on the honeycomb lattice close to the mott state. *Phys. Rev. B*, 90:054521, Aug 2014.

[52] Philipp Werner, Armin Comanac, Luca de' Medici, Matthias Troyer, and Andrew J. Millis. Continuous-time solver for quantum impurity models. *Phys. Rev. Lett.*, 97:076405, Aug 2006.

[53] Thomas Ayral, Philipp Werner, and Silke Biermann. Spectral properties of correlated materials: Local vertex and nonlocal two-particle correlations from combined gw and dynamical mean field theory. *Phys. Rev. Lett.*, 109:226401, Nov 2012.

[54] Philipp Werner and Andrew J. Millis. Efficient dynamical mean field simulation of the holstein-hubbard model. *Phys. Rev. Lett.*, 99:146404, Oct 2007.

[55] Junya Otsuki. Spin-boson coupling in continuous-time quantum monte carlo. *Phys. Rev. B*, 87:125102, Mar 2013.

[56] Hartmut Hafermann. Self-energy and vertex functions from hybridization-expansion continuous-time quantum monte carlo for impurity models with retarded interaction. *Phys. Rev. B*, 89:235128, Jun 2014.

[57] Olivier Parcollet, Michel Ferrero, Thomas Ayral, Hartmut Hafermann, Igor Krivenko, Laura Messio, and Priyanka Seth. Triqs: A toolbox for research on interacting quantum systems. *Computer Physics Communications*, 196:398 – 415, 2015.

[58] E. A. Stepanov, A. Huber, E. G. C. P. van Loon, A. I. Lichtenstein, and M. I. Katsnelson. From local to nonlocal correlations: The dual boson perspective. *Phys. Rev. B*, 94:205110, Nov 2016.

[59] Annica M. Black-Schaffer. Edge properties and majorana fermions in the proposed chiral d-wave superconducting state of doped graphene. *Phys. Rev. Lett.*, 109:197001, Nov 2012.

[60] Mark Jarrell and J.E. Gubernatis. Bayesian inference and the analytic continuation of imaginary-time quantum monte carlo data. *Physics Reports*, 269(3):133 – 195, 1996.

[61] Philipp Werner and Michele Casula. Dynamical screening in correlated electron systems—from lattice models to realistic materials. *Journal of Physics: Condensed Matter*, 28(38):383001, 2016.

[62] Alexander Cyril Hewson. *The Kondo problem to heavy fermions*, volume 2. Cambridge university press, 1997.

[63] G. R. Stewart. Heavy-fermion systems. *Rev. Mod. Phys.*, 56:755–787, Oct 1984.

[64] A. J. Leggett, S. Chakravarty, A. T. Dorsey, Matthew P. A. Fisher, Anupam Garg, and W. Zwerger. Dynamics of the dissipative two-state system. *Rev. Mod. Phys.*, 59:1–85, Jan 1987.

[65] Sajeev John and Jian Wang. Quantum electrodynamics near a photonic band gap: Photon bound states and dressed atoms. *Phys. Rev. Lett.*, 64:2418–2421, May 1990.

[66] G. van der Laan, J. Zaanen, G. A. Sawatzky, R. Karnatak, and J.-M. Esteva. Comparison of x-ray absorption with x-ray photoemission of nickel dihalides and nio. *Phys. Rev. B*, 33:4253–4263, Mar 1986.

[67] M. W. Haverkort, G. Sangiovanni, P. Hansmann, A. Toschi, Y. Lu, and S. Macke. Bands, resonances, edge singularities and excitons in core level spectroscopy investigated within the dynamical mean-field theory. *EPL*, 108(5):57004, dec 2014.

[68] Michel Caffarel and Werner Krauth. Exact diagonalization approach to correlated fermions in infinite dimensions: Mott transition and superconductivity. *Phys. Rev. Lett.*, 72:1545–1548, Mar 1994.

[69] G. Sangiovanni, A. Toschi, E. Koch, K. Held, M. Capone, C. Castellani, O. Gunnarsson, S.-K. Mo, J. W. Allen, H.-D. Kim, A. Sekiyama, A. Yamasaki, S. Suga, and P. Metcalf. Static versus dynamical mean-field theory of mott antiferromagnets. *Phys. Rev. B*, 73:205121, May 2006.

[70] Massimo Capone, Luca de' Medici, and Antoine Georges. Solving the dynamical mean-field theory at very low temperatures using the lanczos exact diagonalization. *Phys. Rev. B*, 76:245116, Dec 2007.

[71] Erik Koch, Giorgio Sangiovanni, and Olle Gunnarsson. Sum rules and bath parametrization for quantum cluster theories. *Phys. Rev. B*, 78:115102, Sep 2008.

[72] Dominika Zgid, Emanuel Gull, and Garnet Kin-Lic Chan. Truncated configuration interaction expansions as solvers for correlated quantum impurity models and dynamical mean-field theory. *Phys. Rev. B*, 86:165128, Oct 2012.

[73] Chungwei Lin and Alexander A. Demkov. Efficient variational approach to the impurity problem and its application to the dynamical mean-field theory. *Phys. Rev. B*, 88:035123, Jul 2013.

[74] Y. Lu, M. Höppner, O. Gunnarsson, and M. W. Haverkort. Efficient real-frequency solver for dynamical mean-field theory. *Phys. Rev. B*, 90:085102, Aug 2014.

[75] Ralf Bulla, Theo A. Costi, and Thomas Pruschke. Numerical renormalization group method for quantum impurity systems. *Rev. Mod. Phys.*, 80:395–450, Apr 2008.

[76] R. Bulla. Zero temperature metal-insulator transition in the infinite-dimensional hubbard model. *Phys. Rev. Lett.*, 83:136–139, Jul 1999.

[77] R. Bulla, T. A. Costi, and D. Vollhardt. Finite-temperature numerical renormalization group study of the mott transition. *Phys. Rev. B*, 64:045103, Jun 2001.

[78] Ralf Bulla, Hyun-Jung Lee, Ning-Hua Tong, and Matthias Vojta. Numerical renormalization group for quantum impurities in a bosonic bath. *Phys. Rev. B*, 71:045122, Jan 2005.

[79] Th. Pruschke, R. Bulla, and M. Jarrell. Low-energy scale of the periodic anderson model. *Phys. Rev. B*, 61:12799–12809, May 2000.

[80] Emanuel Gull, Andrew J. Millis, Alexander I. Lichtenstein, Alexey N. Rubtsov, Matthias Troyer, and Philipp Werner. Continuous-time monte carlo methods for quantum impurity models. *Rev. Mod. Phys.*, 83:349–404, May 2011.

[81] Antoine Georges and Werner Krauth. Numerical solution of the d=∞ hubbard model: Evidence for a mott transition. *Phys. Rev. Lett.*, 69:1240–1243, Aug 1992.

[82] M. Ulmke, V. Janiš, and D. Vollhardt. Anderson-hubbard model in infinite dimensions. *Phys. Rev. B*, 51:10411–10426, Apr 1995.

[83] A. N. Rubtsov, V. V. Savkin, and A. I. Lichtenstein. Continuous-time quantum monte carlo method for fermions. *Phys. Rev. B*, 72:035122, Jul 2005.

[84] Philipp Werner, Armin Comanac, Luca de' Medici, Matthias Troyer, and Andrew J. Millis. Continuous-time solver for quantum impurity models. *Phys. Rev. Lett.*, 97:076405, Aug 2006.

[85] Philipp Werner and Andrew J. Millis. Hybridization expansion impurity solver: General formulation and application to kondo lattice and two-orbital models. *Phys. Rev. B*, 74:155107, Oct 2006.

[86] Steven R. White. Density matrix formulation for quantum renormalization groups. *Phys. Rev. Lett.*, 69:2863–2866, Nov 1992.

[87] Steven R. White. Density-matrix algorithms for quantum renormalization groups. *Phys. Rev. B*, 48:10345–10356, Oct 1993.

[88] Ulrich Schollwöck. The density-matrix renormalization group. *Rev. Mod. Phys.*, 77:259–315, Apr 2005.

[89] Karen A. Hallberg. New trends in density matrix renormalization. *Adv. Phys.*, 55(5-6):477–526, 2006.

[90] Ulrich Schollwöck. The density-matrix renormalization group in the age of matrix product states. *Ann. Phys.*, 326(1):96 – 192, 2011.

[91] Daniel J. García, Karen Hallberg, and Marcelo J. Rozenberg. Dynamical mean field theory with the density matrix renormalization group. *Phys. Rev. Lett.*, 93:246403, Dec 2004.

[92] Carsten Raas, Götz S. Uhrig, and Frithjof B. Anders. High-energy dynamics of the single-impurity anderson model. *Phys. Rev. B*, 69:041102(R), Jan 2004.

[93] F. Alexander Wolf, Ian P. McCulloch, and Ulrich Schollwöck. Solving nonequilibrium dynamical mean-field theory using matrix product states. *Phys. Rev. B*, 90:235131, Dec 2014.

[94] F. Alexander Wolf, Ara Go, Ian P. McCulloch, Andrew J. Millis, and Ulrich Schollwöck. Imaginary-time matrix product state impurity solver for dynamical mean-field theory. *Phys. Rev. X*, 5:041032, Nov 2015.

[95] Martin Ganahl, Patrik Thunström, Frank Verstraete, Karsten Held, and Hans Gerd Evertz. Chebyshev expansion for impurity models using matrix product states. *Phys. Rev. B*, 90:045144, Jul 2014.

[96] Martin Ganahl, Markus Aichhorn, Hans Gerd Evertz, Patrik Thunström, Karsten Held, and Frank Verstraete. Efficient dmft impurity solver using real-time dynamics with matrix product states. *Phys. Rev. B*, 92:155132, Oct 2015.

[97] Andreas Holzner, Andreas Weichselbaum, and Jan von Delft. Matrix product state approach for a two-lead multilevel anderson impurity model. *Phys. Rev. B*, 81:125126, Mar 2010.

[98] Daniel Bauernfeind, Manuel Zingl, Robert Triebl, Markus Aichhorn, and Hans Gerd Evertz. Fork tensor-product states: Efficient multiorbital real-time dmft solver. *Phys. Rev. X*, 7:031013, Jul 2017.

[99] Yi Lu and Maurits W Haverkort. Exact diagonalization as an impurity solver in dynamical mean field theory. *The European Physical Journal Special Topics*, 226(11):2549–2564, 2017.

[100] Norbert Schuch, Michael M. Wolf, Frank Verstraete, and J. Ignacio Cirac. Entropy scaling and simulability by matrix product states. *Phys. Rev. Lett.*, 100:030504, Jan 2008.

[101] J. Eisert, M. Cramer, and M. B. Plenio. Colloquium: Area laws for the entanglement entropy. *Rev. Mod. Phys.*, 82:277–306, Feb 2010.

[102] F. Fröwis, V. Nebendahl, and W. Dür. Tensor operators: Constructions and applications for long-range interaction systems. *Phys. Rev. A*, 81:062337, Jun 2010.

[103] Gregory M. Crosswhite, A. C. Doherty, and Guifré Vidal. Applying matrix product operators to model systems with long-range interactions. *Phys. Rev. B*, 78:035116, Jul 2008.

[104] Johannes Motruk, Michael P. Zaletel, Roger S. K. Mong, and Frank Pollmann. Density matrix renormalization group on a cylinder in mixed real and momentum space. *Phys. Rev. B*, 93:155139, Apr 2016.

[105] C. Hubig, I. P. McCulloch, and U. Schollwöck. Generic construction of efficient matrix product operators. *Phys. Rev. B*, 95:035129, Jan 2017.

[106] E M Stoudenmire and Steven R White. Minimally entangled typical thermal state algorithms. *New Journal of Physics*, 12(5):055026, may 2010.

[107] Steven R. White. Density matrix renormalization group algorithms with a single center site. *Phys. Rev. B*, 72:180403, Nov 2005.

[108] C. Hubig, I. P. McCulloch, U. Schollwöck, and F. A. Wolf. Strictly single-site dmrg algorithm with subspace expansion. *Phys. Rev. B*, 91:155115, Apr 2015.

[109] Stephen Wilson. *Electron correlation in molecules*. Courier Corporation, 2014.

[110] Steven R. White and Adrian E. Feiguin. Real-time evolution using the density matrix renormalization group. *Phys. Rev. Lett.*, 93:076401, Aug 2004.

[111] Walter Metzner and Dieter Vollhardt. Correlated lattice fermions in $d = \infty$ dimensions. *Phys. Rev. Lett.*, 62:324–327, Jan 1989.

[112] Antoine Georges, Gabriel Kotliar, Werner Krauth, and Marcelo J. Rozenberg. Dynamical mean-field theory of strongly correlated fermion systems and the limit of infinite dimensions. *Rev. Mod. Phys.*, 68:13–125, Jan 1996.

[113] E M Stoudenmire and Steven R White. Minimally entangled typical thermal state algorithms. *New J. Phys.*, 12(5):055026, may 2010.

[114] E. Müller-Hartmann. The hubbard model at high dimensions: some exact results and weak coupling theory. *Zeitschrift für Physik B Condensed Matter*, 76(2):211–217, Jun 1989.

[115] Till D. Kühner and Steven R. White. Dynamical correlation functions using the density matrix renormalization group. *Phys. Rev. B*, 60:335–343, Jul 1999.

[116] Eric Jeckelmann. Dynamical density-matrix renormalization-group method. *Phys. Rev. B*, 66:045114, Jul 2002.

[117] Jutho Haegeman, J. Ignacio Cirac, Tobias J. Osborne, Iztok Pižorn, Henri Verschelde, and Frank Verstraete. Time-dependent variational principle for quantum lattices. *Phys. Rev. Lett.*, 107:070601, Aug 2011.

[118] Jutho Haegeman, Christian Lubich, Ivan Oseledets, Bart Vandereycken, and Frank Verstraete. Unifying time evolution and optimization with matrix product states. *Phys. Rev. B*, 94:165116, Oct 2016.

[119] Sebastian Paeckel, Thomas Köhler, Andreas Swoboda, Salvatore R Manmana, Ulrich Schollwöck, and Claudius Hubig. Time-evolution methods for matrix-product states. *arXiv preprint arXiv:1901.05824*, 2019.

[120] Shimpei Goto and Ippei Danshita. Performance of the time-dependent variational principle for matrix product states in the long-time evolution of a pure state. *Phys. Rev. B*, 99:054307, Feb 2019.

[121] Jörg Rissler, Reinhard M Noack, and Steven R White. Measuring orbital interaction using quantum information theory. *Chemical Physics*, 323(2-3):519–531, 2006.

[122] Y-Y Shi, L-M Duan, and Guifre Vidal. Classical simulation of quantum many-body systems with a tree tensor network. *Physical review a*, 74(2):022320, 2006.

[123] Klaus Koepernik and Helmut Eschrig. Full-potential nonorthogonal local-orbital minimum-basis band-structure scheme. *Physical Review B*, 59(3):1743, 1999.

[124] I Opahle, K Koepernik, and H Eschrig. Full-potential band-structure calculation of iron pyrite. *Physical Review B*, 60(20):14035, 1999.

[125] Steven R. White and Ian Affleck. Spectral function for the $s = 1$ heisenberg antiferromagetic chain. *Phys. Rev. B*, 77:134437, Apr 2008.